

Dissertation
submitted to the
Combined Faculties for the Natural Sciences and for Mathematics
of the Ruperto-Carola University of Heidelberg, Germany
for the degree of
Doctor of Natural Sciences

Put forward by
Dipl.-Phys. Stefan Vehoff
born in Arnsberg (Germany)
Oral examination: 29th April, 2009

**Mid-infrared interferometric observations of the
high-mass protostellar candidate NGC 3603 IRS 9A**

Referees: Prof. Dr. Rainer Wehrse
Prof. Dr. Wolfgang J. Duschl

Zusammenfassung

Interferometrische Beobachtungen des massereichen potentiellen Protosterns NGC 3603 IRS 9A im mittleren Infrarot

Wir benutzen Infrarotbeobachtungen der größten Teleskope, Interferometer und Welt- raumteleskope, um der Frage der Entstehung von massereichen Sternen nachzugehen. Das Ziel dieser Beobachtungen ist IRS 9A, ein vielversprechendes Objekt, das wahr- scheinlich der seltenen Gruppe der sehr jungen und massereichen Protosterne angehört. Im ersten Teil dieser Arbeit beschreiben wir die unmittelbaren Ergebnisse der einzelnen Beobachtungen, während wir im zweiten Teil versuchen, ein Modell für IRS 9A und seine direkte Umgebung zu konstruieren, das diese Beobachtungen nachahmen kann. Wir be- nutzen außerdem ein öffentlich zugängliches Netz von spektralen Energieverteilungen, das für eine große Anzahl von protostellaren Objekten berechnet wurde.

Dabei stellen wir fest, dass das Erscheinungsbild von IRS 9A im mittleren Infrarot weder mit einfachen geometrischen Helligkeitsverteilungen, noch mit eindimensionalen Modellen der Dichtestruktur erklärt werden kann. Mittels Strahlungstransportmodellen, die aus zirkumstellaren Scheiben und Hüllen bestehen, sind wir jedoch in der Lage, alle unsere Beobachtungsdaten mit einem einzigen Modell zu erklären. Darüber hinaus zeigt der Vergleich mit dem Netz von protostellaren Objekten, dass es sich bei IRS 9A tatsäch- lich um einen massereichen Protostern handelt. Damit unterstützt unsere Untersuchung die Theorie, dass massereiche Sterne in einer ähnlichen Art und Weise entstehen wie Sterne mit geringer und mittlerer Masse.

Abstract

Mid-infrared interferometric observations of the high-mass protostellar candidate NGC 3603 IRS 9A

We investigate the question of how high-mass stars form by combining mid-infrared ob- servations from the worlds largest ground- and space-based telescopes and interferome- ters. The target of this study is IRS 9A, a promising candidate for the rare class of very young, high-mass protostars. In the first part of this work we present the immediate results and implications of the individual observations, and in the second part we try to devise a model for IRS 9A and its circumstellar structure that can account for these observations. We also make use of a publicly available grid of spectral energy distributions which has been calculated for a large number of protostellar objects.

We find that neither geometrical models of the brightness distribution nor simple one- dimensional models for the density structure can explain IRS 9A's appearance in the mid- infrared. However, using radiative transfer models that comprise circumstellar disks and envelopes, we are able to simultaneously reproduce all our observational data. Moreover, the comparison with the grid of protostellar objects independently confirms IRS 9A to be a high-mass protostar. Hence our study provides further support to the idea that high-mass stars form in a similar manner to their low- and intermediate-mass counterparts.

Contents

1	Introduction	1
1.1	Motivation	2
1.2	The formation of massive stars	4
1.3	The infrared source NGC 3603 IRS 9A	6
1.3.1	The giant H II region NGC 3603	6
1.3.2	The IRS 9 sources	7
1.3.3	IRS 9A	7
2	Optical interferometry	11
2.1	Angular resolution – why interferometry?	11
2.2	History of the field	13
2.3	Basic principles of optical interferometry	15
2.4	Visibility and the van Cittert-Zernike theorem	19
2.5	Image-plane and pupil-plane interferometers	21
2.6	Non-monochromatic light – finite bandwidth	23
2.7	Extended sources	25
2.8	Atmospheric turbulence and phases	26
2.9	The visibility in a few simple cases	28
2.9.1	Point source	28
2.9.2	Gaussian	29
2.9.3	Uniform disk	29
2.9.4	Binary	30
2.9.5	Ring	31
2.9.6	Combinations of models: disks with an inner hole and accretion disks	31
2.10	Observing in the infrared	32
2.10.1	Transmittance of the atmosphere	33
2.10.2	Background emission	33
2.10.3	Chopping and nodding	34
2.11	The VLT Interferometer	35
2.11.1	Baselines	35
2.11.2	Delay lines	36
2.11.3	MACAO and FINITO	37

3	MIDI	39
3.1	Optical layout	39
3.2	Detector	41
3.3	Observing procedure	42
4	Observations and data reduction I – MIDI	45
4.1	The MIA+EWS data reduction package	45
4.1.1	MIA	46
4.1.2	EWS	47
4.2	Acquisition images	48
4.2.1	Results	49
4.3	Photometric observations	51
4.3.1	Results	52
4.4	Interferometric observations	54
4.4.1	Visibilities	55
4.4.2	Correlated flux	57
4.4.3	Comparison and results	57
4.4.4	Differential phase	60
4.5	Interim summary	62
5	Observations and data reduction II – Gemini South and Spitzer	65
5.1	Aperture masking observations at Gemini South	65
5.2	Spitzer/IRS data	67
5.2.1	Spectral index, emission lines and PAH features	69
6	Modelling	71
6.1	Simple brightness distributions, binary and accretion disk models	71
6.1.1	Gaussian, uniform disk, ring	72
6.1.2	Binary and accretion disk models	73
6.1.3	Results	73
6.2	Radiative transfer models	74
6.2.1	DUSTY	75
6.2.1.1	Parameters	76
6.2.1.2	Results	77
6.2.2	MC3D	82
6.2.2.1	Model geometry	83
6.2.2.2	Parameters	84
6.2.2.3	Results I – Disk models	85
6.2.2.4	Results II – Disk + shell model	89
6.3	Fitting the spectra to a large grid of young stellar object SEDs	92
6.3.1	Spitzer	93
6.3.2	MIDI	94

6.3.3 Results	95
7 Summary and discussion	99
8 Conclusions	103
A Observing log	105
B Transmission curves of MIDI filters	109
C List of acronyms, units and constants	111
Bibliography	113
Acknowledgements	121

1 Introduction

Stars are the building blocks of the Universe and play a key role in most of the important processes that determine its structure and appearance. They account for the luminosity of galaxies, determine their structure and evolution, almost all heavy elements are formed in stars and the earliest stars are most likely responsible for the reionisation of the Universe. But apart from these rather “distant” characteristics, they are also of immediate importance for life here on Earth. Our Sun – which is a pretty ordinary star – started to convert hydrogen into helium about 4.6 billion years ago and has provided the energy to enable life as we know it ever since. Except for hydrogen, helium and traces of lithium, all elements that make up the Solar System were produced by generations of stars which returned their products of nuclear fusion to the interstellar medium (ISM) via stellar winds and supernova explosions prior to the formation of the Sun. The understanding of the life cycle of stars, from the processes that lead to their formation to the latest stages of their existence, is therefore one of the key challenges of (contemporary) astrophysics.

As we will see below, there are still many aspects especially concerning the formation of massive stars that we do not properly understand. Although there are several ideas which describe potential solutions to these problems, the precise mechanisms are still unclear. We will try to find clues that might shed some light on this difficult issue by primarily analysing mid-infrared observations of NGC 3603 IRS 9A which were taken at the Very Large Telescope Interferometer (VLTI). Only interferometers like the VLTI offer sufficiently high angular resolution (in the infrared) for this kind of study, although the data analysis is still limited to parametric model fitting and does not allow for the reconstruction of images. These data are complemented by observations from the Spitzer Space Telescope and the Gemini South Observatory, comprising a high resolution spectrum and supplemental interferometric data, respectively. The ultimate goal of this work is to devise a model that can simultaneously reproduce all these datasets, giving a detailed description of the properties of IRS 9A and of its circumstellar structure.

Some disambiguations: throughout this work the term “optical” is handled rather loosely and refers to the range of wavelengths from the “visual” regime (0.4–0.8 μm) to the near-infrared (NIR) and mid-infrared (MIR). The term applies more to the way in which the light is collected and handled since all modern “optical” telescopes are also able to collect infrared radiation. “Optical interferometry” implies the interference of light from an astronomical source that has been collected by telescopes. This is not to be confused with other interferometers, for example the ones used for measuring gravitational waves. A “massive star” denotes an OB star which is sufficiently massive to produce a type II supernova, that is, it applies to stars with $M_\star > 8M_\odot$ (assuming solar metallicity).

In the remaining part of this chapter, we describe the motivation for this work, covering the problems connected to high-mass star formation and introducing our primary target NGC 3603 IRS 9A. In Chapter 2, we give a basic introduction to optical interferometry, highlighting its advantages and drawbacks, before describing some details concerning (mid-) infrared observations and the VLTI. Chapter 3 is dedicated to the characteristics of the mid-infrared interferometric instrument (MIDI) and the associated observing procedure. After that we describe the details of the data reduction and our observational results in Chapter 4, including a short summary of problems and immediate conclusions that can be drawn from them. We present the additional data from the Spitzer Space Telescope and the Gemini South Observatory in Chapter 5, before switching to our diverse modelling efforts in Chapter 6. Finally, a concise summary and discussion of the results is given in Chapter 7 and Chapter 8 concludes this work.

1.1 Motivation

While the understanding of star formation in general has made huge improvements over the last few decades, our knowledge of the processes that lead to the formation of massive stars is still only sketchy. Recent reviews of both star formation in general and the formation of massive stars in particular can be found in, for example, McKee & Ostriker (2007), Beuther et al. (2007), Zinnecker & Yorke (2007) and Krumholz & Bonnell (2007). Our limited knowledge about the early evolutionary phases of massive stars is mostly due to the following three facts. First, massive stars are rare objects. This results in, on average, large distances (several kpc) to the sites of their formation and, therefore, limited angular resolution when observing them. Second, they evolve much faster than low-mass stars during all stages of their existence. As a consequence of this, they reach the main sequence while still enshrouded in massive envelopes of gas and dust, and the whole pre-main sequence phase is not observable at optical wavelengths. Third, most of them do not form in isolation and close companions, either protostars themselves or main sequence stars, can further complicate the circumstances via dynamical interactions, stellar winds and outflows.

This situation is rather unfortunate since massive stars, despite their short lifetime and rarity, have a much larger influence on their surroundings than their low-mass siblings. They dominate the luminous, kinematic, and chemical output of all stars. With their fast stellar winds and ionising radiation, massive outflows, H II regions and supernova explosions they provide an important source of mixing and turbulence in the ISM. Table 1.1 gives an overview of some basic parameters of stars of different masses, including their relative frequency in the solar neighbourhood and also according to an initial mass function (IMF) obtained from the universal power law $dN/d\log M \sim M^{-\Gamma}$, first found by Salpeter (1955) for low-mass stars. A discussion of the values for the power law index Γ and also of an upper mass cutoff can be found in Massey (1998). The values obtained from this formula are normalised in order to have exactly one star in the highest mass interval.

M/M_{\odot}	L/L_{\odot}	T_{eff} [K]	Spectral			N	Mass [M_{\odot}]	Number of stars
			type	t_{evol} [yr]				
60.0	7.9×10^5	44500	O5V	5.5×10^5	3.33×10^{-7}	64–128	1	
18.0	5.2×10^4	30000	B0V	2.4×10^6	1.25×10^{-3}	32–64	2.55	
6.0	8.3×10^2	15400	B5V	5.2×10^7		16–32	6.5	
3.0	5.4×10^1	9500	A0V	3.9×10^8	6.25×10^{-3}	8–16	16.6	
1.5	6.5×10^0	7200	F0V	1.8×10^9	3.00×10^{-2}	4–8	42	
1.1	1.5×10^0	6050	G0V	5.1×10^9	7.70×10^{-2}	2–4	108	
0.8	4.3×10^{-1}	5250	K0V	1.4×10^{10}	1.25×10^{-1}	1–2	275	
0.5	7.7×10^{-2}	3850	M0V	4.8×10^{10}	7.60×10^{-1}	0.5–1	700	
0.2	1.1×10^{-2}	3250	M5V	1.4×10^{11}		Total:	1151.65	

Table 1.1: Basic parameters of main sequence stars. The time t_{evol} is the time after which the star has converted 10 % of its initial hydrogen content into helium. N gives the relative frequency of main sequence stars of the corresponding spectral type per 10^4 pc^3 in the solar neighbourhood. The two last columns are taken from Zinnecker & Yorke (2007) for $\Gamma = 1.35$, the values for N from LeDrew (2001) and all other data from Unsöld & Baschek (1999). More recent discussions concerning the properties of early type main sequence stars can be found in Crowther (2005) and Martins et al. (2005).

Together with the values for the solar neighbourhood they illustrate how rare high-mass stars really are. Regarding the given mass ranges, stars are generally known to exist from about $0.075 M_{\odot}$, the lower limit for hydrogen burning, up to $\gtrsim 100 M_{\odot}$. However, this upper limit is quite uncertain and a range of roughly $100 M_{\odot}$ to $150 M_{\odot}$ can be found in the literature.

Currently there are three major concepts of how massive stars form (see Section 1.2). They are fundamentally different from each other and observations are needed in order to rule out the theories that do not fit. As mentioned above, observing high-mass stars during their formation is a difficult task, imposing strong constraints not only on the telescopes and instruments, but also on the region to be observed. If the technical requirements are met (high angular resolution and sensitivity in the infrared or sub-mm regime), one has to find star forming regions which contain suitable candidates that might eventually evolve into high-mass main sequence stars. A promising location is the violent neighbourhood of a cluster of main sequence O and B stars, as described, for example, in Nürnberger et al. (2005). Their strong stellar winds and ionising radiation are able to remove large parts of the gas and dust that normally obscure the forming stars from our view, thus enabling a look at relatively early evolutionary stages of the formation process.

In this work we make use of the unique capabilities of the VLTI that is operated by the European Southern Observatory (ESO) in Chile. The VLTI satisfies all primary prerequisites mentioned above: excellent angular resolution, high sensitivity and a detector for the mid-infrared (MIDI). But where should we look for suitable sources to observe? An extensive multi-wavelength study of the giant galactic H II region NGC 3603 (Nürnberger & Petr-Gotzens 2002; Nürnberger et al. 2002; Nürnberger & Stanke 2003; Nürnberger

2003) revealed an association of highly reddened, luminous and massive stellar sources in the immediate vicinity of NGC 3603's central OB cluster, the IRS 9 sources. They are located on the border of a massive molecular cloud core (NGC 3603 MM 2) in the direction of the cluster, which supports the idea that they have been released from their natal molecular cloud material just a short time ago. Together with their steeply rising spectral energy distributions (SEDs) and large near- and mid-infrared excess emission, these sources might be members of the rare class of very young high-mass stars, possibly still gaining mass from their circumstellar envelopes. We exploit this advantageous location close to the cluster by observing IRS 9A, the brightest and most massive member of these young sources, and try to shed some light onto the difficult issue of high-mass star formation.

1.2 The formation of massive stars

The problems connected to the observation of massive stars that are in the process of their formation have already been outlined in the previous subsection, but there are also many theoretical challenges connected to the problem. If we compare the values of, for example, the density, temperature and the length scales at the beginning and at the end of the star formation process, we see that they stretch across an incredibly huge range (e.g. $\gtrsim 20$ orders of magnitude for the density). There are numerous problems connected to the radiation transport, for example dust and line opacities, transitions from optically thick to optically thin media, conditions that cannot be approximated by local thermodynamic equilibrium (LTE), etc. The effects connected to the radiation transport are especially important, since high-mass stars undergo hydrogen burning while still accreting a significant amount of their mass. The thermonuclear fusion leads to strong feedback effects – radiative acceleration and photoionisation – that might inhibit the further growth of the star. State-of-the-art computer models have to take all of this into account, and furthermore take care of magnetic fields, turbulence, chemistry, the dynamical interactions with other stars and stellar winds, while at the same time performing the calculations in three dimensions. Therefore, no model currently exists that is able to reproduce all evolutionary stages from the parent molecular clouds to main sequence stars.

Following the review article by Zinnecker & Yorke (2007), there are three competing concepts of how massive stars form. These are:

- ▷ A scaled-up and slightly modified version of the way in which low-mass stars form, that is, monolithic collapse of isolated cores and disk accretion
- ▷ Collisions and mergers of low- to intermediate mass stars in very dense systems
- ▷ Via “competitive accretion” and runaway growth in a protocluster environment

Depending on the initial conditions, each of these scenarios might actually take place in nature. The different concepts are briefly summarised hereafter.

For reasons that have been addressed above, high-mass star formation cannot simply be a scaled-up and unmodified version of low-mass star formation. The latter is now generally accepted to proceed via accretion of material of the circumstellar envelope through an accretion disk, which allows most of the gas and dust to reach the star while the remaining material migrates outward, taking along with it most of the angular momentum (Lynden-Bell & Pringle 1974). Yet the first calculations (using spherical symmetry) indicated that the radiative acceleration found close to a forming star with $M_* \gtrsim 10 M_\odot$ might be able to stop this accretion process. However, more recent simulations are able to produce massive stars with up to $30 M_\odot$ or $40 M_\odot$ via disk accretion, as the radiative acceleration was found to be a less significant barrier than had originally been thought (e.g. Yorke & Sonnhalter 2002; Krumholz et al. 2005, 2009). This is because of a combination of effects, most notably the so-called *flashlight effect* that leads to a concentration of radiation in the polar directions, significantly reducing the radiative flux close to the equatorial plane. Still, the question of whether the most massive stars also form in this way remains an open one and the current results have not yet reached a conclusive state. Observational evidence that high-mass stars up to late O types can form via disk accretion can be found in, for example, Chini et al. (2004, 2006), Nürnberger et al. (2007) and Qiu et al. (2009).

Due to the problems caused by the strong stellar radiation field and also because massive stars in clusters are very tightly packed, the idea of stellar collisions was proposed as a possible formation process (Bonnell et al. 1998). However, this requires a very high density of already quite massive stellar objects in order to be effective, and the other two scenarios seem more likely. Therefore, although this “coalescence scenario” might occur in special circumstances, producing very massive stars in dense clusters, it is no longer considered generally necessary (Zinnecker & Yorke 2007).

Star formation via competitive accretion was first proposed by Bonnell et al. (1997, 2001). The authors investigated the evolution of a cluster of protostellar seeds embedded in a large, dense cloud of molecular gas. Each seed then has the chance to gain mass from its individual accretion domain, which grows larger as the mass of the stellar seed increases. On the other hand, the amount of gas that enters an accretion domain will depend on the environment, since gas settles in the deepest part of the gravitational potential. Thus, the scenario for competitive accretion can be shortly described by the real estate concept “location, location, location” and the capitalistic concept “the rich get richer”. In the end, competitive accretion leads to a very steep IMF which is close the one observed in young clusters (Bonnell et al. 2007), while at the same time giving a physical explanation of how the stars gather their matter.

One issue concerning high-mass star formation has not yet been addressed. Massive stars, on average, seem to have more physical companions than low-mass stars (Preibisch et al. 1999; Duchêne et al. 2001; Köhler et al. 2006). The observed high value of the multiplicity and the clustering of massive stars provides a rather strong argument against the monolithic collapse of isolated cores. Therefore, Zinnecker & Yorke (2007) describe massive star formation as a continuum of cases from the theory of monolithic collapse + disk

Stellar cluster		Associated H II region	
Distance	7200 pc		
Diameter	< 4.2 pc	Diameter	100 pc
$M_V^{(a)}$	-9.6^m	$L_{H\alpha}$	$1.5 \times 10^{32} W$
$L_V^{(a)}$	$6.1 \times 10^5 L_{V,\odot}$	M_{H^+}	$3.9 \times 10^4 M_\odot$
Equiv. $M_{OB}^{(b)}$	$2.6 \times 10^3 M_\odot$	N_{Lyc}	$1.12 \times 10^{51} s^{-1}$
Age	< 3 Myr	Equiv. M_{OB}	$5 \times 10^3 M_\odot$
Γ	$-0.7^{(c)}$ to $-1.7^{(d)}$	Equiv. $N(O5 V)$	20

Table 1.2: Key parameters of NGC 3603’s stellar cluster and H II region taken from Eisenhauer et al. (1998) and references therein. (a) corrected for extinction, (b) within a diameter of 2 pc and for spectral types earlier than B2, (c) slope for stars with $1 M_\odot \lesssim M_* \lesssim 30 M_\odot$, (d) slope for stars with $M_* \gtrsim 15 M_\odot$.

accretion to the competitive accretion scenario.

1.3 The infrared source NGC 3603 IRS 9A

1.3.1 The giant H II region NGC 3603

Today known as one of the most massive, optically visible H II regions in the Milky Way (Goss & Radhakrishnan 1969), NGC 3603 was first discovered by Sir John Herschel in 1834, who classified it as a globular cluster embedded in a nebula with a diameter of more than $2'$ (Sher 1965). It contains a massive cluster of young stars (2–3 Myr, e.g., Melnick et al. 1989) comprising a few Wolf-Rayet stars, several early O-type stars and many O stars of later type. Their integrated $H\alpha$ flux of $\approx 1.5 \times 10^{32} W$ (Kennicutt 1984) is responsible for ionising the region, and the total stellar luminosity estimated from this is $\approx 10^7 L_\odot$, about 100 times the luminosity of the Orion nebula. Hence NGC 3603 is frequently compared to 30 Doradus in the Large Magellanic Cloud, although 30 Doradus is about 40 times more massive, the ionising flux is 7 times larger and it is about 10 times larger in diameter (Balick et al. 1980). Still, NGC 3603 can be seen as a (small) galactic prototype of the starburst clusters which are observed in other galaxies.

NGC 3603 is located in the Carina spiral arm of our Galaxy at a distance of about 7 ± 1 kpc. Despite numerous efforts in the past four decades, this distance is still rather uncertain. Some authors estimate it to about 6.1–6.3 kpc (Goss et al. 1972; de Pree et al. 1999; Pandey et al. 2000; Stolte et al. 2004), some to 7.0–7.3 kpc (Moffat 1983; van den Bergh 1978; Caswell & Haynes 1987; Melnick et al. 1989) and others to about 8 kpc or even 10 kpc (Goss & Radhakrishnan 1969; Moffat 1974; Crowther & Dessart 1998). Throughout this work we will adopt a distance of 7 kpc for NGC 3603. In spite of this rather large distance, the foreground extinction towards the cluster is only 4–5 mag (Sher 1965; Moffat 1983; Melnick et al. 1989). The key parameters of NGC 3603, divided into the central cluster and the H II region, are summarised in Table 1.2.

The Wolf-Rayet and O stars of the central cluster have a huge influence on the (ISM) in their surroundings, most notably through their ionising radiation and fast stellar winds of up to several hundred km/s (Balick et al. 1980). Their combined effort evaporates and disperses the ISM, resulting in pillars of gas and dust and protoplanetary disks like in Orion (Brandner et al. 2000). The first mid-infrared observations were carried out by Frogel et al. (1977) and the authors revealed numerous sources in the vicinity of the H II complexes. One of these sources is located about 1.2' (2.4 pc) south of the cluster and was named IRS 9 (InfraRed Source 9). Figure 1.1 shows NGC 3603's location in the sky and also the target of our observations, IRS 9A.

1.3.2 The IRS 9 sources

The observations by Frogel et al. (1977) suffered from the rather poor angular resolution and sensitivity available at that time. They were followed by a series of more detailed studies at different wavelengths and with several telescopes and instruments. Among them are NIR observations from the South African Astronomical Observatory, the Anglo-Australian Observatory, the La Silla Observatory and the Cerro Tololo Inter-American Observatory (Persi et al. 1985; Roth et al. 1987), 3.4 cm data from the Australia Telescope Compact Array (de Pree et al. 1999), NIR data from the VLT and the Las Campanas Observatory (Brandl et al. 1999; Tapia et al. 2001), sub-millimetre observations from the Swedish-ESO Submillimetre Telescope (Nürnberger et al. 2002) and NIR as well as MIR data from the Las Campanas, Paranal and La Silla Observatories (Nürnberger & Petr-Gotzens 2002; Nürnberger & Stanke 2003; Nürnberger 2003, 2004; Nürnberger 2008). These observations revealed IRS 9 as a deeply embedded cluster of protostars whose members were only recently released from their natal molecular cloud by interactions with the stellar wind and ionising radiation of the OB cluster. A list of infrared sources at and around the location of the IRS 9 cluster is given in Tapia et al. (2001), whereas IRS 9A, B and C are characterised in detail in Nürnberger (2003) and Nürnberger (2008).

An impressive near-infrared image of the whole region was obtained with the ISAAC instrument at the VLT by Brandl et al. (1999). It is shown in Figure 1.2, where IRS 9A can be seen as the bright, yellow source towards the south-east of the cluster. While it appeared rather faint in the optical images (e) and (f) of Figure 1.1, it now clearly stands out in comparison to the sources in its surroundings. Other members of the IRS 9 cluster can also be seen, all of them showing very red colours typical for sources that are surrounded by large amounts of gas and dust. High-resolution JK_sL' images of the IRS 9 cluster can also be found in Nürnberger (2008).

1.3.3 IRS 9A

IRS 9A is the brightest member of the deeply embedded cluster of protostars. Due to insufficient angular resolution, no information about its immediate circumstellar structure

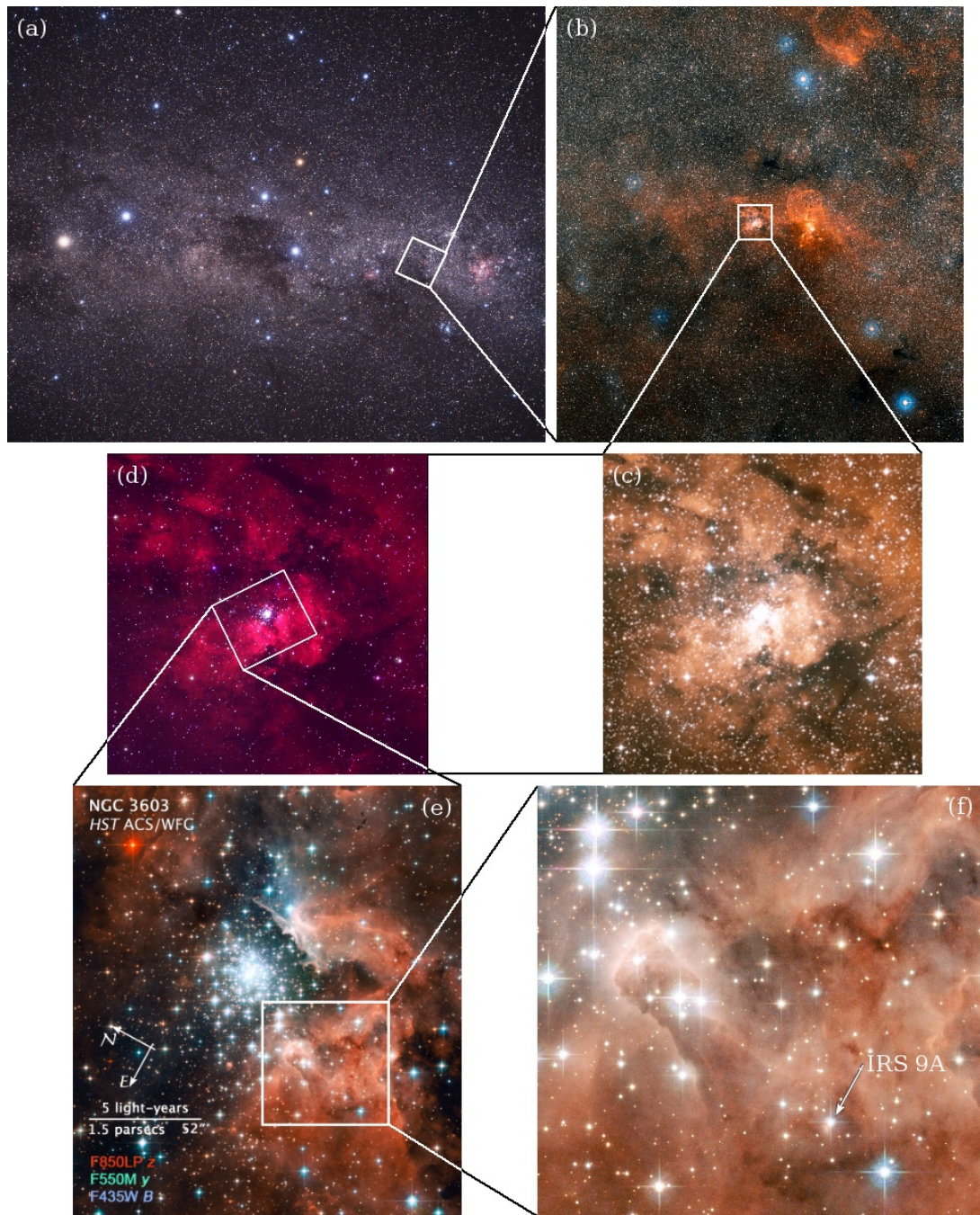


Figure 1.1: A series of images showing ever smaller portions of the sky containing NGC 3603 IRS 9A. (a) the part of the Milky Way containing the Southern Cross, the Coalsack and α and β Centauri. (b) the region around NGC 3603 in a $2.6^\circ \times 2.8^\circ$ image. (c) the innermost part of the previous image, spanning $13.5' \times 13.5'$. (d) the same region in different colours, most notably H α in red. (e) Hubble image of NGC 3603. (f) detail (roughly $1' \times 1'$) of the previous image showing the location of IRS 9A. Image credits: (a) A. Fujii, (b,c) NASA, ESA and the DSS 2, D. de Martin, (d) MPIA WFI, T. Stanke, (e,f) NASA, ESA and the Hubble Heritage (STScI/AURA)-ESA/Hubble Collaboration, J. M. Apellániz & D. de Martin.

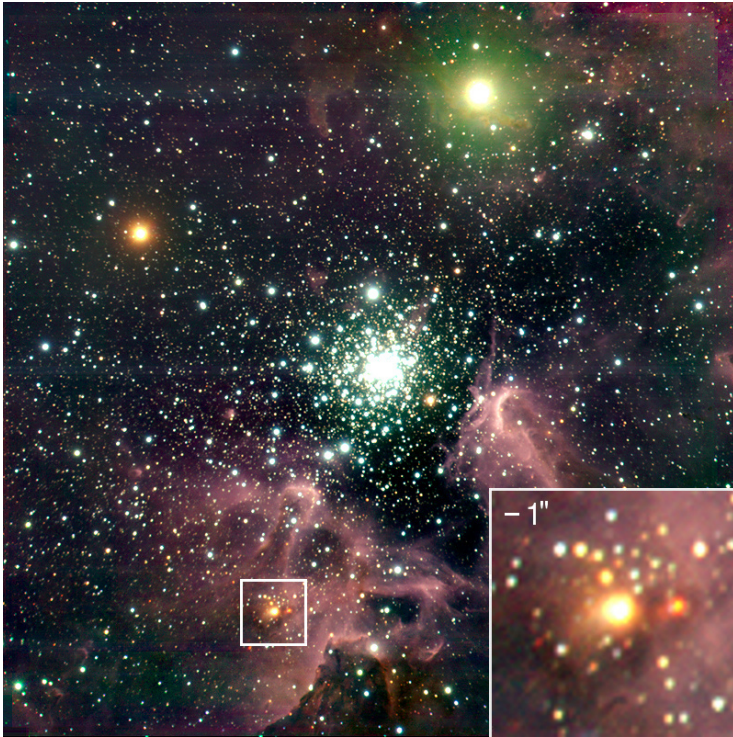


Figure 1.2: Near-infrared image of NGC 3603 taken with ISAAC at the VLT. The colours correspond to the following filters and wavelengths: blue = J_s band ($1.24 \mu\text{m}$), green = H band ($1.65 \mu\text{m}$), red = K_s band ($2.17 \mu\text{m}$). The image is $3.4' \times 3.4'$ in size, which corresponds to about $7 \times 7 \text{pc}^2$ for a distance of 7 kpc. IRS 9A is the rather large yellow dot at the 7 o'clock position and also shown in the small inset. North is up and east to the left. Taken from the ESO press release 16/99 (<http://www.eso.org/public/outreach/press-rel/pr-1999/pr-16-99.html>).

has been obtained so far, but together with the two adjacent sources IRS 9B and C it has been analysed in detail by Nürnberger (2003) and Nürnberger (2008). He was able to reproduce the measured SED through a combination of three Planck functions and obtained temperatures of 22000 K (central object), 1000–1150 K and 250 K (surrounding dust) for the three components. Together, the three Planck functions can account for the data for visual extinctions of 4.5 mag – the foreground extinction towards the cluster – and 15 mag or 20 mag of additional, intrinsic extinction. The most important results of the study are summarised in Table 1.3, which also shows the flux of IRS 9A from the near- to the mid-infrared. The mass of the circumstellar gas and dust, $M_{\text{circ.st.}}$, has been estimated based on the aforementioned dust temperatures and the assumption that the mid-infrared emission is optically thin. Therefore, it represents only a lower limit on the true mass. The coordinates of IRS 9A are given in Table A.1 in appendix A.

Moffat et al. (2002) used the Chandra X-ray Observatory in order to search for sources in NGC 3603. They did not detect IRS 9A at a 3σ detection level of $4.5 \times 10^{-4} \text{Jy/beam}$. This is a further indication that IRS 9A is indeed a very young, massive source. In combination with the many other measured properties and the large amounts of gravitationally bound circumstellar material, IRS 9A is a very promising candidate for a high-mass protostar and an ideal object to further examine the processes that lead to the formation of high-mass main sequence stars.

1 Introduction

Basic properties		Filter	Wavelength $\lambda_c \pm \Delta\lambda$ [μm]	Magnitude ^a	Flux ^b [Jy]	Flux ^c [Jy]
Age	$10^{4\dots 5}$ yr	J'	1.25 ± 0.2	12.87 ± 0.2	0.038	2.11
A_V	$\approx 22^{\text{m}}$	H	1.65 ± 0.3	10.92 ± 0.2	0.096	1.16
T	≈ 22000 K	K'	2.16 ± 0.33	8.55 ± 0.2	0.405	2.00
Spectral type	B2 or earlier	L	3.78 ± 0.58	6.00 ± 0.02	1.38	3.16
M_\star	$\approx 40 M_\odot$	M_{nb}	4.66 ± 0.1	5.53 ± 0.02	1.09	1.51
$M_{\text{circ.st.}}$	$\approx 0.1 M_\odot^{\text{d}}$	$N_{11.9}$	11.59 ± 0.6	0.54 ± 0.03	21.88	21.88
L	$\approx 2.3 \times 10^5 L_\odot$	Q1	17.75 ± 0.4	-1.85 ± 0.03	51.69	51.69

Table 1.3: Basic properties and near-/mid-infrared fluxes of IRS 9A from Nürnberg (2003). Values for J', H and K' taken with NIRCAM at the Las Campanas Observatory 2.5 m telescope, L and M_{nb} from ISAAC at the VLT, $N_{11.9}$ and Q1 from TIMMI 2 at the La Silla Observatory 3.6 m telescope. (a) apparent magnitudes, not corrected for extinction, (b) corrected for foreground extinction of $A_V = 4.5$ mag towards the central cluster of NGC 3603, (c) corrected for $A_V = 20$ mag, (d) lower limit.

2 Optical interferometry

2.1 Angular resolution – why interferometry?

Since the distances between the stars, galaxies and all the other objects populating the universe are amazingly large, their apparent size in the sky is very small and astronomers have always been busy trying to increase the angular resolution of their telescopes. One of the many outcomes of this are today's interferometers. Before discussing these instruments in more detail, a brief introduction to angular resolution in astronomy in general is given. Broadly speaking, there are three things that limit our ability to investigate astronomical objects at high spatial resolution:

- The wave nature of light
- Earth's atmosphere
- The size of the telescope

It is due to the first point that even an ideal telescope will not produce a perfect image of an object, because light passing through an aperture is diffracted and produces an interference pattern on a screen or a detector at some distance behind the aperture. The exact shape of this interference pattern depends on the shape and size of the aperture and on the observing wavelength. For the case of a uniformly illuminated circular aperture, e.g. an ideal single telescope observing a point source from space, this is the well known *Airy pattern* shown as a computer generated example in Figure 2.1 to the right. In order to enhance the otherwise very faint outer rings, the figure shows the square root of the Airy pattern. If D denotes the diameter of the aperture / telescope mirror and θ the radial (angular) coordinate, the function describing the Airy pattern can be written as follows:

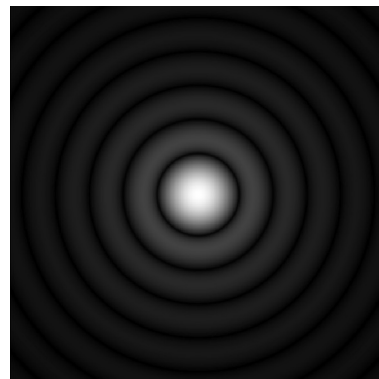


Figure 2.1: The square root of an artificial Airy pattern

$$F_{\text{Airy}} = I_0 \left(\frac{2J_1(\pi\theta D/\lambda)}{\pi\theta D/\lambda} \right)^2, \quad (2.1)$$

where J_1 denotes the Bessel function of the first kind of order one and I_0 the intensity in the centre of the distribution (see for example Born & Wolf 1999 for a derivation).

The first dark ring lies at the first null of $J_1(x)/x$, which is given by $x \approx 3.8317$. This leads to the definition of the *Rayleigh criterion* for the angular resolution of an image-forming device: two distinguishable objects in an image (for example two point sources) are said to be resolved if the position of the maximum of the Airy pattern of the first object coincides with the position of the first minimum of the second Airy pattern. Therefore, using $x = \pi\theta D/\lambda \approx 3.8317$, we obtain for the spatial resolution of a single telescope with a circular aperture:

$$\Theta_{\text{tel}} = 1.22 \frac{\lambda}{D} \text{ rad.} \quad (2.2)$$

Thus, although still dependent on the wavelength and the size of the telescope's mirror or lens, the highest achievable resolution is ultimately limited by diffraction, that is, the wave nature of light.

The second point in the list, Earth's atmosphere, is a severe problem for most of astronomy but it is also the only point in the list where the limiting effects on the spatial resolution can be completely removed. First of all, the atmosphere blocks long wavelength radio waves, most of the infrared spectrum, as well as ultraviolet radiation, X-rays and gamma rays. Secondly the wave fronts from the parts of the electromagnetic spectrum which do reach the ground are distorted by the atmosphere. This is due to turbulence which causes the column density of air to vary between two slightly different paths, which then leads to different effective path lengths. If these differences are not small compared to the observing wavelength, they will lead to significant distortions of the image across the aperture of a telescope. To make things worse, these distortions vary on a time scale which is typically less than 10 ms. The linear scale over which one has to expect such significant differences is called the Fried parameter $r_0(\lambda)$ (Fried 1965). If the aperture of a telescope is larger than r_0 , the details in the image will be blurred and the resolution will be determined by the atmosphere. Since typical values for r_0 are in the range of 10–20 cm in the visible, virtually all modern telescopes only have a resolution comparable to a telescope of this size, unless they possess an adaptive optics (AO) system (see Section 2.11.3). Historically this led to the term “seeing”, describing the obtainable image quality in terms of the full width at half maximum (FWHM) of the seeing disc, also called the point spread function (PSF). Values for the seeing below 1'' are usually considered “good seeing” and at the best observing sites this value can go down to about 0.4'', which, for the case of today's telescopes, is still much larger than the diffraction limit according to equation (2.2).

There is, of course, a way to solve all atmosphere-related problems, namely observing from space. However, this involves a huge effort and great costs, so that today's largest space telescope for the infrared, the *Spitzer Space Telescope*, has a mirror of “only” 0.85 m in diameter. We will return to atmosphere-related problems in Section 2.8, where its influence on the phase of the interferometric signal is discussed, and also in Section 2.10, dealing with problems specific to observations in the infrared, and throughout Chapter 3. For more detailed information about the theory of atmospheric turbulence and the consequences for optical interferometry and high angular resolution astronomy in general,

we refer to Quirrenbach (2000) and the references therein.

The last point, the size of the telescope, is where interferometers come into play. By looking at equation (2.2) (and neglecting the atmosphere for a moment) we see that we can increase the spatial resolution by simply increasing the diameter of the telescope. There are of course limits to that and today's largest optical telescopes have (segmented) mirrors of up to 10 meters. A further significant increase in size is linked with enormous technical challenges and costs, for example for the planned European Extremely Large Telescope (E-ELT). As we will see in Section 2.3, the equation for the resolution of an interferometer is very similar to equation (2.2), but instead of the diameter of the single telescope we have the separation between two telescopes, regardless of their individual diameters. So with two small telescopes separated by a large distance we can achieve a resolution comparable to that of a single telescope with a diameter as large as the separation of the interferometer's telescopes. In this way it is possible to exceed the resolution of the largest single telescopes by more than a factor of ten, unlocking new research areas which were previously not accessible, or at least not at this price. However, these opportunities come along with a significant number of drawbacks, among which are a much higher complexity due to numerous sophisticated subsystems needed for the beam combination, much lower sensitivity and very narrow fields of view. While images can in principle be obtained, the facilities which are currently available do not contain a sufficient number of telescopes to achieve a satisfying result within a reasonable amount of time. Nevertheless, optical interferometry is now in a quite mature state, exploiting its unique potential and producing scientific results of high significance.

2.2 History of the field

This historical review is based on Lawson (2000), Monnier (2003), the presentation "A Brief History of Astronomical Interferometry in the Optical" given at the 2003 Michelson Interferometry Summer School by Gerard van Belle and the presentation "Optical Interferometry – Motivation and History" given at the 2006 Michelson Summer Workshop by Peter Lawson.

The earliest works in this field date back to the 19th century, when in 1868 Armand Hippolyte Louis Fizeau was the first to suggest that "it is perhaps allowed to hope" to make use of interference fringes to measure the angular diameter of stars (Fizeau 1868). Only a few years later, between 1872 and 1873, the director of the Marseilles Observatory, Édouard Jean-Marie Stephan, picked up the idea of Fizeau and performed the first interferometric measurements of stars. He used the 80 cm reflector built by Foucault, the biggest reflecting telescope at that time, but could only derive an upper limit of $0.158''$ for the stellar diameters (Stephan 1874). In 1890 Albert Abraham Michelson gave the first thorough mathematical description of stellar interferometry (Michelson 1890), most likely unaware of Fizeau's earlier work. In the following year Michelson measured the angular diameters of the Galilean moons (Michelson 1891) and in 1921, together with

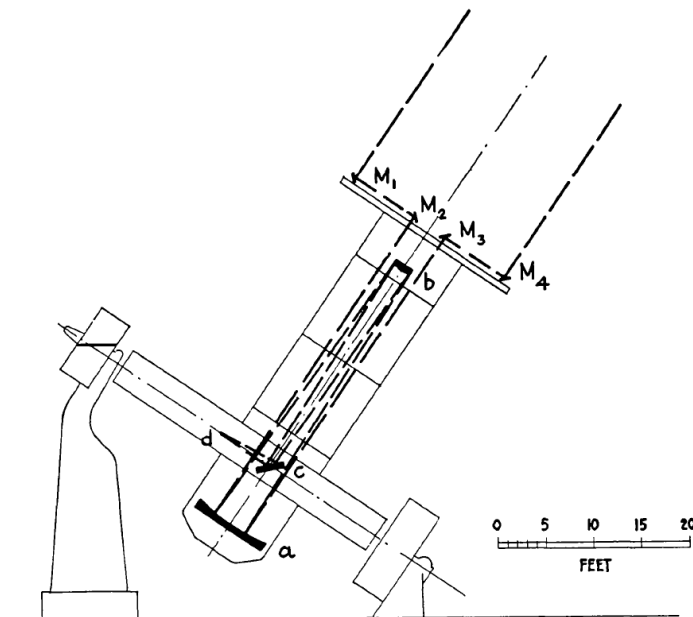


FIG. 1.—Diagram of optical path of interferometer pencils. M_1 , M_2 , M_3 , M_4 , mirrors; a , 100-inch paraboloid; b , convex mirror; c , coudé flat; d , focus.

Figure 2.2: Sketch of the 20-foot interferometer on Mt. Wilson. The steel structure visible at the end of the Cassegrain cage carries the four additional 6-inch mirrors M_1 to M_4 which are used to reduce the separation of the two beams. They are then combined by the telescope. Taken from Michelson & Pease (1921)

Francis Gladheim Pease, he measured the diameter of Betelgeuse with the 20-foot interferometer on Mt. Wilson (Michelson & Pease 1921). This was the first measurement of the diameter of a star other than the sun and they found it to be $0.047''$. A sketch of the 20-foot interferometer is shown in Figure 2.2.

The 20-foot interferometer was followed by the 50-foot interferometer, which was built by Pease and George Ellery Hale in 1931. Unlike its precursor it was not a very successful experiment, suffering from various technical problems. This led to very little activity in the field from 1922 to 1968, with only a few unrefereed letters from Pease and some measurements of binary stars. While there was virtually no activity in the optical arena during this time, a rapid development of radio interferometry took place. This was due to progress in radar during World War II and the first radio interferometer was built by Ryle and Vonberg in 1946. In 1956 Hanbury Brown and Twiss described the basic principle behind intensity interferometry (Hanbury Brown & Twiss 1956a). This technique is different to the one used by Michelson, and due to much lower demands on the quality of the optical equipment allows for larger baselines. They published their first results obtained from experiments at Jodrell Bank in the same year (Hanbury Brown & Twiss 1956b), reporting an estimate of the diameter of Sirius. This unexpected success led to the construction of the Narrabi intensity interferometer in New South Wales, Australia, starting in 1962. Optimised for blue light and with a maximum baseline of 188 m, it had

1970	– Speckle interferometry invented (Labeyrie 1970)
1972	– First fringes with heterodyne receivers operating at a wavelength of $\approx 10\ \mu\text{m}$ (Gay & Journet 1973)
1974	– Heterodyne fringes obtained with separated telescopes observing the limb of Mercury (Johnson et al. 1974)
1974	– Direct detection (electric fields combined before photon detection) of fringes on Vega with a 12 m baseline in the visible (Labeyrie 1975)
1979	– Fringe measurements with the first fringe-tracking interferometer (Shao & Staelin 1980)
1982	– First fringe measurements at $2.2\ \mu\text{m}$ (di Benedetto & Conti 1983)
1985	– Closure phase measured in the optical (Baldwin et al. 1986)
1986	– Mark III stellar interferometer, the first fully automated interferometer for astrometry (Shao et al. 1988)
1991	– Use of single-mode fibres (Coudé du-Foresto & Ridgway 1992)
1995	– First true image from an interferometric array of optical telescopes (Baldwin et al. 1996)

Table 2.1: Milestones in optical and near-IR interferometry from 1970 to 1995. See Lawson (2000).

a huge impact on the field of optical interferometry. The measurement of the diameter of 32 stars ranging in spectral type from O to A to a limiting magnitude of $B = +2.5$ mag at an accuracy of 1–2 percent remains the seminal paper on diameters of main sequence stars to this day (Hanbury Brown et al. 1974).

Due to advances in both technology and theory, a great reawakening of the field took place in the 1970s. The milestones on the way towards modern optical and near-IR interferometry are listed chronologically in Table 2.1. Since this chapter is meant to give an overview of the most important historical events, the most recent developments and current facilities will not be described (except for the VLTI in Section 2.11). Today there are nine operational ground-based interferometers, several new projects are under construction or development, half a dozen projects are being studied and there are also plans for interferometers in space. For a complete overview and links to the individual observatories we refer to the “Optical Long Baseline Interferometry News” website (OLBIN¹), edited by Peter Lawson at NASA-JPL.

2.3 Basic principles of optical interferometry

In the following chapters the basic aspects of optical interferometry will be described in the way that is customary in astronomy, i.e based solely on the classical wave theory. This

¹<http://olbin.jpl.nasa.gov/index.html>

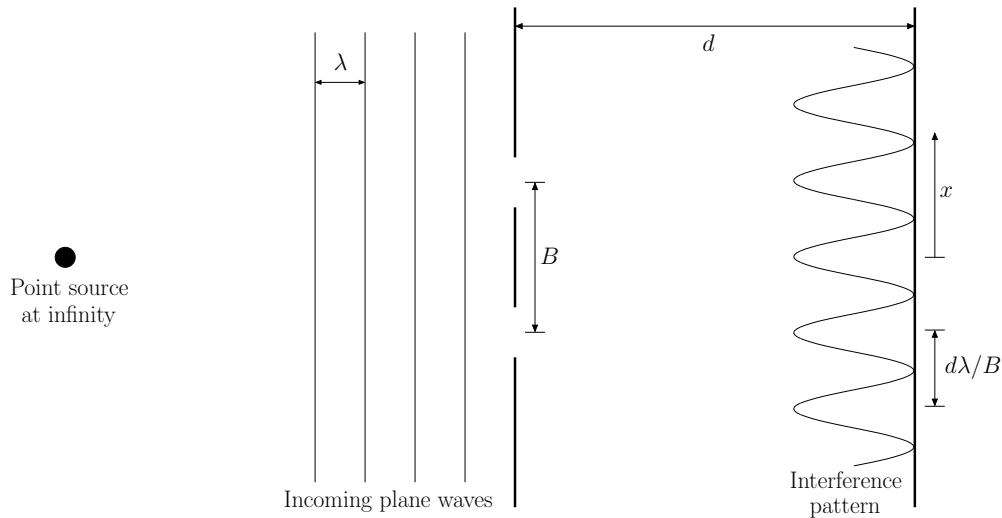


Figure 2.3: Sketch of Young’s double-slit experiment for the case of monochromatic light and a point source at infinity.

approach suffices in order to understand (and build) today’s interferometers, and is treated in detail in the book by Born & Wolf (1999), whose first edition was published in 1959, the year before the laser was invented. However, the experiments and discoveries in the 1960s and 70s led to the development of a whole new field, now known as *quantum optics*, dealing with the subject of coherence and fluctuations of light. We refer to the book by Mandel & Wolf (1995) for an extensive description of the field, but will not discuss its implications for astronomical interferometers.

The basic principles behind optical interferometry can be illustrated by the famous double-slit experiment performed by Thomas Young in 1801. It successfully demonstrated the wave nature of light, in contrast to the then well established “corpuscular” theory of Newton. Figure 2.3 shows a sketch of the double-slit experiment which is inspired by Figure 1 of Monnier (2003). The design differs slightly from the original setup used by Young, but the conclusions are the same and the similarity to astronomical interferometers is more obvious. Monochromatic light from a point source at infinity impinges on an opaque wall with two slits, separated by a “baseline” B . The light behind the wall is projected on a screen and an interference pattern can be observed, which consists of bright and dark bands called *interference fringes*. They are equidistant and oriented perpendicular to the direction of the baseline. The *fringe contrast*, that is, the difference of the maximum and the minimum intensity divided by their sum, is equal to one.

Whether the interference on the screen is constructive or destructive depends on the relative path lengths from the slits to the position x on the screen. Assuming the screen to be far away from the two slits, i.e., $x \ll d$ and $B \ll d$, we can write for the difference between the two path lengths:

$$\Delta s \approx B \frac{x}{d}. \quad (2.3)$$

Maxima of the interference pattern will occur whenever Δs is an integral multiple of the wavelength λ , whereas minima occur whenever Δs is an odd numbered multiple of half the wavelength. So we can write:

$$x_{\max,n} = n\lambda \frac{d}{B}, \quad \text{and} \quad x_{\min,n} = \frac{2n+1}{2} \lambda \frac{d}{B}, \quad (2.4)$$

for $n \in \mathbb{N}$. The distance between two neighbouring maxima or minima on the screen is $d\lambda/B$, as already indicated in Figure 2.3. If we divide this by the distance d we obtain the fringe spacing in radians:

$$\text{fringe spacing} = \frac{\lambda}{B} \text{ rad}. \quad (2.5)$$

Now we can define the angular resolution of an interferometer in a similar way as we already did for a single telescope in Section 2.1. Two point sources are said to be resolved by an interferometer if the fringe contrast at the longest baseline reaches zero (Born & Wolf 1999; Monnier 2003). Obviously, this is the case when the two fringe patterns of the point sources are out of phase by 180 degrees, resulting in a uniformly illuminated screen/detector. This happens if the point sources are separated by an angle of $\lambda/2B$ in the sky. Therefore we note as the angular resolution of an interferometer:

$$\Theta_{\text{int}} = \frac{\lambda}{2B} \text{ rad}. \quad (2.6)$$

It is interesting to compare this with the resolution of the single telescope given in equation (2.2). By setting $\Theta_{\text{tel}} = \Theta_{\text{int}}$ we obtain $D = 2.44B$, that is, the diameter of the single telescope would have to be roughly 2.5 times larger than the baseline of the interferometer in order to resolve the same binary. One has to keep in mind, however, that the sensitivity is still limited by the area of the telescope(s).

The inverse of the fringe spacing (2.5) is the fringe spatial frequency, giving the number of fringes per unit angle. We denote it with u and write:

$$u = \frac{B}{\lambda} \text{ rad}^{-1}. \quad (2.7)$$

We now move from this instructive but very simple picture towards a more realistic (but still idealised) case. Figure 2.4 shows a sketch of a two-telescope interferometer containing all the necessary components in order to obtain fringes on an astronomical target. The light from a distant source is collected by the two telescopes A and B which are separated by an on-ground baseline vector \vec{B} . Since the source is not at zenith, there is a difference δ between the path lengths from the source to the two telescopes. This difference can be expressed as the scalar product of the unit vector \hat{s} , pointing towards the source, and the baseline vector \vec{B} :

$$\delta = \hat{s} \cdot \vec{B}. \quad (2.8)$$

It has to be corrected with delay lines, because, for the realistic case of non-monochromatic light, we will not receive any fringes if δ is much larger than a few wavelengths

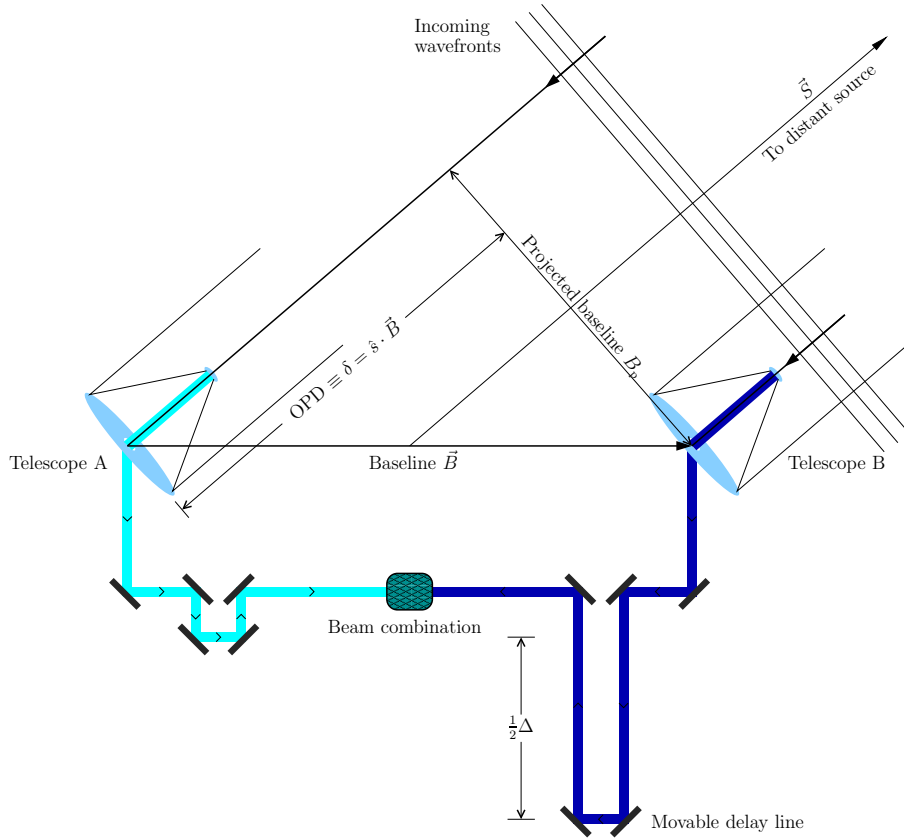


Figure 2.4: Sketch of a two-element interferometer with delay lines (OPD = optical path difference $\equiv \delta$, $\hat{s} = \vec{S}/|\vec{S}|$). See text for details.

(see Section 2.6). The delay lines are available for both telescopes in order to ensure that the same number and type of reflections occur in each beam. In Figure 2.4 the delay line belonging to telescope B introduces an optical delay Δ with respect to the other beam. For the case of $\delta = \Delta$ the optical path difference (OPD) between the two beams is zero, as if the source were at zenith. Due to the rotation of the earth the OPD has to be continually adjusted with high accuracy (see Section 2.11.2 for some numbers from the delay lines of the VLTI). As seen from the source, the telescopes are only separated by the projected baseline B_{proj} . Its length determines the achievable angular resolution and since it is generally time-dependent, just like the OPD, so is the resolution of the interferometer. Finally the two beams are brought to interference with a beam combiner and the resultant electromagnetic fields can be measured.

What do these electromagnetic fields look like? The electric field vector of a plane wave can be written as follows (e.g. Jackson 1998):

$$\vec{E}(\vec{x}, t) = E e^{i(\vec{k} \cdot \vec{x} - \omega t)} = E e^{i(k\hat{n} \cdot \vec{x} - \omega t)}, \quad (2.9)$$

with wave vector $\vec{k} = k\hat{n} = 2\pi\hat{n}/\lambda$, the direction of propagation \hat{n} and the angular fre-

quency $\omega = 2\pi\nu$. If the two telescopes in Figure 2.4 are located at positions \vec{x}_A and \vec{x}_B respectively, then the baseline vector \vec{B} is nothing more than:

$$\vec{B} = \vec{x}_B - \vec{x}_A. \quad (2.10)$$

Following Boden (2000), but using the electrical field vector \vec{E} in order to describe the monochromatic light from the source, the incident radiation at the telescopes A and B can be written as:

$$\vec{E}_A = E_A e^{-i(k\hat{s}\cdot\vec{x}_A + \omega t)} \quad (2.11)$$

$$\begin{aligned} \vec{E}_B &= E_B e^{-i(k\hat{s}\cdot\vec{x}_B + \omega t)} \\ &\stackrel{(2.10)}{=} E_B e^{-i(k\hat{s}\cdot\vec{x}_A + k\hat{s}\cdot\vec{B} + \omega t)}. \end{aligned} \quad (2.12)$$

The common phase factor $e^{-i(k\hat{s}\cdot\vec{x}_A)}$ can be absorbed into any normalisation we choose for the optical fields. Thus, without loss of generality and using (2.8) we can write:

$$\vec{E}_A = E_A e^{-i\omega t} \quad (2.13)$$

$$\vec{E}_B = E_B e^{-i(k\delta + \omega t)}, \quad (2.14)$$

that is, the phase difference at the locations of the two telescopes is simply determined by δ , as expected when neglecting the effects of the atmosphere. At the beam combiner we have the additional phase shift Δ from the delay line, so here (2.14) becomes:

$$\vec{E}_B = E_B e^{-i[k(\delta - \Delta) + \omega t]}. \quad (2.15)$$

Now we can write for the time-averaged detected signal I_{det} :

$$\begin{aligned} I_{\text{det}} &= \left| \vec{E}_A + \vec{E}_B \right|^2 \\ &= (\vec{E}_A + \vec{E}_B) \times (\vec{E}_A^* + \vec{E}_B^*) \\ &= \vec{E}_A^2 + E_A E_B e^{ik(\delta - \Delta)} + E_A E_B e^{-ik(\delta - \Delta)} + \vec{E}_B^2 \\ &= I_A + 2\sqrt{I_A I_B} \cos[k(\delta - \Delta)] + I_B \\ &= 2I \{1 + \cos[k(\delta - \Delta)]\}, \end{aligned} \quad (2.16)$$

where the last step requires that the intensities of the two beams are equal: $I_A = I_B =: I$. Thus the detected signal varies between zero and two times the signal from one of the single telescopes, depending on the net delay $\delta - \Delta$. So just like in Young's double-slit experiment we obtain fringes and the question arises of how the measured fringe pattern is related to the structure of the observed source in the sky.

2.4 Visibility and the van Cittert-Zernike theorem

In Section 2.3 we already mentioned the fringe contrast which, for historical reasons, is called the *visibility*. For the simple case of the double-slit experiment with monochromatic

light the visibility is just the ratio of the difference and the sum of the maximum and the minimum intensity, that is, a real number. In general this is not the case and the visibility is a complex quantity, exhibiting an amplitude and a phase. Therefore, following Quirrenbach (2001), we write for the complex visibility Γ :

$$\Gamma = Ve^{i\phi}. \quad (2.17)$$

This visibility is the prime observable of a Michelson interferometer.

There is a very important theorem in optics which, under certain assumptions, relates the intensity function of a source to the complex visibility. It is known as the van Cittert-Zernike theorem and was first established by P. H. van Cittert (van Cittert 1934) and later by F. Zernike (Zernike 1938). A complete derivation can also be found in Born & Wolf (1999). Simply speaking, the visibility is proportional to the Fourier transform of the brightness distribution of the source. More precisely, the theorem states that the amplitude and phase of the visibility are exactly proportional to the amplitude and phase of the Fourier component of the image which corresponds to the fringe spatial frequency B/λ defined in (2.7). Thus, a single interferometric observation of an object measures a single component of the Fourier transform of the brightness distribution of this object.

Figure 2.5 to the right shows a sketch of the relevant coordinate systems. The source is located in the direction indicated by the vector \vec{S} and is assumed to be far away. If it emits light over only a very small area of the sky, we can use the Cartesian coordinates x and y instead of the spherical coordinates of right ascension and declination which are normally used and indicated in the figure with thin lines. The plane defined by x and y is parallel to the one defined by u and v . Thus, while x and y are used to describe the brightness distribution of the source in the sky, u and v denote the sampled Fourier component of the image which is defined by the components of the baseline vector \vec{B} projected onto this plane (the fringe spatial frequencies):

$$u = \frac{B_u}{\lambda}, \quad \text{and} \quad v = \frac{B_v}{\lambda}, \quad (2.18)$$

where B_u and B_v are the components of the baseline vector which are parallel to u and v , respectively. They are measured in units of the observing wavelength λ . The van Cittert-Zernike theorem can now be written as:

$$\Gamma(u, v) = V(u, v) e^{i\phi} = \frac{\iint I(x, y) e^{-2\pi i(ux+vy)} dx dy}{\iint I(x, y) dx dy}, \quad (2.19)$$

with $I(x, y)$ being the intensity of the source. The Fourier transform is normalised so that $\Gamma(u = 0, v = 0) = 1$, in agreement with the visibility of an unresolved source.

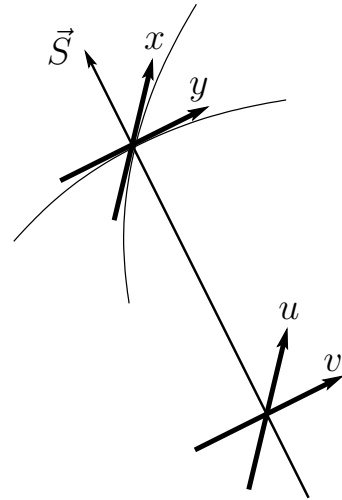


Figure 2.5: Coordinate systems for interferometric observations.

According to the theorem we can recover the brightness distribution of the source via a simple inverse Fourier transform. Of course, this requires that we know the left hand side of equation (2.19), or at least we need a sufficient number of sampled points in the u - v -plane. As already mentioned in Section 2.1, this is not feasible with the current generation of optical interferometers as it would simply take too much time. The interpretation of interferometric data in the optical is therefore still limited to parametric model fitting (but see the recent paper by Raban et al. 2009).

It is instructive to compare the operation of an interferometer with that of a single telescope. This is done, for example, in Dyck (2000). A single telescope is able to provide precise images because its single mirror provides a continuum of interferometric baselines, covering all sizes in the range from zero to the diameter of the telescope and all possible position angles. Since a single (projected) baseline at a certain position angle leads to one sampled point in the u - v -plane, a single telescope with aperture D will map all points in the Fourier plane up to the maximum spatial frequency D/λ .

2.5 Image-plane and pupil-plane interferometers

With respect to the combination of the beams, all interferometers can be divided into two groups: image-plane or “Fizeau” interferometers and pupil-plane or “Michelson” interferometers (see for example Traub 2000). The former type is named after Fizeau because he was the first to suggest the idea of converting an ordinary telescope into an interferometer using a mask with two slits (see Section 2.2 and Fizeau 1868). The name of the latter type originates in the famous experiment conducted by Michelson at the end of the 19th century, showing that the speed of light is independent of the velocity of the observer.

In image-plane interferometry the single beams from each telescope are focused in order to produce images of the observed area of the sky and these images are then superposed at the same position on a detector. The interference pattern is then spread across the combined image and the visibility can be measured. The AMBER (Astronomical Multi-BEam combineR) instrument is built as an image-plane interferometer and the technique is schematically illustrated for two telescopes on the left side of Figure 2.6.

In a pupil-plane interferometer the beams are superposed with a beam splitter (e.g. a half-silvered mirror) and the combined beams are focused on different detectors or different parts of the same detector. The fringe signal is then modulated in time by varying the OPD around the point of zero-OPD, causing the intensities of the combined beams to vary with opposite signs. This is caused by the fact that, due to energy conservation, the beam splitter introduces a phase shift of $\pi/2$ between the reflected and transmitted beam (Traub 2000). We will come back to this in Section 3.1. Measuring the amplitude of the time-modulated fringe signals gives the visibility. MIDI uses the technique of pupil-plane beam combination which is illustrated on the right side of Figure 2.6 (compare with the actual optical layout of MIDI in Figure 3.1).

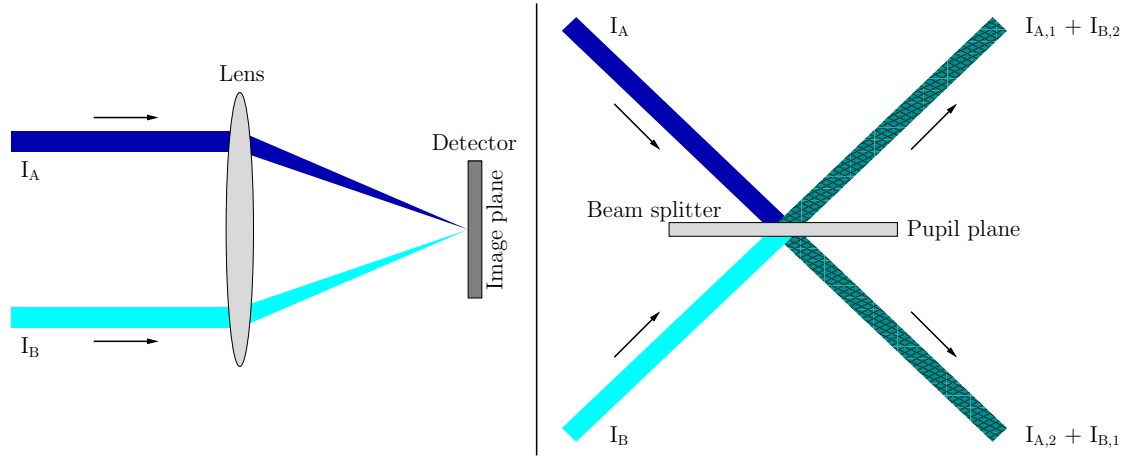


Figure 2.6: The two different types of beam combination for the case of a two-telescope interferometer: image-plane on the left and pupil-plane on the right.

Hence, when designing an interferometer, one has to choose either to measure the visibility pattern modulated in space (image-plane) or in time (pupil-plane). Assuming an ideal interferometer the results should not be different.

Since MIDI is a pupil-plane combiner we take a closer look at the intensities and electrical fields, following Chapter 8.3.2 of Thorsten Ratzka's PhD thesis (Ratzka 2005) and the short manual "Measuring Visibilities with MIDI" by Rainer Köhler which is part of the MIA+EWS data reduction software, but also directly available². Using the same nomenclature as in Figure 2.6 and taking the phase shift of $\pi/2$ into account, the combined beams/fields can be written as follows:

$$I_1 \equiv I_{A,1} + I_{B,2} = \left| \vec{E}_{A,1} + \vec{E}_{B,2} e^{-i\pi/2} \right|^2 \quad (2.20)$$

$$I_2 \equiv I_{A,2} + I_{B,1} = \left| \vec{E}_{A,2} e^{-i\pi/2} + \vec{E}_{B,1} \right|^2, \quad (2.21)$$

where the individual fields are $\vec{E}_{A,1} = E_{A,1} e^{i\phi_A}$, $\vec{E}_{A,2} = E_{A,2} e^{i\phi_A}$, $\vec{E}_{B,1} = E_{B,1} e^{i\phi_B}$ and $\vec{E}_{B,2} = E_{B,2} e^{i\phi_B}$. Then the intensities are:

$$\begin{aligned} I_1 &= (\vec{E}_{A,1} + \vec{E}_{B,2} e^{-i\pi/2}) \times (\vec{E}_{A,1}^* + \vec{E}_{B,2}^* e^{i\pi/2}) \\ &= |\vec{E}_{A,1}|^2 + E_{A,1} E_{B,2} e^{i(\phi_A - \phi_B + \pi/2)} + E_{B,2} E_{A,1} e^{-i(\phi_A - \phi_B + \pi/2)} + |\vec{E}_{B,2}|^2 \\ &= I_{A,1} + 2E_{A,1} E_{B,2} \cos(\phi_A - \phi_B + \pi/2) + I_{B,2} \\ &= I_{A,1} - 2E_{A,1} E_{B,2} \sin(\phi_A - \phi_B) + I_{B,2}, \end{aligned} \quad (2.22)$$

$$\begin{aligned} I_2 &= (\vec{E}_{A,2} e^{-i\pi/2} + \vec{E}_{B,1}) \times (\vec{E}_{A,2}^* e^{i\pi/2} + \vec{E}_{B,1}^*) \\ &= I_{A,2} + 2E_{A,2} E_{B,1} \sin(\phi_A - \phi_B) + I_{B,1}. \end{aligned} \quad (2.23)$$

²<http://www.strw.leidenuniv.nl/~koehler/MIA+EWS-Manual/Visibility.pdf>

Note the different sign in front of the sine term, which causes I_1 and I_2 to vary in an opposite way, depending on the phase difference $\phi_A - \phi_B$. If we assume a “perfect” 50:50 beam splitter and equal intensities of the two beams, we find for the constant terms in (2.22) and (2.23):

$$I_{A,1} = I_{A,2} = I_A/2, \quad I_{B,1} = I_{B,2} = I_B/2, \quad \text{and} \quad I_A = I_B =: I, \quad (2.24)$$

that is, the intensities of the two interferometric beams vary between zero and two times the intensity of a single beam, one being at its maximum when the other is zero. We can determine the interferometric signal by simply subtracting I_1 and I_2 from each other:

$$\begin{aligned} I_{\text{int}} := I_2 - I_1 &= (2E_{A,2}E_{B,1} + 2E_{A,1}E_{B,2}) \sin(\phi_A - \phi_B) \\ &= (2\sqrt{I_A I_B/4} + 2\sqrt{I_A I_B/4}) \sin(\phi_A - \phi_B) \\ &= 2I \sin[k(\delta - \Delta)], \end{aligned} \quad (2.25)$$

where we replaced the phase difference between the two beams by the OPD from Section 2.3. The assumptions of a perfect beam splitter and equal intensities of the two beams are, of course, unrealistic, but these effects are taken into account when analysing MIDI data and the qualitative result is the same.

2.6 Non-monochromatic light – finite bandwidth

So far we have always used monochromatic light in our calculations, which led to the appearance of fringes regardless of the OPD (“infinite fringes”). Since every object emits light over a range of wavelengths and every detector has a finite passband, we have to determine how this impacts the interferometric signals. To further complicate the situation, the intensity of a source is generally wavelength-dependent, and so is the filter function of the instrument. Thus, for the general case, we have to modify equation (2.25) accordingly, but instead of the wavelength we use the frequency in order to simplify the calculations. Following Boden (2000) and Ratzka (2005) we write for the interferometric signal in the polychromatic case:

$$I_{\text{int}} = 2 \int I(\nu) \eta(\nu) \sin[k(\delta - \Delta)] d\nu, \quad (2.26)$$

where $\eta(\nu)$ is the filter function of the instrument. In order to calculate the integral we will make two simplifying assumptions: we presume the intensity of the source to be constant across the passband of the instrument and the filter function to be described by a top-hat function, with constant throughput in the interval $\bar{\nu} \pm \Delta\nu/2$:

$$\eta(\nu) = \begin{cases} \eta_0 & \text{if } \bar{\nu} - \frac{\Delta\nu}{2} \leq \nu \leq \bar{\nu} + \frac{\Delta\nu}{2} \\ 0 & \text{otherwise.} \end{cases} \quad (2.27)$$

Now equation (2.26) becomes:

$$\begin{aligned}
 I_{\text{int}} &= 2I(\bar{\nu}) \eta_0 \int_{\bar{\nu}-\Delta\nu/2}^{\bar{\nu}+\Delta\nu/2} \sin[2\pi\nu(\delta-\Delta)/c] d\nu \\
 &= 2I(\bar{\nu}) \eta_0 \left[-\frac{c}{2\pi(\delta-\Delta)} \cos[2\pi\nu(\delta-\Delta)/c] \right]_{\bar{\nu}-\Delta\nu/2}^{\bar{\nu}+\Delta\nu/2}.
 \end{aligned} \tag{2.28}$$

$$\tag{2.29}$$

Evaluating the right hand side and using the following identity:

$$\cos(a) - \cos(b) = -2 \sin\left(\frac{a+b}{2}\right) \sin\left(\frac{a-b}{2}\right), \tag{2.30}$$

we get:

$$\begin{aligned}
 I_{\text{int}} &= 2I(\bar{\nu}) \eta_0 \frac{c}{2\pi(\delta-\Delta)} 2 \sin\left(\frac{2\pi(\delta-\Delta)\bar{\nu}}{c}\right) \sin\left(\frac{\pi(\delta-\Delta)\Delta\nu}{c}\right) \\
 &= 2I(\bar{\nu}) \eta_0 \Delta\nu \sin\left(\frac{2\pi(\delta-\Delta)\bar{\nu}}{c}\right) \frac{\sin\left(\frac{\pi(\delta-\Delta)\Delta\nu}{c}\right)}{\frac{\pi(\delta-\Delta)\Delta\nu}{c}} \\
 &= 2I(\bar{\nu}) \eta_0 \Delta\nu \sin[\bar{k}(\delta-\Delta)] \text{sinc}[\Delta k(\delta-\Delta)/2],
 \end{aligned} \tag{2.31}$$

where in the last step we have replaced $\bar{\nu}$ and $\Delta\nu$ with \bar{k} and Δk , respectively, and introduced the sinc function, which is defined by $\text{sinc}(x) := \sin(x)/x$. The leading coefficient of (2.31) is the total collected power by the two telescopes (with efficiency η_0 and in the bandwidth $\Delta\nu$). Just as in the monochromatic case, the signal oscillates with respect to the optical path difference, but now it is modulated by the sinc function, which becomes small if its argument is larger than one. Therefore, in contrast to equations (2.16) and (2.25), we only observe fringes if the OPD is sufficiently close to zero. This is often described by a characteristic scale length, namely the *coherence length*, which we obtain if we replace Δk by $\Delta\lambda$ in (2.31):

$$\begin{aligned}
 I_{\text{int}} &= 2I(\bar{\nu}) \eta_0 \Delta\nu \sin[\bar{k}(\delta-\Delta)] \text{sinc}\left[\pi(\delta-\Delta)\Delta\lambda/\bar{\lambda}^2\right] \\
 &= 2I(\bar{\nu}) \eta_0 \Delta\nu \sin[\bar{k}(\delta-\Delta)] \text{sinc}\left[\pi(\delta-\Delta)/\Lambda^2\right],
 \end{aligned} \tag{2.32}$$

where $\bar{\lambda} = c/\bar{\nu}$ is the wavelength in the centre of the passband and the coherence length is defined as $\Lambda = \bar{\lambda}^2/\Delta\lambda$. Since MIDI works in the range from 7.5 μm to 13.5 μm , the coherence length is roughly 20 μm or $2\bar{\lambda}$. Three examples for the interferometric signal in the polychromatic case (with different values for Λ) are shown in Figure 2.7. Obviously, for OPDs much larger than the coherence length, the detection of interferometric fringes is impossible. It is interesting to note that the sinc function is the Fourier transform of a top-hat function, that is, the filter function of the instrument.

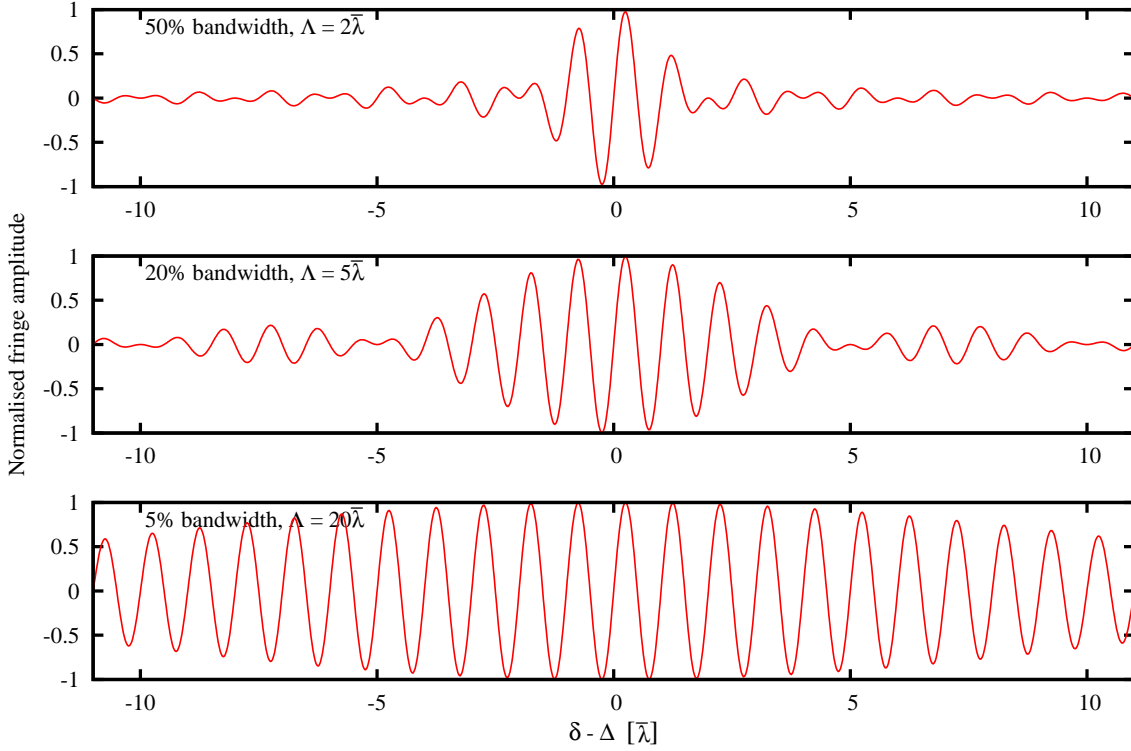


Figure 2.7: Three examples for the fringe signal in the polychromatic case. The OPD $\delta - \Delta$ is in units of the central wavelength $\bar{\lambda}$ and the fringe signal is normalised. From top to bottom: $\Delta\lambda = 0.5\bar{\lambda}$ (this is roughly the case for MIDI, since $7.5 \mu\text{m} \lesssim \lambda \lesssim 13.5 \mu\text{m}$), $\Delta\lambda = 0.2\bar{\lambda}$ and $\Delta\lambda = 0.05\bar{\lambda}$, i.e., approaching the monochromatic case.

2.7 Extended sources

Since the common goal of interferometric observations is to resolve the structure of sources which are too small to show any deviations from the signal of a point source in observations with a single telescope, we have to consider sources which are resolved by the interferometer. Following Boden (2000) for the monochromatic case, we therefore characterise the intensity of the source as a function of the position in the sky as $F = F(\hat{s})$, where F is usually measured in power per area per solid angle. Using the vector \hat{s}_0 , pointing to some reference position in the direction of the source, and $\Delta\vec{s}$, a small offset from this reference position, we define:

$$\hat{s} = \hat{s}_0 + \Delta\vec{s}. \quad (2.33)$$

In the case of extended sources, or if a point source is not centred in the field of view (FOV) of the telescopes, we also have to take into account that the throughput of the telescopes depends on the position of the source in the sky. We write this as $A(\hat{s})$ which describes the throughput in terms of an effective cross-sectional area, so that $\int A(\hat{s}) F(\hat{s}) d\Omega$ yields the collected power.

The basic idea for extended sources is to assume that the radiation emitted at different places is incoherent, and that we can describe the source as a superposition of coherent point sources at different locations. With δ being a small optical delay between the two arms of the interferometer, the detected power can be written as:

$$\begin{aligned}
 P(\hat{s}_0, \vec{B}, \delta) &= \int A(\Delta\vec{s}) F(\Delta\vec{s}) d\Omega + \cos(k\delta) \int A(\Delta\vec{s}) F(\Delta\vec{s}) \cos(k\Delta\vec{s} \cdot \vec{B}) \\
 &\quad - \sin(k\delta) \int A(\Delta\vec{s}) F(\Delta\vec{s}) \sin(k\Delta\vec{s} \cdot \vec{B}) \\
 &= \int A(\Delta\vec{s}) F(\Delta\vec{s}) d\Omega + \text{Re}\{V\} \cos(k\delta) + \text{Im}\{V\} \sin(k\delta) \\
 &= P_0 + \text{Re}\{V e^{ik\delta}\}, \tag{2.34}
 \end{aligned}$$

where \vec{B} is the baseline vector, $P_0 = \int A(\Delta\vec{s}) F(\Delta\vec{s}) d\Omega$ and the complex visibility:

$$V(k, \vec{B}) = \int A(\Delta\vec{s}) F(\Delta\vec{s}) e^{-ik\Delta\vec{s} \cdot \vec{B}} d\Omega \tag{2.35}$$

was introduced in the second step. This result can be easily compared with the (normalised) visibility given in equation (2.19) in the context of the van Cittert-Zernike theorem. To this end we choose a coordinate system where $\hat{s}_0 = (0, 0, 1)$ and assume that $\Delta\vec{s}$ is approximately perpendicular to \hat{s}_0 . This is the case if the FOV of the interferometer or the angular extent of the source is small. Then we can express $\Delta\vec{s}$ in terms of the angles x and y :

$$\Delta\vec{s} \approx (x, y, 0), \tag{2.36}$$

and together with the spatial frequencies defined in (2.18), the visibility becomes:

$$V(u, v) = \iint A(x, y) F(x, y) e^{-2\pi i(ux+vy)} dx dy. \tag{2.37}$$

This visibility is in units of power and depends on the brightness distribution of the source and the collection efficiencies of the telescopes.

2.8 Atmospheric turbulence and phases

The basic problems which are caused by the atmosphere have already been introduced in Section 2.1. We will now concentrate on how the atmospheric turbulence influences the measurement of the phase of the interferometric signal. A more detailed description of this matter and the strategies used to overcome these difficulties can be found in Monnier (2000) and also in Quirrenbach (2001).

As discussed in Section 2.4, the complex visibility $\Gamma = V e^{i\phi}$ is the prime observable of a Michelson interferometer like MIDI at the VLTI. While the amplitude of the visibility can be recovered directly (after removal of background, instrumental effects, etc.), the

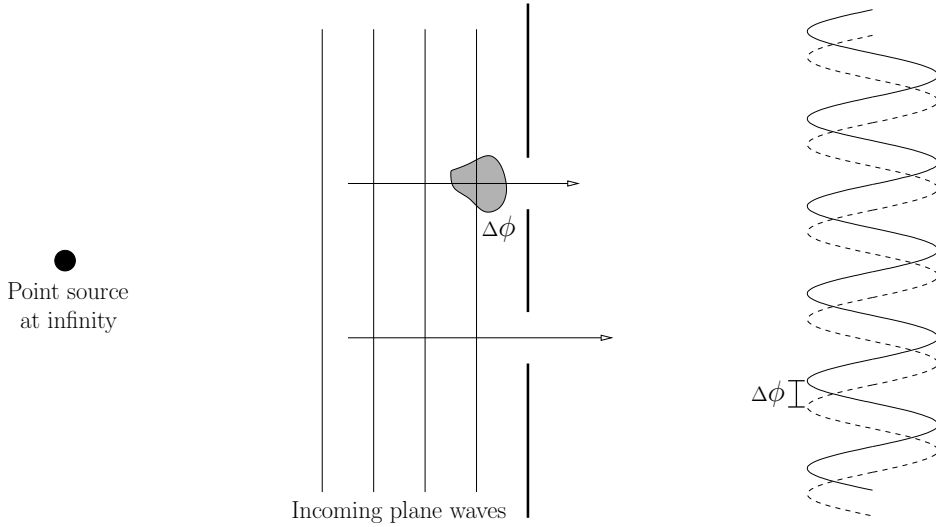


Figure 2.8: Modified version of Young’s double-slit experiment inspired by Figure 1 from Monnier (2000). If the path length above one of the slits is changed, the position of the fringe signal is shifted.

measured phase is a sum of three terms. The intrinsic phase emanating from the structure of the source, the phase distortion due to the atmosphere and the instrumental phase:

$$\phi_m = \phi_s + \phi_a + \phi_i. \quad (2.38)$$

It is due to the the second term, the unknown contribution from the atmosphere, that the intrinsic phase of the visibility cannot be measured.

In order to understand this, we first have a look at Figure 2.8. It is similar to Figure 2.3, but now the path lengths of the two arms of the “interferometer” are different due to a bubble of hot (or cold) air above one of the arms. This extra path length shifts the position of the fringe signal, while the spatial frequency (determined by the slit separation and the wavelength) remains unchanged. For example, if the two path lengths differ by half the wavelength, the fringes will be shifted by half a fringe or π radians. Hence measuring the intrinsic phase of the source is equal to measuring the precise location of the fringe signal on the detector. This task is severely aggravated by the instrumental and atmospheric OPD fluctuations, the latter leading to changes on a time scale of usually less than 10 ms. An estimate of this so-called *coherence time* can be calculated by dividing the Fried parameter $r_0(\lambda)$ by the wind speed.

An obvious solution would be, of course, to average the position of the fringe signal over many observations, with the mean atmospheric phase shift being zero. However, this is not possible if the root mean square (RMS) of the phase shift of ϕ_a is larger than approximately 1 radian. This can be easily understood if we visualise Figure 2.8 for the case of $\Delta\phi = \lambda$. This would shift the fringes by 2π and we would lose track of the fringe we want to measure since this case is not distinguishable from the one with equal path lengths.

According to Monnier (2000), typical atmospheric path length fluctuations are in the range of 5 – 10 μm , that is, in the case of optical interferometers the atmosphere destroys all direct phase information independent of the baseline. There are some strategies to overcome this problem, but since they either require at least three telescopes (closure phases) or were not available during the time of our observations (FINITO, see Section 2.11.3) they will not be discussed here. A different kind of phase information, the so-called “differential phase” will be covered in Section 4.4.4.

2.9 The visibility in a few simple cases

In the ideal case of perfect u - v -sampling and monochromatic light and if the structure of the source is simple enough, for example a point source or a uniform disk, the corresponding visibility can be computed directly. Since these simple source geometries are useful when modelling real interferometric data, the most important ones are presented in this chapter. These are: point source, Gaussian, uniform disk, binary, ring and a disk with an inner hole. We will return to these equations in Chapter 6.

All the aforementioned models are rotationally symmetric, and hence it is useful to describe them in terms of a radius. For the intensity distributions this is the “ordinary” radius r :

$$r = \sqrt{x^2 + y^2}, \quad (2.39)$$

measured in an arbitrary angular unit. The visibilities depend on u and v and we introduce the so-called u - v -radius:

$$r_{u,v} = \sqrt{u^2 + v^2} = \frac{B_{\text{proj}}}{\lambda}, \quad (2.40)$$

measured in the inverse of an arbitrary angular unit. Its length is given by the projected baseline from Section 2.3 and the wavelength of the observation.

2.9.1 Point source

We start with the simplest source, the point source. If the distance to an object is large enough or alternatively if the resolving power of the light collecting instrument is small enough, every source, regardless of its intrinsic size and shape, will appear as a point source. The intensity of a point source located at the centre of the coordinate system with intensity I_0 is simply given by:

$$I_{\text{point}}(x, y) = I_0 \delta(x) \delta(y), \quad (2.41)$$

where $\delta(x)$ and $\delta(y)$ are Dirac delta functions. Inserting this expression into equation (2.19) we immediately get the normalised visibility:

$$V_{\text{point}}(u, v) = 1. \quad (2.42)$$

Thus the visibility of a point source is equal to one, regardless of the baseline or wavelength of the observation. If the point source is offset from the centre, we also get a visibility of amplitude one, but with a linear dependence of the phase on the coordinates u and v .

2.9.2 Gaussian

Another simple and widely used brightness distribution is a Gaussian brightness distribution. It is specified by its FWHM which is normally referred to as σ , but here we use the angular size θ (in arcseconds) instead. At a radial distance of $\theta/2$ from the centre, the intensity is reduced to half of the maximum value. For simplicity we assume the Gaussian brightness distribution to be centred in the FOV so that the intensity is:

$$I_{\text{Gauss}}(r) = I_0 \exp\left(-\frac{4 \ln(2) r^2}{\theta^2}\right). \quad (2.43)$$

The Fourier transform of a Gaussian is again a Gaussian, but narrow distributions lead to wide distributions in the Fourier space and vice versa. The normalised visibility is:

$$V_{\text{Gauss}}(r_{u,v}) = \exp\left(-\frac{(\pi\theta r_{u,v})^2}{4 \ln(2)}\right). \quad (2.44)$$

2.9.3 Uniform disk

The simplest model for a resolved star is a uniform disk (UD), which is described by a top-hat function. The intensity of a uniform disk with diameter θ at the centre of the coordinate system is given by:

$$I_{\text{UD}}(r) = \begin{cases} \frac{4}{\pi\theta^2} & \text{if } r \leq \frac{\theta}{2} \\ 0 & \text{else} \end{cases} \quad (2.45)$$

The Fourier transform of a top-hat function in one dimension is the sinc function (see Section 2.6), while in two dimensions the sine is replaced by a Bessel function:

$$V_{\text{UD}}(r_{u,v}) = 2 \left| \frac{J_1(\pi\theta r_{u,v})}{\pi\theta r_{u,v}} \right|, \quad (2.46)$$

where J_1 again denotes the Bessel function of the first kind and of order one. The intensities and visibilities of a point source, a Gaussian brightness distribution and a uniform disk are illustrated for the one-dimensional case in Figure 2.9.

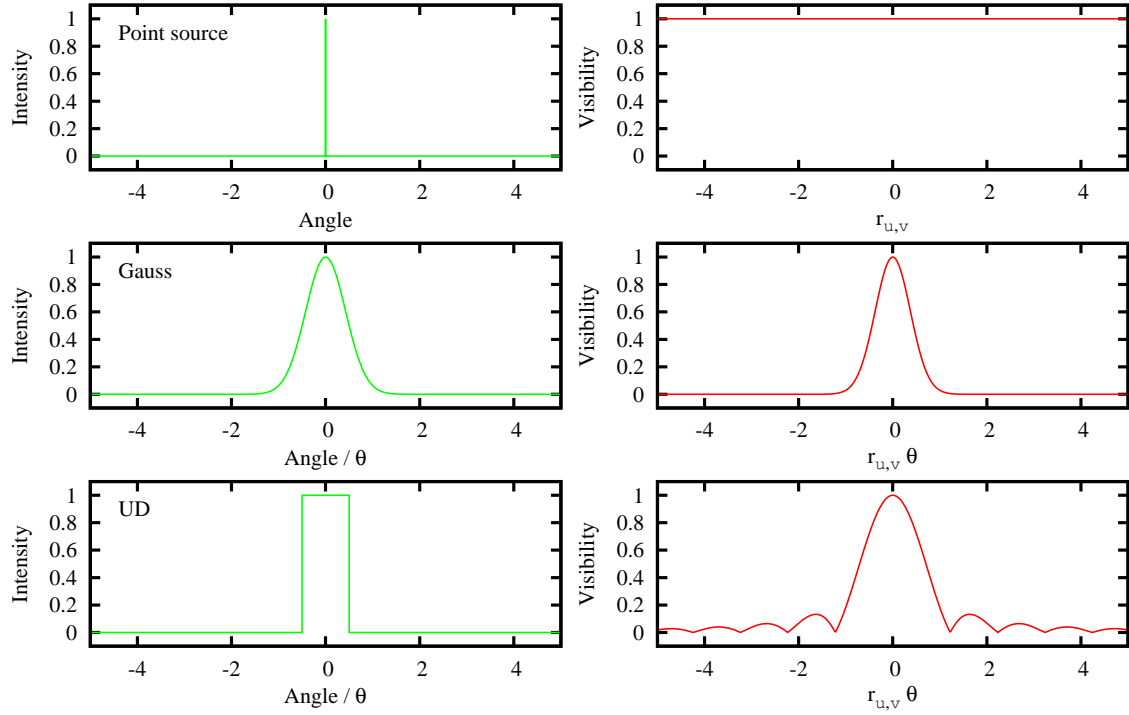


Figure 2.9: The one-dimensional intensities (left) and visibilities (right) of a point source, a Gaussian brightness distribution and a uniform disk. For simplicity, the x-axis is dimensionless in case of the Gauss and UD distributions, i.e., divided by the FWHM (Gauss) and diameter (UD) in real space and multiplied by it in Fourier space. This is, of course, not possible for the point source, and the values on the x-axis denote angle and angle⁻¹ in arbitrary units.

2.9.4 Binary

A binary star is described as the sum of two point sources, each with its own intensity. If the two stars are located at $(-\frac{\theta}{2}, 0)$ and $(+\frac{\theta}{2}, 0)$ respectively, the intensity of the binary is:

$$I_{\text{binary}}(x, y) = I_1 \delta(x + \theta/2) \delta(y) + I_2 \delta(x - \theta/2) \delta(y). \quad (2.47)$$

Let \vec{a} be the separation vector from one star to the other (in the u - v -plane). Then, the visibility of the binary is:

$$V_{\text{binary}}(u, v) = \sqrt{\frac{1 + R^2 + 2R \cos(2\pi\vec{B} \cdot \vec{a}/\lambda)}{(1 + R)^2}}, \quad (2.48)$$

where $R = I_1/I_2$ is the flux ratio of the binary defined such that $R \leq 1$. Thus, for a flux ratio of one the visibility will vary between one and zero, while for lower values of R it will vary between one and $(1 - R)/(1 + R)$. With (2.18) and $\vec{a} = (a_u, a_v)$ we write the argument of the cosine as: $2\pi\vec{B} \cdot \vec{a}/\lambda = 2\pi(ua_u + va_v)$.

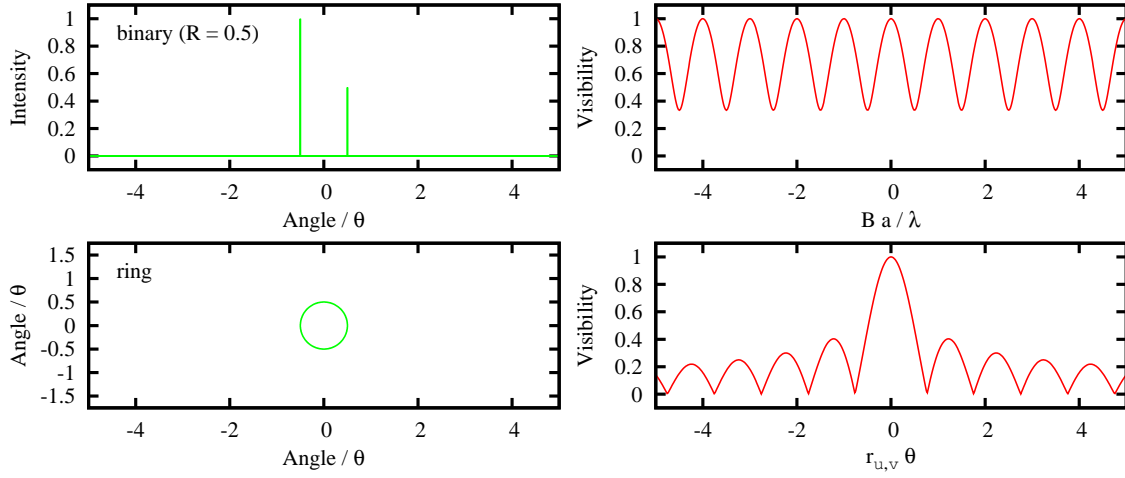


Figure 2.10: The intensities (left) and visibilities (right) of a binary and a ring. The x-axes are again dimensionless, i.e., for the intensity in the case of the binary we divided by the angular separation and in the case of the ring we divided by its diameter. For the visibility of the binary we assumed \vec{B} and \vec{a} to be parallel to each other and we multiplied by the diameter in the case of the ring. Note that the intensity of the ring is illustrated in two dimensions, so it is not confused with the binary.

2.9.5 Ring

We also note the intensity and visibility of a ring of infinitely small width and with diameter θ . Although this is not a very useful or realistic model on its own, it can be used to describe more complex models like a ring of finite width or an accretion disk, which is demonstrated below. The intensity is given by:

$$I_{\text{ring}}(r) = \frac{1}{\pi\theta} \delta\left(r - \frac{\theta}{2}\right), \quad (2.49)$$

and the visibility is simply:

$$V_{\text{ring}}(r_{u,v}) = |J_0(\pi\theta r_{u,v})|, \quad (2.50)$$

where J_0 denotes the Bessel function of the first kind and order zero. The intensities and visibilities of a binary and a ring are illustrated in Figure 2.10.

2.9.6 Combinations of models: disks with an inner hole and accretion disks

Due to the linearity of the Fourier transform, the visibility of an arbitrary combination of the aforementioned models is simply the sum of the individual visibilities weighted by their fluxes and normalised by the total flux. So assuming n models we obtain the total

visibility according to:

$$V_{\text{total}}(u, v) = \frac{\sum_{i=1}^n F_i V_i(u_i, v_i)}{\sum_{i=1}^n F_i}. \quad (2.51)$$

A disk with an inner hole can now be modelled by summing over a finite number of annuli ranging from an inner diameter θ_i to an outer diameter θ_o , where the visibility of each annulus is weighted by its flux. This can either be done assuming a constant flux per unit area, which in the case of $\theta_i \ll \theta_o$ yields a result comparable to the uniform disk, or we can specify a temperature profile and calculate the flux of each ring as if it were a black body, yielding a simple model for an accretion disk.

2.10 Observing in the infrared

Today, astronomers observe the universe using virtually every part of the electromagnetic spectrum. Due to the huge diversity of physical processes involved, every wavelength range is connected to certain objects which emit radiation primarily in this range. The *visible* light around 500 nm, for example, is connected to the “hot” parts of the universe, that is, to stars with (surface) temperatures of thousands of Kelvin or the illuminated material in their immediate surroundings. X-ray observations reveal even hotter material (or different processes) in active galactic nuclei, binary stars, supernova remnants, galaxy clusters and also the corona of our sun. Infrared radiation, on the other hand, provides a wealth of information about “warm” (a few hundred Kelvin) gas and dust in the universe, which is not accessible by any other wavelength regime. Here, small particles of a few micron in size such as silicates, silicon carbide, carbon, coals, aluminium oxides or polycyclic aromatic hydrocarbon (PAH) molecules contribute to the mid-infrared radiation, while gases like neon and molecular hydrogen emit through a large number of ionic and atomic lines ([Ne II] at 12.81 μm , rotational transitions of H_2 at 8.02, 9.66, 12.27 and 17.03 μm). In combination with the fact that extinction due to interstellar dust is much weaker for infrared light than it is for visible light, infrared observations are the perfect tool to investigate young stars and their surroundings, the centre of our own galaxy or, due to the cosmological redshift, galaxies in the early Universe.

Longer wavelengths also have a favourable effect considering the atmospheric turbulence, so that diffraction limited images with 8 m telescopes are feasible. However, infrared observations suffer from the same problem as many other wavelength ranges, namely the partial or even complete absorption of the radiation by the atmosphere. In addition to this, the atmosphere and the telescopes strongly emit in the infrared themselves, often outshining the astronomical objects. Ignoring space-based telescopes, this forces astronomers to restrict their observations to the few existing transparent “windows” and to the use of dedicated observing techniques (see Section 2.10.3). The infrared is usually divided into three parts: the near-infrared (0.8–4 μm), the mid-infrared (4–40 μm)

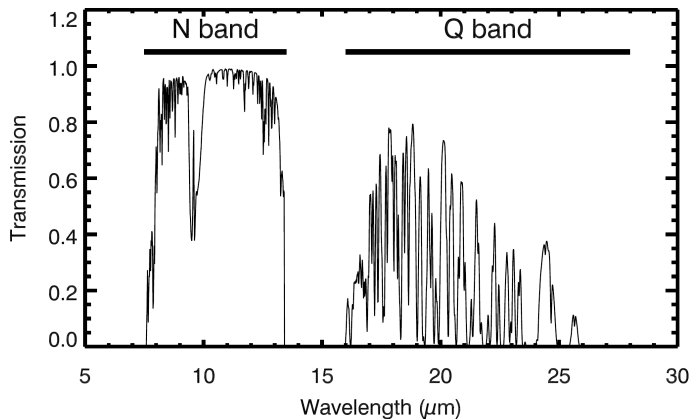


Figure 2.11: The mid-infrared transmittance of the sky above Cerro Paranal from 5 to 30 μm . Result of a simulation for an altitude of 2600 m and 1.5 mm of precipitable water vapour at zenith. (taken from the user manual of VISIR, accessible at: <http://www.eso.org/sci/facilities/paranal/instruments/visir/doc/index.html>).

and the far-infrared (40–300 μm), yet none of these boundaries should be considered exact. Since MIDI works in the range from 7.5 μm to 13.5 μm , all of the following will only address the mid-infrared, although some aspects might also apply to the near- or far-infrared.

2.10.1 Transmittance of the atmosphere

The first problem which is caused by the atmosphere is the absorption of most of the mid-infrared radiation coming from astronomical sources. Figure 2.11 shows an example of the transmittance of the sky from 5 μm to 30 μm . The two bands in which observations from the ground are possible are called the N and the Q band and range roughly from 7.5 μm to 13.5 μm and 16 μm to 25 μm , respectively. Even in these windows, the atmosphere is not perfectly transparent (especially not in the Q band), but today's detector technology and the usually very dry air at the high altitude of the observing sites still allow for good data quality. The most important absorber of mid-infrared radiation is water vapour. Other important molecules include CH_4 , CO_2 , CO , O_2 and O_3 . The deep absorption feature which can be seen around 9.6 μm in the N band is caused by the ozone layer.

2.10.2 Background emission

The second problem caused by the atmosphere arises from its strong thermal emission which can be described by a black body spectrum with a temperature of about 250 K. Using Wien's displacement law, we immediately see that the peak of the emission lies at approximately 11.6 μm , thus exactly inside the N band. Observing in the mid-infrared can therefore be compared to observing in the optical during daytime, even though the sky's brightness during the day is caused by scattered light from the sun and not due to emission of the atmosphere itself. The effect for an observer is the same: everything glows brightly and the astrophysical sources are hidden in an overwhelming background. A typical value for the brightness of the night sky at 10 μm is -5 mag per square arcsecond, which is

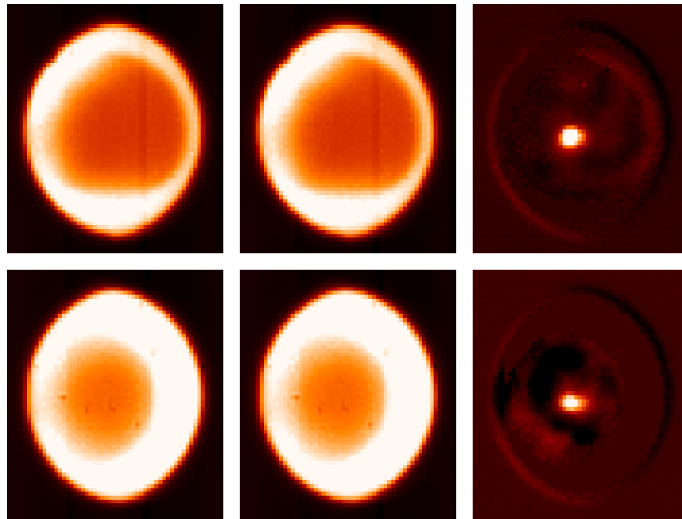


Figure 2.12: MIDI images of IRS 9A obtained on the 27 February, 2005. Top row: images from UT2, bottom row: UT3. In each row the image on the left shows the “on-source” position, the one in the middle the “off-source” position and the one on the right the result of their subtraction. The bright rings on the outside are caused by thermal emission from the VLTI tunnel, the sky can be seen as the darker area in the middle (FOV $\approx 2''$). The target is only visible after subtraction of the background.

roughly similar to the brightest objects in the infrared. The majority of the sources are much fainter though, and brightness ratios of a hundred or a thousand to one are quite common.

There is another source of unwanted background radiation which is caused by the telescope mirrors and the mirrors of the VLTI infrastructure. Since they have a temperature of about 280 K, they also radiate predominantly in the mid-infrared. In total there are 27 mirrors in front of the cryostat of MIDI and their radiation produces an even stronger background than the one from the atmosphere. The flux inside the Airy disk which originates from the sky background amounts to about 10^{10} photons/s, whereas the flux from the VLTI optical train is around 10^{11} photons/s (Leinert et al. 2003b,c). Due to these huge numbers, the exposure time has to be kept very short in order not to saturate the detector. Typical values range from few milliseconds to few tens of milliseconds for the detector integration time (DIT). This is the reason why the sensitivity of ground-based infrared instruments is rather low. The values for MIDI are given in Table 3.1.

2.10.3 Chopping and nodding

The standard procedures used to get rid of the high background radiation in the infrared are called chopping and nodding. The idea behind both is to alternately observe the region of the sky containing the target and an “empty” region of the sky. The background is then removed by subtracting the two datasets from each other, leaving the target (and small residuals) behind. Since the background depends on the position in the sky and also varies quickly in time, the empty region should be as close as possible to the target and the switching between the two regions has to be fast (typically 0.5 Hz for MIDI). Chopping at the VLT is implemented by tilting the secondary mirror of the telescopes, which can yield a chopping throw of up to 30 arcseconds. Figure 2.12 shows some images of IRS 9A

obtained with MIDI to illustrate the chopping technique. The source is not bright enough to be visible in the unprocessed images, and due to the huge background the two images on the left of each row seem to be identical, while, in fact, they are not (see the caption for additional information).

This procedure removes most of the background and also the temporal variations in it. Due to the fact that the light paths are not exactly the same when the secondary mirror is moved, an intensity gradient remains in the background subtracted image. This residual can be removed with the nodding technique, where the whole telescope points to the empty region and the chopping observations are repeated. However, nodding is not applied when observing with MIDI and during the interferometric exposures the background can even be removed without chopping (see Section 3.1). Subtracting an image of the sky from an image of the target (with sky) has the additional advantage that it removes detector artifacts.

2.11 The VLT Interferometer

The VLT Interferometer (VLTI) is located on the summit of Cerro Paranal, a 2635 m high mountain in the Atacama desert in the north of Chile. It is operated by the European Southern Observatory and consists of four 8.2 m telescopes, the so-called Unit Telescopes (UTs), and, since December 2006, also of four 1.8 m telescopes, the so-called Auxiliary Telescopes (ATs). These smaller telescopes lack much of the light collecting capabilities when compared to the UTs, of course, but have the advantage that they can be moved on a system of rails. This allows for a more flexible configuration of the interferometer, provided that the target is sufficiently bright. The light of two or three of these eight telescopes can currently be combined by MIDI and AMBER, the first generation of interferometric instruments. The second generation of instruments will use 4 or even up to 6 telescopes, which will significantly improve the coverage of the u - v -plane within a single measurement and hence allow imaging. Construction work on the mountain began in the early nineties and “first light” with the first of the four UTs was achieved in May 1998. The first fringes, that is, the first light of the VLTI, were obtained nearly three years afterwards in March 2001. A view of the observing platform of the VLT in the year 2005 is shown in Figure 2.13.

2.11.1 Baselines

The range of baselines between the UTs spans from 47 m, the baseline between UT2 and UT3, to 130 m between UT1 and UT4. The possible positions of the ATs are arranged on a grid with a cell size of 8 m. Therefore the baselines range from 8 m between two stations which are directly adjacent to each other, up to 202 m, which is the maximum baseline length of the VLTI. As illustrated in Section 2.3, the given baseline lengths have to be projected onto the plane which is perpendicular to the line of sight to the object in order



Figure 2.13: The VLT on Cerro Paranal. The picture shows the four UTs, two of the ATs, the interferometric laboratory (the flat building), the AT rail tracks and, in the background, the enclosure for the new survey telescope VST. The picture is taken from the ESO press release 06/05 (14th March, 2005) and has been slightly cropped to better fit the page. (<http://www.eso.org/public/outreach/press-rel/pr-2005/pr-06-05.html>)

to calculate the actual resolution of the interferometer. A schematic diagram of the VLTI is shown in Figure 2.14, indicating the outline of the mountain top of Cerro Paranal with the positions of the UTs, the grid for the ATs, the delay line tunnel and the interferometric laboratory.

Due to ongoing construction work, not all of the AT baselines are offered for observing and the maximum baseline with the ATs is 128 m long (as of the current observing period from 1 April, 2009 until 30 September, 2009). Additional observational constraints exist for some of the possible VLTI configurations which are either due to telescope shadowing or the limited length of the delay lines. For example an AT on a position close to a UT will have serious sky restrictions (compare with Figure 2.13) and when using the UT1–UT4 baseline, the delay line is not long enough to compensate for the OPD of an object which is close to the southwestern horizon. Due to the atmospheric extinction, it is highly advisable not to observe objects close to the horizon, and so the aforementioned issues do not usually have any significant consequences for the observations.

2.11.2 Delay lines

The delay lines correct the different lengths of the optical path in the arms of the interferometer whenever the observed object is not at zenith (see Section 2.3). This difference has to be continuously adjusted due to the rotation of the earth. Accomplishing these two goals for an interferometer working in the optical is not a simple task. Interference will only occur if the optical path difference is cancelled to within a (small) fraction of the wavelength, whereas the mirrors of the delay line have to move with speeds of the order of cm/s to correct for the apparent sidereal motion. Considering that AMBER and MIDI work in the wavelength ranges around 1 μm and 10 μm , respectively, and that the length of the delay lines is 60 m, this is a dynamic range in the region of 10^9 . According to Glindemann et al. (2001) the (repeatable) absolute position accuracy over the full length of the delay lines is approximately 30 μm and the relative position error is about 20 nm. Figure 2.15 shows the tunnel of the delay lines with one of the carriages which house the

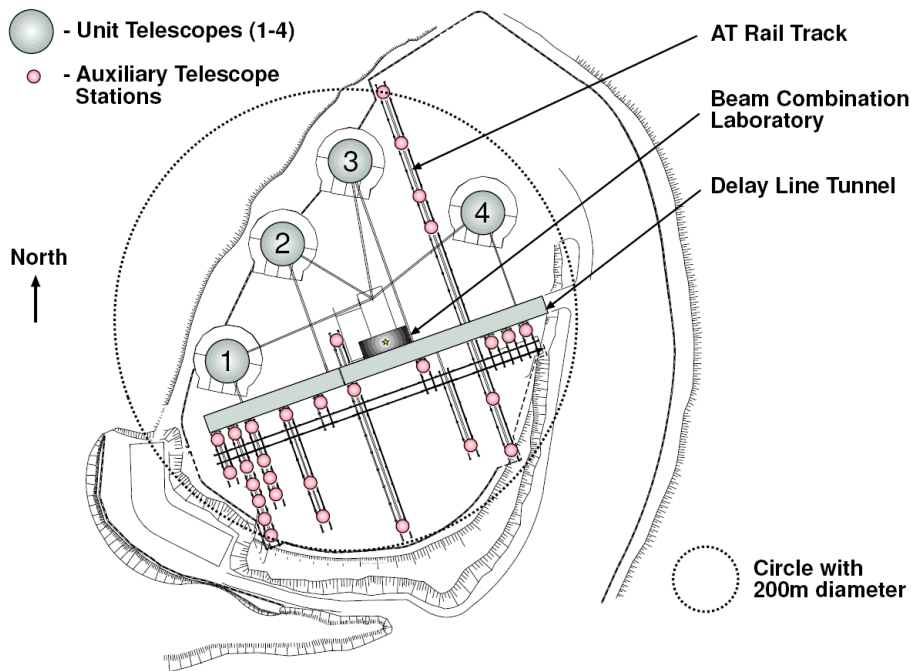


Figure 2.14: A schematic diagram of the VLTI with its main components labelled. See text for additional information. Figure taken from Glindemann et al. (2003).

cat's eye reflector system.

Since every reflection on one of the 27 mirrors belonging to the telescopes and the VLTI infrastructure leads to the loss of light, only 30–35 % of the total incident radiation reaches the instruments. This is another reason why the sensitivity with MIDI is rather low, but the main problem is still the short integration time which is imposed by the atmospheric turbulence.

2.11.3 MACAO and FINITO

Every Unit Telescope is equipped with an adaptive optics system called MACAO (Multi Application Curvature Adaptive Optics). Its purpose is to correct the wavefront distortions which are caused by the atmosphere in order to improve the overlap of the beams when they are combined in the interferometric laboratory. All the technical details can be found in an article by Arsenault et al. (2003) and also in an ESO press release³.

All four MACAO units are identical and are installed in the so-called Coudé room under each telescope. The AO system consists of a deformable mirror with 60 elements which is coupled to a curvature wavefront sensor. The system corrects the shape of the wavefront at a rate of 350 Hz in real-time and offers the recording of nearly diffraction limited images in the near- and mid-infrared. While MIDI does take real images of the

³<http://www.eso.org/public/outreach/press-rel/pr-2003/pr-11-03.html>

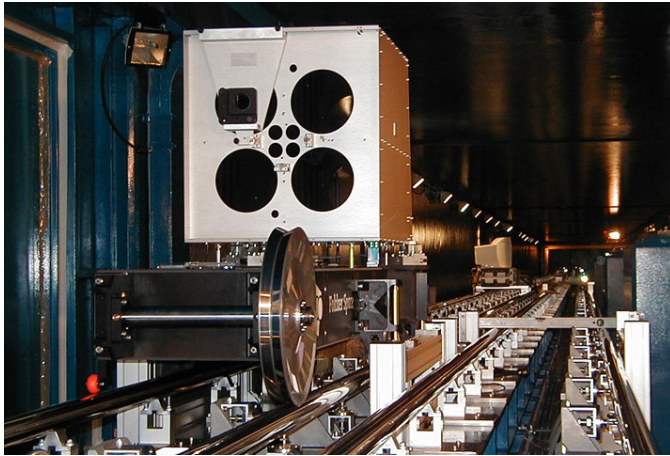


Figure 2.15: A carriage of the delay line system on its rails. The light enters the reflector through one of the big holes and emerges on the opposite side. The image is taken from the ESO press photos 26a-e/00 (11 October, 2000) and has been slightly cropped to fit the page. (<http://www.eso.org/public/outreach/press-rel/pr-2000/phot-26-00.html>)

target, the main goal is, of course, to measure the amount of coherence of the two light beams. In this respect the effect of MACAO is to increase the sensitivity by optimising the overlap of the beams, which allows the observation of fainter targets and increases the overall efficiency.

While the MACAO instruments correct the shape of the wavefronts at each individual telescope, the aim of FINITO (Fringe-tracking Instrument of NICE and TORINO) is to measure the phase difference between the arms of the interferometer. FINITO works in the H band around $1.65 \mu\text{m}$ and can be used with both MIDI and AMBER (two or three telescopes), but the benefits when used with MIDI are limited. Since FINITO was not available during the time of our observations (it was offered for the first time in 2007) we will not discuss further details and instead refer to the reference publication by Gai et al. (2004) and the additional information which can be found in the user manual of MIDI and on an ESO web page⁴.

⁴<http://www.eso.org/sci/facilities/paranal/telescopes/vlti/subsystems/finito/index.html>

3 MIDI

The **mid**-infrared interferometric instrument (MIDI) is one of the two first generation interferometric instruments of the VLTI (Leinert et al. 2003b). MIDI combines the light from two telescopes and covers the full N band from 7.5 – 13.5 μm . It was built by an international consortium of 12 institutes from Germany, the Netherlands and France under the leadership of the Max Planck Institute for Astronomy in Heidelberg. The conceptual design started in Heidelberg in 1997. First fringes in the lab were obtained during October 2001 and the instrument was sent to Chile about a year later in September 2002. It was re-assembled on Paranal in November and the first “real” fringes on a scientific target were obtained soon afterwards in December 2002. It has been made available to the worldwide community of astronomers since September 2003.

3.1 Optical layout

The design of the instrument is presented in detail in Leinert et al. (2003a,b,c), in the PhD thesis of Thorsten Ratzka (Ratzka 2005) and in the MIDI User Manual¹, the latter being continuously updated by ESO and therefore providing the most up-to-date information. The basic parameters of MIDI are summarised in Table 3.1. MIDI is a coaxial beam combiner (pupil-plane, see Section 2.5) and the instrument can be divided into two main parts: the warm optics on the MIDI table and the cold optics in the cryostat (“cold box”). As already mentioned in Section 2.10, radiation at 10 μm is dominated by the thermal emission from the environment, so most of the optical elements are located in the cryostat. The temperatures range from 77 K for the outer radiation shield to 40 ± 5 K for the cold bench and 9 ± 3 K for the detector. For a more detailed description of the cold optics of MIDI see Glazeborg-Kluttig et al. (2003).

After being collected by the telescopes and transferred to the instrument by the VLTI infrastructure, light reaches the instrument from the left in Figure 3.1. The two beam compressors still belong to the VLTI infrastructure and simply reduce the width of the two beams. The small delay lines directly in front of the cryostat are used to step the OPD rapidly around the point of zero-OPD to scan the fringes (compare with Sections 2.5 and 3.3). Following the subsequent path of the light in Figure 3.1, the two beams enter the cryostat through the dewar window and pass a cold pupil stop which suppresses thermal emission which does not belong to the beams. The beams are then focused in order to be

¹<http://www.eso.org/sci/facilities/paranal/instruments/midi/doc/index.html>

Wavelength coverage:	7.5 – 13.5 μm (N band)
Spatial resolution:	20 milliarcseconds (λ/B for 100 m baseline)
Spectral resolution:	30 or 230 (prism or grism)
Field of view:	2 arcseconds (UTs), 10 arcseconds (ATs)
Limiting N-magnitude without external fringe tracking:	3 – 4 mag (1 – 2.5 Jy, UTs), 0 – 1 mag (ATs)
Accuracy of visibility:	$\pm 5\%$ (Sci-Phot) $\pm 20\%$ (High-Sens)

Table 3.1: Basic parameters of MIDI. Data taken from Leinert et al. (2003b,c). At the time of our observations MIDI was operated without external fringe tracking.

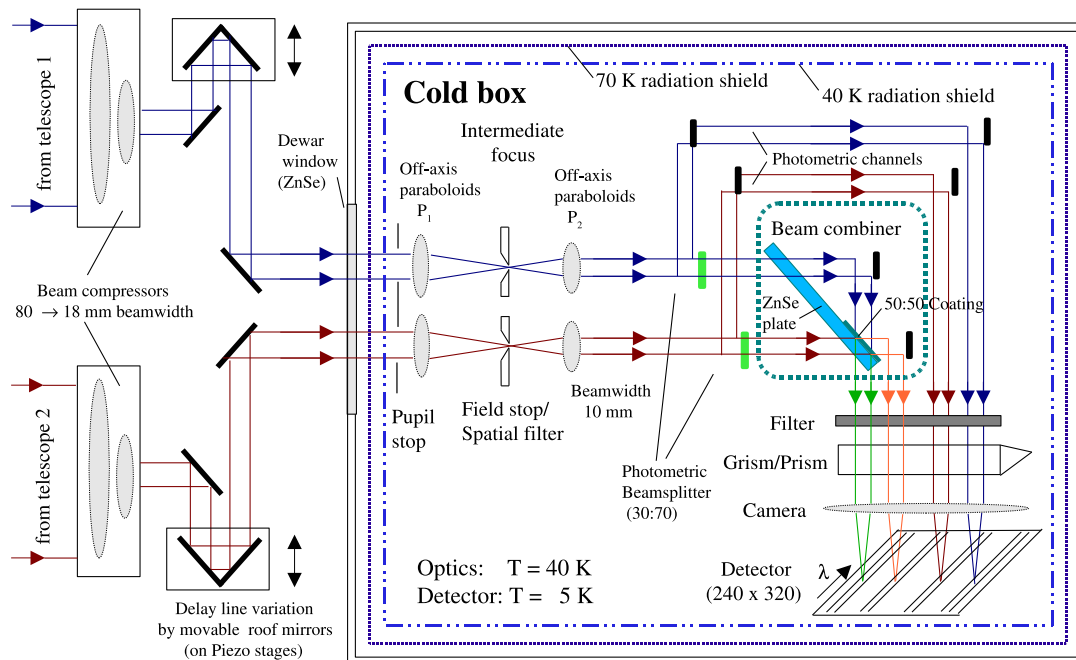


Figure 3.1: Schematic diagram of MIDI's optics. Some of the lenses are in fact mirrors, but for simplicity drawn as lenses. Image courtesy of U. Graser, MPIA.

able to insert different slits or spatial filters if further suppression of radiation is desired. After that they are re-collimated and two beam splitters can be placed in the light path to extract photometric information while scanning the interferometric signal. This setup is called “Sci-Phot” and has the advantage that the total flux of the source (needed for the determination of the visibility) is measured together with the fringe signal, which improves the accuracy of the visibility. The disadvantage is that, since around 30 % of the flux is extracted, the target has to be brighter to be observable. In the other setup option, called “High-Sens”, no flux is extracted during the fringe measurement and there

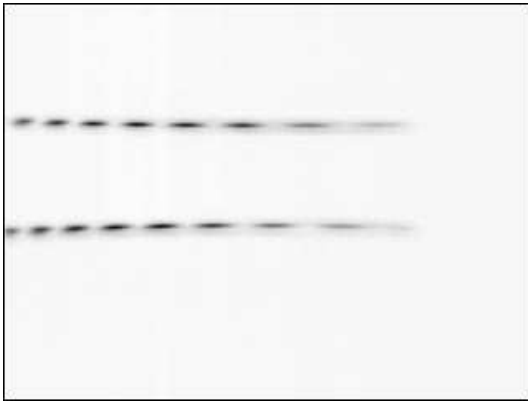


Figure 3.2: Sample image of the two dispersed interferometric beams of MIDI obtained in the laboratory. The wavelength increases from the left to the right and the phase opposition between the fringes is easily visible. Image taken from the user manual of MIDI, accessible at: <http://www.eso.org/sci/facilities/paranal/instruments/midi/doc/index.html>

is a photometric measurement for each of the two telescope beams directly afterwards instead. The disadvantage here is that the large thermal background usually changes between these measurements, degrading the accuracy of the visibility.

The beams then approach the heart of the instrument, namely the beam combiner. The combining element itself is a half-transparent plate on the back side of the ZnSe plate in Figure 3.1. Here 50 % of the light from telescope 1 is transmitted and 50 % of the light from telescope 2 is reflected, forming the first combined beam. The rest of the light, consisting of the reflected 50 % from telescope 1 and the transmitted 50 % of telescope 2, forms the second combined beam which is directed towards the detector with an extra mirror (compare with the right part of Figure 2.6 on page 22). As already addressed there, the two combined beams are in phase opposition due to the phase shift introduced by the beam splitter. If the light in one of the interferometric channels interferes constructively, the other channel will show destructive interference and vice versa. This fact can be exploited in an easy and elegant way in order to dispose of the background radiation. Since the thermal background between the two interferometric beams is almost totally correlated, simply subtracting one beam from the other will add the interferometric fringes and remove the background. Therefore, in interferometric setup, the chopping technique is not required. Figure 3.2 shows an image of the (spectrally dispersed) interferometric beams, where the phase opposition and the fringes are easily visible.

3.2 Detector

The detector of MIDI is a SiAs impurity band conduction array, also known as blocked impurity band. It was manufactured by Raytheon and is 320×240 pixels in size. More characteristics of the detector can be found in Table 3.2.

The detector is operated in the so-called “Integrate-Then-Read” (ITR) mode. In this mode, before the start of the integration, the whole detector is reset and at the end of the exposure a bias voltage stops any further accumulation of electrons. Due to the high thermal background, the exposure times have to be kept very short in order not to saturate

Array dimensions	320 × 240 pixels
Pixel size	50 μm × 50 μm
Peak quantum efficiency	34 %
Dark current	10 ⁴ electrons / pixel / second at 10 K
Operating temperature	4 – 12 K
Well capacity	1.1 × 10 ⁷ electrons
Readout noise	≈ 800 electrons

Table 3.2: Basic characteristics of MIDI’s detector, taken from the user manual.

the detector. To this end the signal is always spectrally dispersed by either the prism or the grism, which distribute the light over a wider area of the detector.

The time needed for a readout of the whole chip is about 6 ms and the minimum integration time is 0.2 ms. The integration times for the different instrumental setups lie in the range from a few milliseconds to a few tens of milliseconds. Since this leads to quite high data rates (up to some tens of Mbytes/s), it is possible to select only certain areas of the detector to be read out. This procedure is called “windowing” and is applied in all operating modes where a full read out of the chip is not necessary. Although this also reduces the time needed for the readout (around 3 ms for most of MIDI’s operating modes), the data rate is still much lower than without windowing due to the much smaller “images”.

3.3 Observing procedure

The typical observing procedure for MIDI is described in Leinert et al. (2004) and Chesneau et al. (2005). More detailed accounts can be found in Chesneau (2007), Ratzka (2005) and the user manual of MIDI. In the following, the observing procedure which was used during the time of our observations (in the year 2005) is described. For changes which took place afterwards we refer to the homepage of MIDI².

The typical observing procedure consists of two or three main steps, depending on the setup of the instrument. The first step is always the acquisition of the target in imaging mode. In case of the “Sci-Phot” setup this is followed by the simultaneous measurement of the fringe signal and the photometry of the source. When using the “High-Sens” setup, the acquisition is followed by the fringe measurement and the photometry is measured separately in the third step. The whole procedure is used for both the science target and a suitable calibrator star with known diameter, in order to correct for the atmospheric and instrumental losses. The calibrator is usually observed directly before or after the science target in order to minimise the effects of the ever-changing atmosphere. The total

²<http://www.eso.org/sci/facilities/paranal/instruments/midi/>

time needed to obtain one calibrated visibility in this way amounts to 30 to 60 minutes, depending on the weather conditions and the brightness of the targets.

The observing procedure starts with the pointing of the telescopes towards the target. Here, MIDI is used in imaging mode without beam combiner and dispersing element, and the two telescope beams form two images of the observed region of the sky on the detector. The user has the possibility to specify a filter for the acquisition, but the N 8.7 filter is usually recommended due to a good signal-to-noise ratio (SNR). Appendix B shows the transmission curves for the N band, the N 8.7 and the N 11.3 filter.

Since it is very important for the interferometric measurements that the beam overlap is as good as possible, the pointing has to be very accurate. If the target is inside MIDI's FOV of approximately $2'' \times 2''$, the acquisition images are used to adjust the pointing of each telescope so that the images of the target move to predetermined pixels on the detector (this procedure is now obsolete and the IRIS instrument is used to control the correct alignment of the two beams instead, reducing the time required for the observations). The default value for the DIT is 4 ms, and, depending on the brightness of the target, at least 1000 frames are recorded to increase the SNR. In order to speed up the process and to reduce the amount of data to be stored, only the two small areas (each 62×69 pixels in size) where the beams actually illuminate the detector are read out.

The acquisition images are not only useful for the alignment of the telescopes, but also provide low resolution (compared to the interferometer) information about the object which can be helpful for the interpretation of the interferometric data, but are also interesting in their own right. Although MIDI was not designed to be an imaging instrument, thanks to MACAO the acquisition images are diffraction limited and therefore have a resolution of about 0.3 arcseconds (for the UTs). No other telescope at the VLT is currently able to do this in the mid-infrared (VISIR does not have an AO system). Using the observations of the calibrator star as a PSF reference, the resolution of the images can be even further improved by deconvolution algorithms (see Section 4.2).

After the acquisition of the source, the beam combiner and the prism or grism are inserted into the optical train for the interferometric measurement. In order to find the location of zero optical path difference, the VLTI delay lines scan a region of a few millimetres in length around the expected point of equal path lengths. When the correct position is found, the piezo-mounted mirrors of MIDI's internal delay line are used to scan a range of six to eight wavelengths ($\approx 60 - 80 \mu\text{m}$) around the point of zero-OPD in steps of typically $2 \mu\text{m}$. An exposure is taken at each of these steps, giving the dispersed interferometric signal for the corresponding OPD. The delay lines of the VLTI re-centre the fringe packet between each scan, correcting for the sidereal motion and the atmospheric turbulence. Figure 3.3 illustrates the process of finding and recording the fringes. It is repeated until a few hundred scans have been obtained, and from the average of these scans the fringe amplitude can be determined. As already noted in Section 3.1, chopping is not needed to cancel the background during the interferometric observations.

If MIDI is in the Sci-Phot setup, the photometric information was obtained during the fringe scans, and the observing procedure stops here. In the High-Sens mode, the

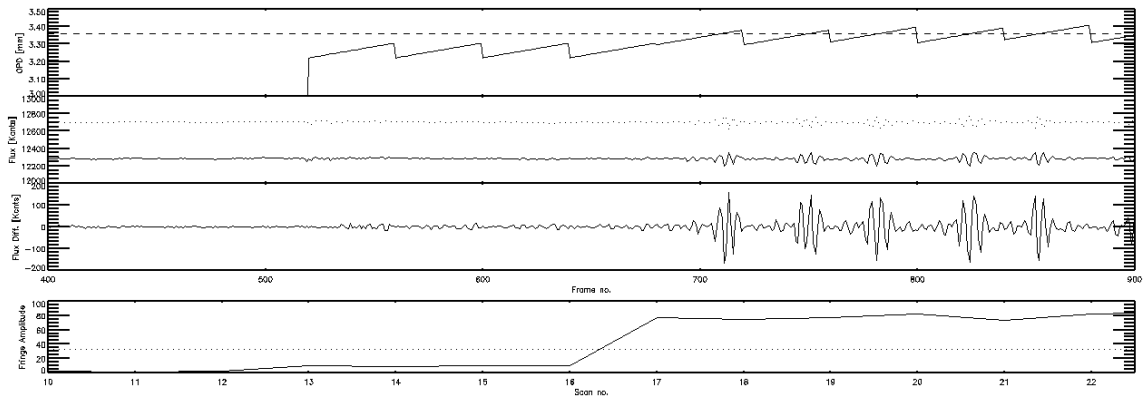


Figure 3.3: The figure shows the search for the point of zero-OPD and the start of a fringe scan for our calibrator star HD 107446. The top row displays the optical path difference in mm (from 3.0 mm to 3.5 mm) as a function of the frame number (from 400 to 900, i.e., spanning roughly 5 s). The last offset of the VLTI delay lines can be seen, where the start of the typical saw-tooth pattern indicates that the point of zero-OPD has been found. The second row shows the total flux for each telescope (with background), ranging from 12000 to 13000 counts, and the third row displays the difference of these two fluxes, ranging from -200 to $+200$ counts. The last row shows the corresponding fringe amplitude as a function of the scan number (from 10 to 22).

photometric data of the object have to be recorded in the third step. This is done by successively closing one of the two shutters of MIDI and recording the photometric information of each telescope separately. The beam splitter is not removed, and the flux is measured with the same pixels as during the fringe measurement, using the chopping technique to remove the background. The problem in this mode is that the atmosphere alters the result of the photometric measurement between the second and the third step at a level of up to 15–20% or even more (Chesneau et al. 2005; Chesneau 2007). This can be easily seen in Figure 4.3 in Section 4.3.1, where we show the calibrated spectra of IRS 9A. The true level is not determined and since the visibility is calculated by dividing the correlated flux by the total flux, the visibility has a similar uncertainty. This is the major source of error in the High-Sens mode.

4 Observations and data reduction I – MIDI

In this chapter, we first give a brief description of the software which we used for the data reduction in Section 4.1 and then present all the data which we obtained with MIDI at the VLTI in Sections 4.2 to 4.4. Additional data from other telescopes and instruments are presented in Chapter 5.

IRS 9A was observed with MIDI during three nights in February and March 2005, and a total number of 7 visibility measurements were obtained. The first two observations were carried out during the nights from the 26th to the 27th and the 27th to the 28th of February, using telescopes UT2 and UT3. These telescopes are separated by an on-ground baseline of 46.6 m which has an orientation of 40° (east of north). The third observation during the night from the 2nd to the 3rd of March used telescopes UT3 and UT4 with an on-ground baseline of 62.4 m and an orientation of 111° . A complete log of the observations can be found in appendix A.

In order to correct the measurements for instrumental and atmospheric effects, every observation of the science target is immediately followed by an observation of an appropriate calibrator star with the same instrumental setup. This calibrator should be sufficiently close to the science object, bright enough in the N band to be easily observable with MIDI and also have a diameter of not more than a few milliarcseconds, that is, it should appear as a point source to MIDI. Suitable calibrator stars can be found using the CalVin database which is maintained by ESO.¹

We chose HD 107446 as our calibrator star and observations were taken before and after every observation of IRS 9A. According to the SIMBAD and CalVin databases, HD 107446 is an optically rather bright K3.5III star with a B and V magnitude of 5 and 3.6, respectively. Its magnitude in the N band is 0.22 and its flux at $12\ \mu\text{m}$ is $32.42\ \text{Jy}$ (measured by IRAS, the Infrared Astronomical Satellite). The uniform disk diameter is $4.43 \pm 0.02\ \text{mas}$ and its angular distance from IRS 9A is 8.1° .

4.1 The MIA+EWS data reduction package

Unless stated otherwise, we used the standard MIA+EWS (version 1.5) data reduction software² for our data. This software package actually contains two data reduction pro-

¹<http://www.eso.org/observing/etc/>

²<http://www.strw.leidenuniv.nl/~koehler/MIA+EWS-Manual/index.html>

cedures, which use different approaches to obtain the interferometric information from the raw data. MIA (MIDI Interactive Analysis) is based on power spectrum analysis and was developed by the MIDI group at the MPIA in Heidelberg. EWS (Expert Work Station) is based on coherent integration and was developed by Walter Jaffe at the Leiden Observatory. The complete package can be downloaded here³ and more details about the reduction procedure can also be found in Ratzka (2005).

We also used the publicly available code OYSTER for our data reduction and analysis. OYSTER provides a single environment for the general analysis and visualisation of interferometric data and the MIA+EWS data reduction package can be conveniently executed from within the software. Within OYSTER it is, for example, easy to evaluate the quality of the calibrator measurements in order to reject possible outliers. The latest version of the software can be obtained from its web page⁴. In the following two sections, the algorithms of MIA and EWS are briefly summarised.

4.1.1 MIA

The concept of data reduction with MIA is given in detail in Leinert et al. (2004), while additional information can be found on the quoted web pages and in Köhler (2005).

In a first, step MIA determines the position and width of the spectrum as a function of wavelength. This is accomplished by averaging the target and the sky frames and subtracting the average sky frame from the average target frame. The position of the spectrum is found by searching for a sufficiently high signal in the resulting “image”. The process is carried out for both photometric datasets and a mask is created from the average position of the two spectra. This mask is then used for the extraction of the signal from the interferometric data. Here, each frame is multiplied by the mask and reduced to a one-dimensional spectrum by integrating in the direction perpendicular to the spectral dispersion. The frames from the two output channels are then subtracted from each other (see Section 3.1). Since each of the one-dimensional frames corresponds to a specific value of the OPD (MIDI’s piezo-mounted mirrors scan the signal around zero-OPD, see Section 3.3), these data are collected in a two-dimensional array sorted by wavelength and OPD. Each column of the array is Fourier transformed from OPD to fringe frequency space and by default three pixels are added in order to improve the signal-to-noise ratio. The fringe amplitude (or correlated flux) for each wavelength can be obtained from the power spectrum at the associated fringe frequency. Dividing it by the photometric flux then results in the raw visibility of the object, also called the instrumental visibility. In order to obtain calibrated visibilities, the instrumental visibility of the science target is divided by the instrumental visibility of a suitable calibrator star.

The result of the Fourier Transform from OPD to fringe frequency space is, of course, complex, but MIA neglects the phase and only calculates the amplitude of the visibility,

³<http://www.strw.leidenuniv.nl/~nevec/MIDI/index.html>

⁴<http://www.eso.org/~chummel/oyster/oyster.html>

that is, uses the square of the Fourier Transform. All information about the phase arising from the structure of the source itself is lost due to the turbulent atmosphere (see Section 2.8).

According to Leinert et al. (2004) this method excels in the case of bright sources, while EWS should be more reliable for faint sources. MIA does not offer the possibility to calculate a calibrated spectrum. In order to verify and compare the spectra which are calculated by the EWS software, we used a small IDL routine that was kindly provided by Olivier Chesneau (priv. communication).

4.1.2 EWS

The concept of the EWS software is described in detail in Jaffe (2004), on the quoted web pages and in the document from Rainer Köhler⁵ which was mentioned in Section 2.5.

The first steps in EWS are very similar to the ones in MIA. That is, multiply the photometrical data with a mask, integrate to get a one-dimensional spectrum and subtract the average target frame from the average sky frame. The only exception is that EWS uses a predefined mask to extract the spectrum while MIA calculates the mask interactively for each dataset. However, the user may specify an alternative mask (e.g. the one calculated from MIA) in order to compare the results of both reduction schemes in case they should deviate from each other.

Most of the atmospheric and instrumental background is removed when subtracting the averaged frames from each other, but the signal is still lost in the remaining background. The EWS software applies a temporal high-pass filter and subtracts the filtered data from the original data in order to remove this remaining background. This step exploits the fact that MIDI's piezo-mounted mirrors modulate the interferometric signal much faster than changes in the background occur. The next step is the instrumental OPD demodulation, which is the crucial part of EWS as compared to MIA. Here, each spectrum is multiplied by e^{-ikD_i} , where D_i is the known instrumental delay. The complex result still contains the OPD variations which are due to the unknown atmospheric delay. For this reason the spectra are Fourier transformed from the frequency to the (spatial) delay domain and the atmospheric OPD fluctuations are evaluated via group delay estimation (Lawson 1995; ten Brummelaar 1997; Lawson et al. 1999; Meisner 2001). This estimate is then used to demodulate the atmospheric delay of the signal using the same technique as before, that is, multiplying by e^{-ikD_a} , with D_a being the atmospheric delay. The phase of the data is still not constant in time after this step because the index of refraction of air changes rather rapidly, which is not taken into account in the group delay estimation. The variations are caused by changing amounts of water vapour in the air and produce phase shifts of tens of degrees in a few seconds. In order to remove these phase shifts, EWS subtracts the mean phase (averaged over the N band) of each frame from the visibility at each spectral channel. Finally, the visibilities of the entire observation can be

⁵<http://www.strw.leidenuniv.nl/~koehler/MIA+EWS-Manual/Visibility.pdf>

averaged “coherently” and the result should, in theory, yield the same correlated flux as calculated within the power spectrum analysis in MIA. In practise the results cannot be identical for various reasons (starting with the different masks used in the first step), but they should agree within uncertainties of 10–15 %.

As mentioned in the previous section and Section 2.8, the phase of the visibility cannot be measured with MIDI. However, EWS is able to recover the relative phase of the signal between the different spectral channels (a remainder of the removal of the atmospheric delay). We will return to this so-called “differential phase” and how it can be used to investigate the observed object in Section 4.4.4.

4.2 Acquisition images

We used the acquisition images of IRS 9A and HD 107446 to create a deconvolved, high resolution image of IRS 9A. A log of these observations is given in Table A.2 in appendix A, which also contains some parameters of the atmosphere, the telescopes and comments for each observation. In order to perform the deconvolution, we need the instrumental PSF, which is obtained by averaging all the frames from the calibrator after the sky has been removed.

It should be noted that in our case this procedure was not straightforward, since we detected some apparent movements of the sources after they had been placed in the centre of the FOV. These movements are likely caused by MACAO and last only a few frames, but they significantly shift the signal of the source from the mean position. Simply averaging all the frames would therefore lead to a distorted PSF and an incorrect deconvolved image. We examined two possible ways to solve this problem. Our first attempt was to shift the non-centred frames back to the nominal position, while the second attempt was simply to exclude all these frames. In the end we chose the latter method, despite losing almost 50 percent of the frames. We rejected the method of re-centring the frames because most of the non-centred frames are also distorted themselves and hence would corrupt the PSF even when shifted to the right place. Careful inspection of the single frames for some of the observations has shown that the rejection algorithm we employed works well, and together with a rather conservative selection criterion we are now confident that the shape of the PSFs is correct.

The deconvolution itself was performed with the Lucy-Richardson algorithm from the IDL `astrolib` package, which was first introduced by Lucy (1974). The algorithm iteratively deconvolves an image with a given PSF based on the Maximum Likelihood solution and with additive noise. It is not easy to choose the right number of iterations and as an example we show in Figure 4.1 the results of the algorithm for the same image and PSF, but with a varying number of iterations. Beginning with small values, the results change up to a value of approximately 25 where a state of convergence is reached. From there up to 40 or 50, increasing the number of iterations does not change the result much, but after that the quality clearly decreases. We therefore chose to work with 25 iterations.

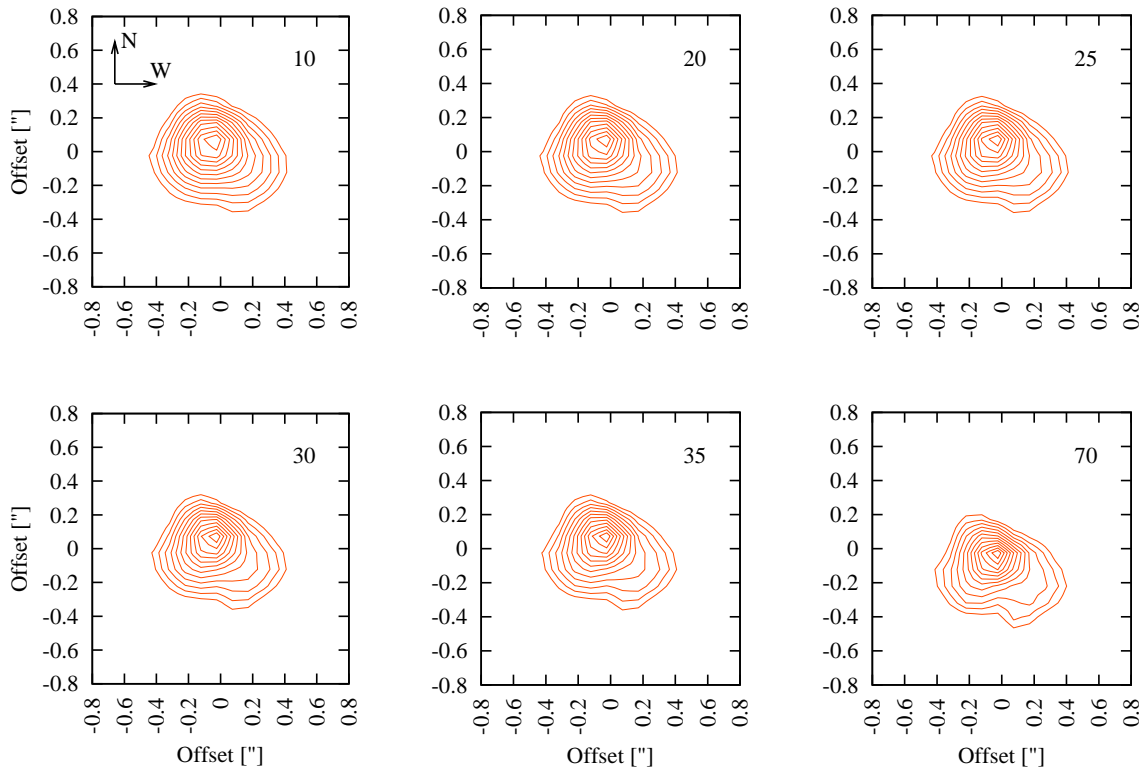


Figure 4.1: Deconvolved acquisition images of an observation of IRS 9A, each with a different number of iterations as indicated in the top right corner. North is up and East to the left. Convergence is reached around 25 iterations and the image quality starts to degrade for values which are too high. The 12 contour lines are equally spaced for the fourth root of the intensity, and the last contour is equal to 25% of the maximum of $I^{1/4}$. Given in percent of the maximum of I , the lines approximately lie at 0.4, 1, 2, 3.7, 6.3, 10, 15, 22, 32, 44, 59 and 77%.

4.2.1 Results

From our total number of seven observations of IRS 9A we obtained numerous acquisition images. Not only does every observation yield two images (one for each telescope), but one also has to choose an observation of the calibrator star which serves as the PSF reference. In general we used the observations both right before and after IRS 9A for this, which again doubles the number of deconvolved acquisition images. Therefore, we will only describe the overall conclusions which can be drawn from them and present some representative examples. Almost all of the images were obtained with the N 8.7 filter (see appendix B).

In the course of the deconvolution process we noticed that the quality of the “B” images, which originate from the telescope beam that enters the instrument through shutter B, seems to be systematically worse than the quality of the “A” images. The effect is not very strong and only visible for the last two or three contour lines, but it occurs during

Date (UT)	Telescope	FWHM x [mas]	FWHM y [mas]	Ratio
2005-02-27	UT2	402 ± 12	339 ± 2	0.844 ± 0.024
"	UT3	515 ± 14	337 ± 11	0.655 ± 0.022
2005-02-28	UT2	392 ± 64	366 ± 17	0.955 ± 0.150
"	UT3	536 ± 106	342 ± 26	0.653 ± 0.093
2005-03-03	UT3	375 ± 19	339 ± 14	0.905 ± 0.024
"	UT4	529 ± 94	411 ± 45	0.787 ± 0.074
Mean		459 ± 101	358 ± 35	0.81 ± 0.15

Table 4.1: Parameters of the deconvolved acquisition images sorted by date and telescope. The errors are the standard deviation of the 3 (02-27), 9 (02-28) and 6 (03-03) values, respectively. $x \rightarrow$ east-west direction, $y \rightarrow$ north-south direction.

every night of our observations. Since we changed the baseline from UT2–UT3 to UT3–UT4 for the last night, the effect most likely does not originate from the telescopes, but rather from the VLTI infrastructure or MIDI itself. A similar problem was also encountered during the calibration of the spectrum in Chesneau et al. (2005). Since the last three contour lines trace only very weak emission and are the ones which are most susceptible to reconstruction artefacts from the Lucy-Richardson algorithm, we did not investigate this any further.

Although the exact shapes of the deconvolved images vary from observation to observation, most of them show the slight asymmetries which are also visible in Figure 4.1. This demonstrates that the source is already partly resolved by an 8 meter telescope in the N band. The asymmetries are mainly oriented towards the south-west and south-east directions, which is further supported by the aperture masking observations from Gemini South (see Section 5.1). We applied a 2D Gaussian fit to the deconvolved images, providing information about the FWHM sizes in the x and y directions. The results of this statistical analysis are summarised in Table 4.1. The obtained values range from 337 mas to 536 mas, which lead to a rough estimate of the physical size of the emitting region of about 2400 AU to 3800 AU (assuming a distance of 7 kpc). Three examples of our deconvolved acquisition images are shown in Figure 4.2.

In comparison with the observations from Gemini South (see Section 5.1), we detected an interesting feature slightly north of IRS 9A. It is only traced by the last contour lines in some of the images, and without the aperture masking data we would most likely have neglected it. It can be seen at an offset of approximately 0.2 arcseconds to the west and 0.6 arcseconds to the north of the centre of IRS 9A. The position in the aperture masking image is slightly different, only about 0.5 arcseconds to the north, but this might be related to the fact that our image was taken at $8.7 \mu\text{m}$ while the Gemini data were taken at $11.7 \mu\text{m}$. It is also detected in more recent near-infrared observations with NACO at the VLT by Nürnberger (2008). These data were taken in J, H, K_s and L' filters and the source is easily visible in the L' data (see Figure 4 of Nürnberger 2008).

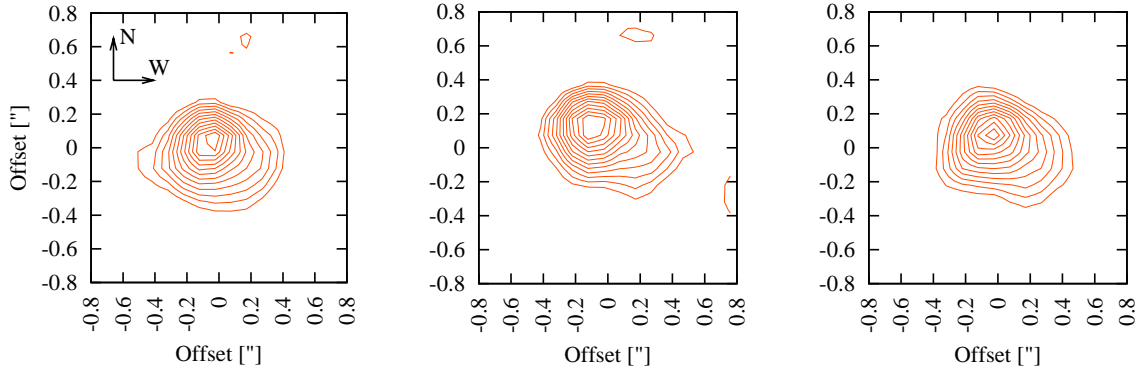


Figure 4.2: Three examples from our set of deconvolved acquisition images of IRS 9A. The image to the left shows the observation from the 27th of February (beam A), the one in the middle is the first observation from the 28th of February (beam B) and the one to the right displays the the first observation from the 3rd of March (beam B).

4.3 Photometric observations

Since the visibility is calculated as the ratio of the correlated flux to the total flux, MIDI also provides the user with a spectrum of the target. This photometric information is measured for each beam separately, and in our case took place directly after the fringe measurements. A log of these observations can be found in Table A.4 in appendix A. As already discussed at the end of Section 3.3, the photometry is heavily influenced by the atmosphere, and only EWS is equipped with routines to extract a calibrated spectrum from the data (see the web page mentioned in Section 4.1 for a description). In the following, the algorithm by Olivier Chesneau that we used in order to check the spectra produced by EWS is briefly described.

The raw photometry of each target is obtained with the standard procedure of subtracting the average sky frame from the average target frame, searching for a signal which is sufficiently high above the background, calculating a mask from this information and extracting the data with this mask. The raw spectrum of the science target is then divided by the raw spectrum of a calibrator observation in order to correct for most of the atmospheric absorption effects, most notably the deep absorption feature caused by the ozone layer. It is not possible to determine the absolute fluxes of the sources from our data, but we can use a measurement made by the Infrared Astronomical Satellite (IRAS) for this. We simply have to multiply the whole spectrum by the IRAS flux of the calibrator at $12\ \mu\text{m}$, which can be obtained from the SIMBAD Astronomical Database⁶.

The spectrum is now fully calibrated at $12\ \mu\text{m}$, but the values at the remaining wavelengths are not correct since our calibrator HD 107446 does not radiate like a perfect black body. We use an adequate template star from the catalogue by Cohen et al. (1999) in order to correct for this effect. The spectral type of this star should be as close as possible to

⁶<http://simbad.u-strasbg.fr/simbad/>

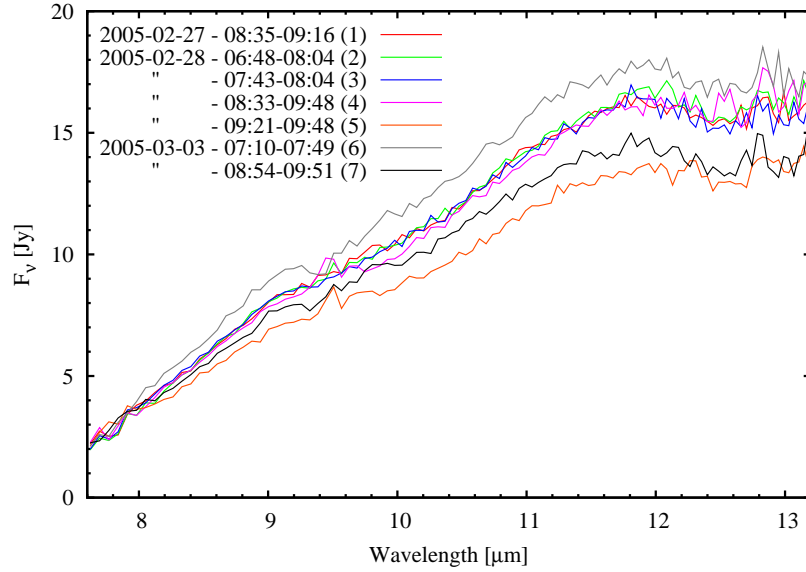


Figure 4.3: The spectra of the individual measurements of IRS 9A calibrated with EWS. The legend indicates the date of the observation, the time of the photometric measurement of IRS 9A, the time of the photometric measurement of HD 107446, which has been used to calibrate the spectrum of IRS 9A, and a sequential number.

the one of the calibrator, otherwise the continuum correction will not lead to good results. Its spectrum is normalised at $12 \mu\text{m}$ and multiplied with the one from the science target. The calibration of the spectra of IRS 9A with this method is summarised in the following equation:

$$S_{\text{IRS 9A, cal}} = \underbrace{\frac{S_{\text{IRS 9A, raw}}}{S_{\text{HD, raw}}}}_{\text{calibrated flux at } 12 \mu\text{m}} \cdot \underbrace{F_{\text{HD, IRAS } 12 \mu\text{m}} \cdot \frac{S_{\text{Cohen}}}{F_{\text{Cohen } 12 \mu\text{m}}}}_{\text{continuum correction}}, \quad (4.1)$$

where S indicates a full (N band) spectrum, F a single flux value and “HD” denotes our calibrator star HD 107446.

4.3.1 Results

Figure 4.3 shows the seven calibrated spectra we obtained from the data reduction with EWS. The flux of IRS 9A rises rather steeply towards longer wavelengths, with some flattening close to the long wavelength end of the N band. The former is the expected behaviour of a young stellar object (YSO) surrounded by large amounts of dust and gas. As already discussed in the last paragraph of Section 3.3, the absolute flux levels of the measurements differ quite a lot due to the changes in the atmospheric conditions, exhibiting differences as large as 20%. The shapes of the individual spectra are fairly similar though, and if scaled appropriately show only very small discrepancies. EWS calculates estimates for the errors of the photometry, but according to the manual they are not particularly reliable and therefore are not shown in the figure.

The legend specifies the observations of HD 107446 we chose in order to calibrate the spectra of IRS 9A. Ideally, the calibrator observations should be as close in time and

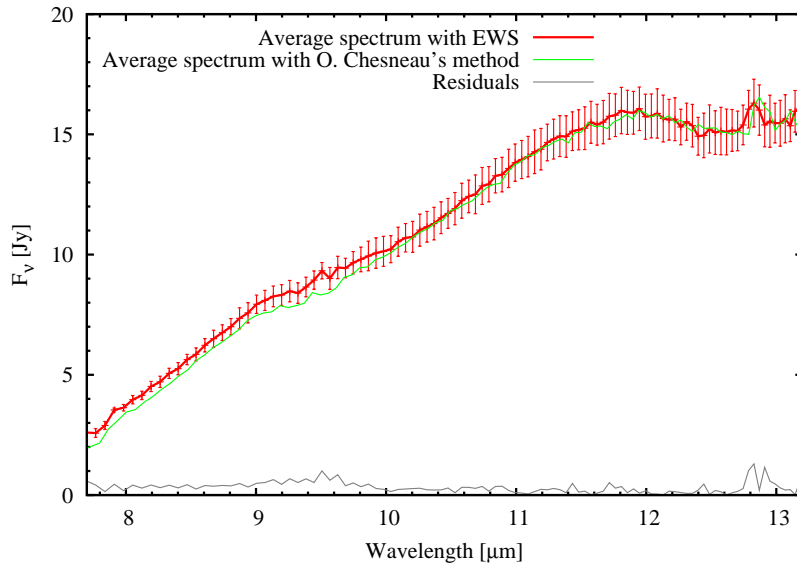


Figure 4.4: Comparison of the mean spectra of IRS 9A obtained with EWS and the method by Olivier Chesneau. The error bars for EWS are the standard deviation resulting from the seven measurements.

airmass⁷ as possible to those of IRS 9A, but choosing a different set of observations of HD 107446 in the calibration process did not have a strong effect on the results. The scatter between the individual measurements in Figure 4.3 always remained more or less at the same level. This gives a further indication that the unknown changes in the atmospheric conditions are the dominating source of error.

Due to the jagged shape of the individual spectra it is difficult to detect any obvious emission or absorption features. The small bumps around 9.5 μm are remnants of the strong absorption by ozone in the upper atmosphere and not intrinsic to the source (compare with the transmittance of the atmosphere in Figure 2.11 on page 33). It is difficult to achieve a good calibration here. However, a close inspection of the region around 12.8 μm reveals a weak emission feature present in all of the seven measurements. This is much more evident in Figure 4.4, where we show the mean spectrum resulting from the single EWS spectra, the mean spectrum obtained with the procedure from Olivier Chesneau and the modulus of their difference. Here, the emission feature can be clearly seen in both spectra, although the different calibration processes seem to have introduced a small wavelength shift. On the other hand, the prism only has a spectral resolution of about 30, and we cannot expect too much accuracy in any case. The wavelength of the feature matches the [Ne II] emission line at 12.81 μm , which is commonly associated with high-mass YSOs. Because of the high ionization potential of neon (21.56 eV, see, e.g., Cox 2000), Ne^+ can only exist in photo-ionised gas close to the young star. We will return to this point and discuss more spectral features of IRS 9A in Section 5.2, where we present the data from Spitzer.

The two independently calibrated spectra are in very good agreement with each other, demonstrating the reliability of both techniques. The residuals are almost always smaller

⁷See appendix A for a short description of the concept of airmass

Date	Time (UT)	#	Telescopes	B_p [m]	$\frac{\lambda}{B_p}$ [mas]	PA [°]
2005-02-27	08:35:10	1	UT2–UT3	31.83	51.8–84.2	80.41
2005-02-28	06:48:35	2	"	38.04	43.4–70.5	61.29
"	07:43:50	3	"	34.97	47.2–76.7	71.33
"	08:33:25	4	"	31.68	52.1–84.6	80.85
"	09:21:12	5	"	28.10	58.7–95.4	90.86
2005-03-03	07:10:49	6	UT3–UT4	62.46	26.4–42.9	132.32
"	08:54:33	7	"	61.95	26.6–43.3	155.87

Table 4.2: Log of the interferometric observations of IRS 9A. An estimate for the resolution of each observation is given in the second to last column for a wavelength of 8 μm and 13 μm , respectively. The position angle (PA) is measured east of north.

than 0.5 Jy, only reaching about 1 Jy in the region of the ozone absorption and of the emission line at 12.81 μm , where the small wavelength shift occurs. While 0.5 Jy corresponds to 10–20 % of the total flux at the short wavelength end, the same value leads to a relative error of only a few percent at the long wavelength end.

It is striking that the silicate feature at 9.7 μm , which is commonly observed in YSOs such as T-Tauri or Herbig Ae/Be stars, is seen neither in absorption nor in emission in any of our spectra. At the most we see hints for a very shallow and quite broad absorption feature in the range from 9–11 μm , but this could also be due to other effects. A missing silicate feature has been detected for other YSOs as well, and among the possible explanations which are discussed in the literature are the general absence of small silicate grains (Meeus et al. 2001, 2002, 2003), the absence of small and hot silicate grains (Dullemond et al. 2001), a very high ratio of the visual opacity to the opacity in the silicate feature (Natta et al. 2001) or a cancellation of silicate absorption and emission in disks which are seen edge-on (Chiang & Goldreich 1999). Whether one of these explanations or a combination of them can account for the spectrum of IRS 9A cannot be decided at this stage.

4.4 Interferometric observations

In total we obtained 7 visibility measurements for IRS 9A and 17 for our calibrator HD 107446. The complete log of the observations can be found in Table A.3 in appendix A, while the most important information is also summarised in Table 4.2. Using the values of B_p and the position angle of the baseline we can create a map showing the coordinates of the measured points in the u - v -plane. The result is shown in Figure 4.5 for both IRS 9A and HD 107446. The u - v -coordinates of the two measurements of IRS 9A from the 3rd of March are almost perpendicular to the other ones. We chose this configuration in order to be able to detect a possible flattening of the emitting region around IRS 9A, that is, a dependence of the visibility on the position angle.

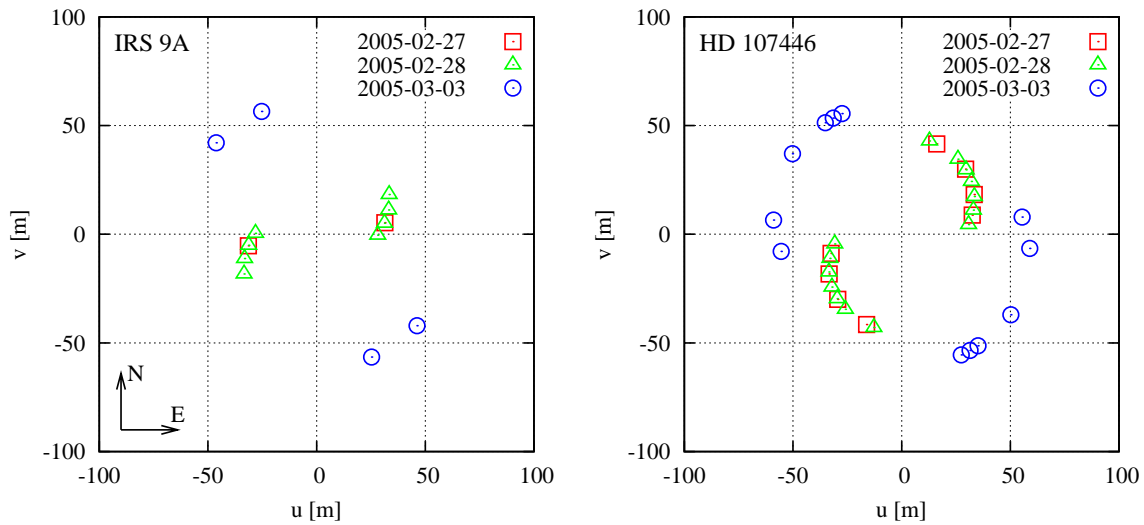


Figure 4.5: Coverage of the u - v -plane for the observations of IRS 9A (left) and HD 107446 (right). Note that u and v are given in meters as we did not divide by λ as in equation (2.18).

In the following chapter, we present the calibrated visibilities which we obtained from the data reduction with both MIA and EWS and summarise the main findings. In Section 4.4.2, we show and analyse the correlated fluxes, while the results of the two data reduction packages are compared and discussed in detail in Section 4.4.3. The differential phases are presented in Section 4.4.4.

4.4.1 Visibilities

The main results of the incoherent data reduction with MIA are shown in Figure 4.6, where the calibrated visibilities are plotted against wavelength. The results of the coherent analysis with EWS are presented in the same way in Figure 4.7. The legend of the latter figure has the same design as in Figure 4.3, that is, indicating the science and the calibrator measurement, but when using MIA we achieved the best results with time-averaged values of the calibrator visibilities. Therefore, the legend only specifies the time and date of the interferometric measurements of IRS 9A. This calibration was carried out within OYSTER, using a smooth Gaussian weighting function in order to average the calibrator measurements in time. The graphs from EWS have a finer structure because MIA bins three pixels together by default in order to increase the signal-to-noise ratio.

The visibilities of IRS 9A are fairly similar for all our projected baseline–position angle pairs. They are extremely small in the whole region from 9–13 μm where all measurements yield a visibility of less than 0.1. Yet for wavelengths smaller than 9 μm the visibility rises steeply, and close to the lower end of the atmospheric window it reaches values which are in the range of approximately 0.16–0.44 for MIA and 0.24–0.55 for EWS. This is the reason why we include all the values down to a wavelength of about

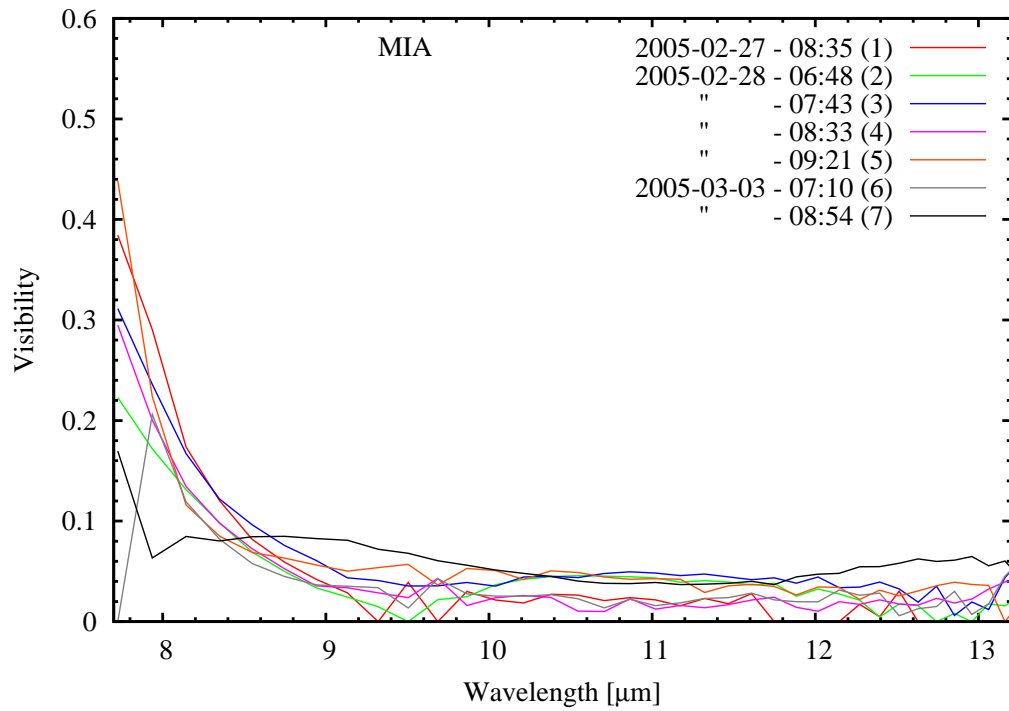


Figure 4.6: The calibrated visibilities of IRS 9A calculated within OYSTER with MIA.

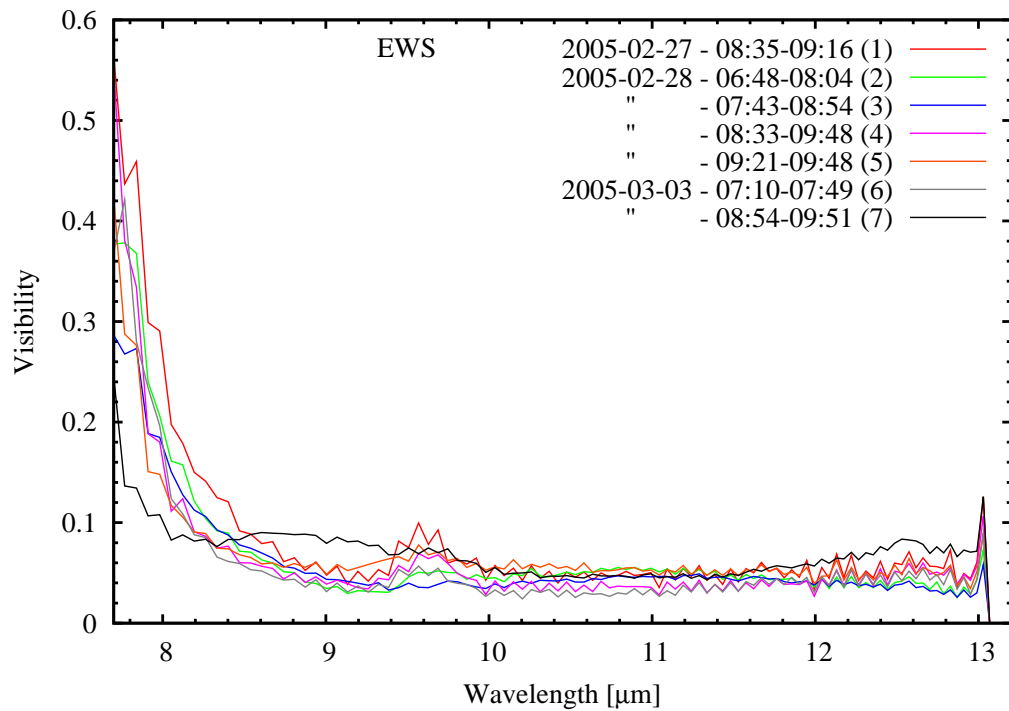


Figure 4.7: The calibrated visibilities of IRS 9A calculated with EWS. The small peaks at 13 μm are caused by the upper end of the masks and do not represent real data.

7.7 μm , while the majority of publications dealing with data from MIDI only include the data beyond 8 μm . Naturally, since the atmospheric absorption becomes stronger and stronger for wavelengths below 8 μm , the uncertainties of the measurements increase. This is partly responsible for the sizeable differences between some of the measurements in this range which have similar values of B_p and PA. Since the flux of IRS 9A is rather low towards the short wavelengths (see Figures 4.3 and 4.4), a careful inspection of the individual fluxes in this range is necessary in order to ensure that the visibilities are real. The ratio of the correlated flux to the total flux is a ratio of two numbers which are both fairly close to zero in this case. However, at a wavelength of about 8 μm , the total flux of IRS 9A lies in the range of 2–4 Jy for all our measurements and almost all visibilities are smaller than 0.5. Hence we are certain that the steep gradient of the visibilities is not an artefact of the above-mentioned problems, but caused by the intrinsic structure of IRS 9A.

The MIA-visibility of the sixth observation (grey line) drops to zero below 8 μm . This is not observed when reducing the same observation with EWS and we attribute it to an erroneous calibration. Hence there is only one measurement which significantly deviates from the other six, namely the seventh observation (black curve), which shows a very similar behaviour with both MIA and EWS. Compared to the sixth observation which was obtained during the same night, the lengths of the projected baselines are almost the same and also the position angles differ by only 24 degrees. Hence one would expect visibilities with a similar shape and of a similar magnitude. Yet the sixth measurement is consistent with the other five, while the seventh measurement is not. We will discuss possible reasons and implications in Section 4.4.3.

Some of the visibilities from EWS show a slight bump around 9.6 μm . This is a remnant of the strong ozone absorption in the atmosphere and does not reflect a change in the structure of IRS 9A (compare with Section 4.3.1).

4.4.2 Correlated flux

Figure 4.8 shows the correlated fluxes we obtained from MIA and EWS. It is immediately obvious that the EWS software produces better results in the region where the visibilities lie below 0.1, that is, for wavelengths larger than about 9 μm . Here, the results from MIA deviate strongly from each other and the individual curves have a very ragged appearance (some even show zero-values), while the ones from EWS are much more consistent. On the other hand, the correlated fluxes from EWS show a large scatter below 8 μm . A possible explanation for this behaviour will be given in the next chapter. For a comparison with other sources that were observed with MIDI and which have very low (correlated) flux levels, see, for example, Matsuura et al. (2006) and de Wit et al. (2007).

4.4.3 Comparison and results

When comparing the overall shape of the visibilities, it is obvious that the two data reduction packages agree very well with each other. Larger differences exist between indi-

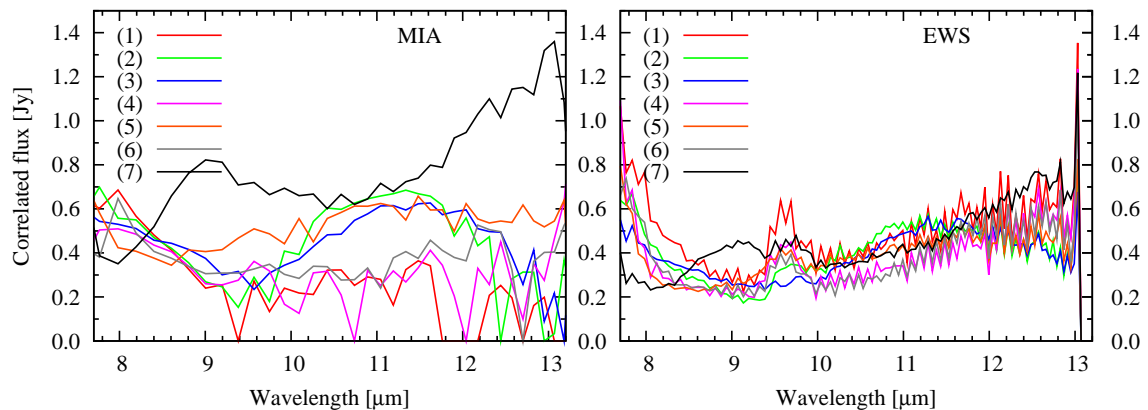


Figure 4.8: The correlated fluxes from MIA (left) and EWS (right). The graphs from EWS again show the sharp peak at 13 μm which is due to the masks.

vidual measurements, which we primarily attribute to three reasons. First, the total flux of IRS 9A below 8 μm is only about 2–4 Jy which is close to the limiting magnitude of MIDI without external fringe tracking (compare with Table 3.1 on page 40). This makes reliable measurements of the flux and the fringe amplitude generally more difficult, and increases the uncertainties which are expected to lie in the range of 10–15 % even for sufficiently bright sources. Second, almost all of our values of the correlated flux are smaller than 1 Jy, a large fraction of them being even smaller than 0.5 Jy. This increases the uncertainty and the scatter of the measurements throughout the N band. Third, MIA and EWS do not use the same masks in order to extract the signal from the detector (see Sections 4.1.1 and 4.1.2). While the interactively computed masks from MIA might yield better results in some cases, the fixed mask of EWS might be advantageous in other cases.

In Figure 4.9 we plot the relative difference between the visibilities from MIA and EWS, that is, the absolute value of $(V_{\text{MIA}} - V_{\text{EWS}})/V_{\text{mean}}$, where $V_{\text{mean}} = (V_{\text{MIA}} + V_{\text{EWS}})/2$. In order to obtain meaningful results, we do not use the MIA visibilities from Figure 4.6 (i.e. the ones with time-averaged calibrators), but rather employ individual calibrator measurements for each observation of IRS 9A, as in the data reduction with EWS. Therefore, the legend in Figure 4.9 is valid for both the visibilities from MIA and from EWS. We only show the wavelengths from 7.7 μm to 9 μm since the values of the visibility in the remaining part of the N band are too close to zero to yield useful results. Except for the values at the lower end of the atmospheric window, most of the measurements do not deviate by more than 20 % from each other. These discrepancies can be slightly reduced by using the same mask in both reduction packages, that is, by running MIA with the mask from EWS or EWS with the masks that are computed by MIA. However, even in this case differences of up to 20 % remain for some measurements, which we attribute to the faint total and correlated fluxes.

Coming back to the rather large uncertainties of the few values at the very beginning of the N band, we give an explanation for the fact that some of the visibilities from EWS

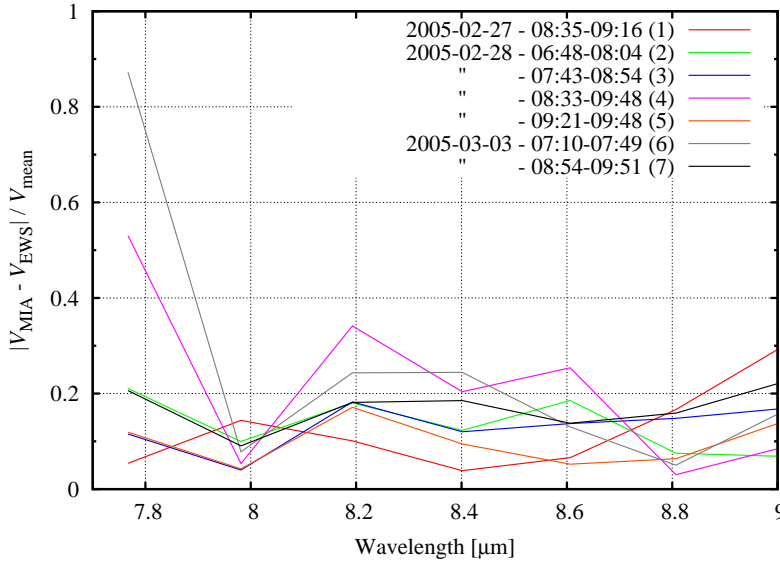


Figure 4.9: The absolute value of the relative difference between the visibilities from MIA and EWS. Note that we do not show the results for the full N band, but only the wavelength range from 7.7 μm to 9 μm (see text).

are substantially larger than the corresponding visibilities from MIA (see Figures 4.6 and 4.7). This is probably due to the underestimation of the fairly faint total flux of IRS 9A. The problem can occur when the signal-to-noise ratio of the science target is too low, whereas the (usually) brighter calibrator star is correct (see Chesneau 2007). In order to check whether this is the case, one can compare results which were obtained with different binning parameters, because a larger bin size during the reduction process leads to a higher SNR. We can simply use the standard results from MIA and EWS for this. It appears that EWS seems to overestimate the visibilities of measurements 1, 4, 6 and possibly also number 2. Since the measurements with the higher SNR are more reliable, we only trust in the values from MIA in these cases (and in the range from 7.6–8 μm).

As mentioned earlier, only the last measurement deviates from the other six and this is observed in the results from both MIA and EWS. The visibility curve shows a rather broad bump around 8.8 μm and also rises to a slightly higher level in the range from 12–13 μm . While these deviations do not exceed a factor of about 2 compared to the remaining visibilities (which are all smaller than 0.1), there is still the question of whether this result is simply due to an erroneous measurement or reflects a change of the structure of IRS 9A when changing the position angle from 132 to 156 degrees. Since these two angles differ by only 24 degrees, we tried to rule out other possible explanations. The acquisition images can reveal an insufficient overlap of the two beams, but this does not seem to be the case either for the measurement of IRS 9A or for the one of HD 107446. The latter is confirmed by comparing the instrumental photometry and visibility of this measurement with the ones from a different measurement from the same night. A closer look at the plots in the graphical user interface of MIA also did not reveal any anomalies compared to the other measurements. Therefore, we conclude that the structure of IRS 9A is slightly different for the spatial scales and orientations which are probed by the two last observations.

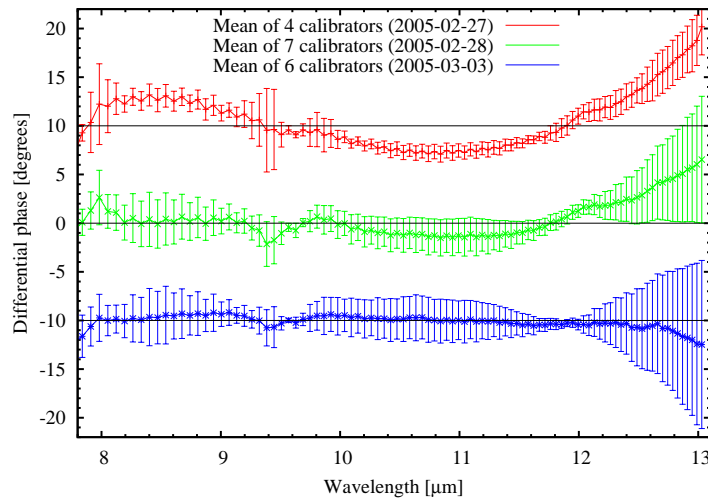


Figure 4.10: Mean differential phases of the calibrator measurements. The data from the first night are shifted by +10 degrees, while the data from the third night are shifted by -10 degrees and lines of zero phase have been drawn for all three measurements to guide the eye. Error bars represent the standard deviation.

4.4.4 Differential phase

Data reduction with the EWS method has the advantage that the relative phase of the signal between the different spectral channels, the so-called differential phase, is conserved. This quantity can yield information about the geometry of the source being observed. While point symmetric objects have a (constant) differential phase of zero, asymmetric objects show non-zero values of the differential phase, indicating different positions of the photo-centre at different wavelengths.

As discussed in Section 2.8, the intrinsic phase of the complex visibility cannot be measured with MIDI and also the differential phase is affected by the atmosphere. On the one hand, the atmosphere produces a large offset for the values of the differential phase, and on the other hand it causes small variations since the two light beams pass through different amounts of air and water vapor, changing the index of refraction (see the description of the EWS data reduction scheme in Jaffe 2004 and also Deroo et al. 2007 and Fedele et al. 2008). The first effect is linear with respect to frequency and the EWS software subtracts a fit to this component from the measured differential phases, leaving only the second effect caused by the unequal light paths. The magnitude of this effect is usually small and can be analysed with the observations of HD 107446. Since this star appears as a point source to MIDI, any deviation from zero differential phase cannot be due to the source geometry but has to be caused by the atmosphere. Therefore, we expect the measurements to be time-dependent and to (slightly) deviate from zero, but on average they should be reasonably constant and close to zero.

Figure 4.10 shows the average values of all the calibrator measurements for the three observing nights. Except for the wavelengths above approximately $12.5 \mu\text{m}$, the differential phases of HD 107446 always lie within ± 3 degrees relative to zero. This is very close to the theoretical result and indicates quite stable observing conditions during the three nights. In particular, the measurements from the second and third night are very close to zero, while those from the first night are in very good agreement with each other, leading

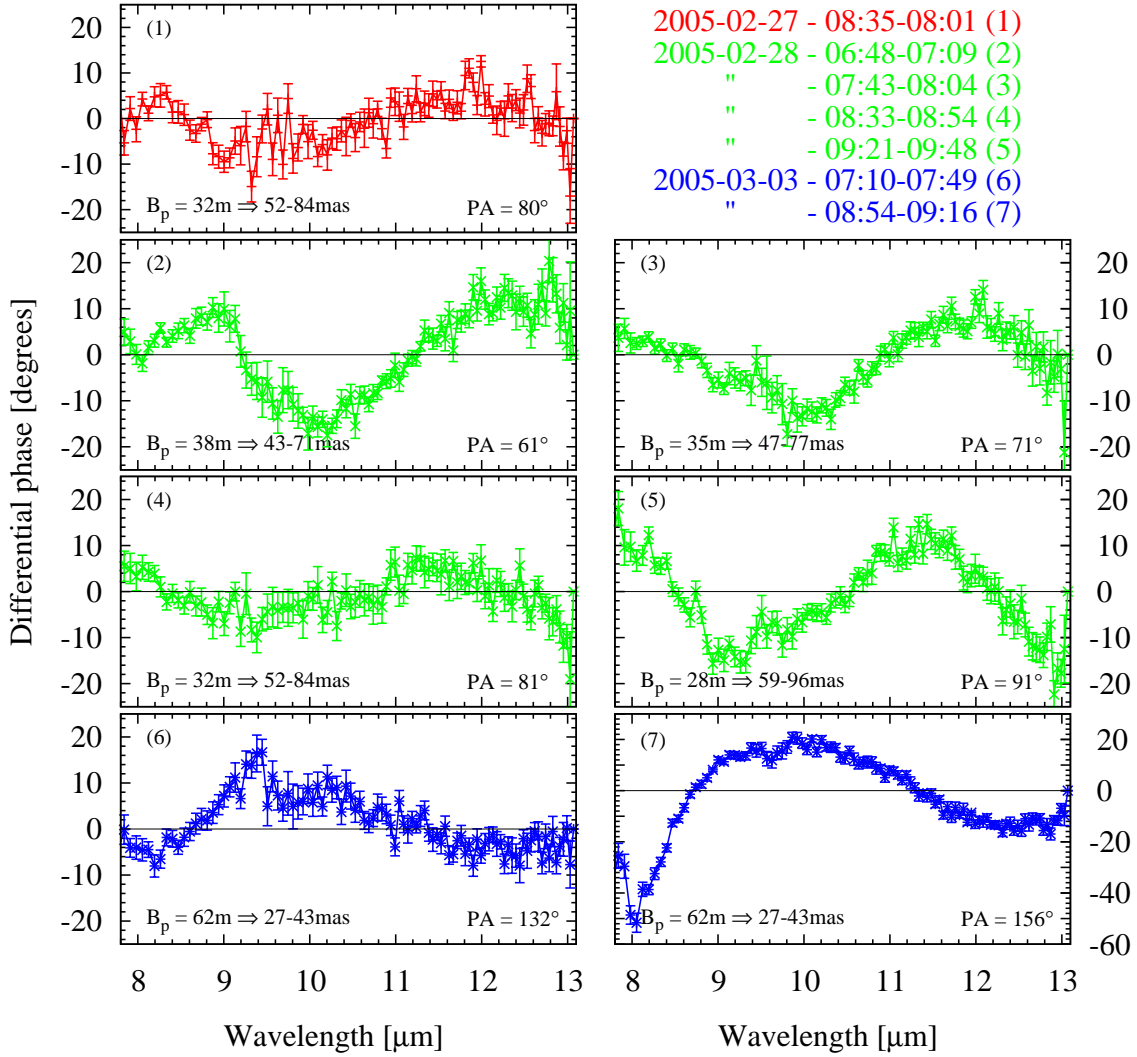


Figure 4.11: The differential phases of IRS 9A. Different colours refer to different observing nights as indicated in the top right corner. The two time specifications after the date refer to the science and the calibrator measurement, respectively (compare with Table A.3). The lengths of the projected baselines, the corresponding angular scales (for $8\ \mu\text{m} \leq \lambda \leq 13\ \mu\text{m}$) and the position angles are also shown. Note the different scale for observation number seven, which is also responsible for the “smaller” error bars.

to smaller error bars. The large error bars above wavelengths of about $12.5\ \mu\text{m}$ indicate larger deviations between the single observations, which is probably connected with the end of the atmospheric window in this region.

In order to calibrate the differential phases of IRS 9A one simply has to subtract the differential phases of HD 107446 from them. Here, one can choose between subtracting the mean value from the particular night, or subtracting the calibrator measurement with the smallest difference in time to the science measurement. We compared the results of the two alternatives and found only small quantitative differences while the overall trends

remain the same. In the following, we present the results of the second method, that is, each science measurement has its own calibrator.

The differential phases of IRS 9A are shown in Figure 4.11 together with additional information on each observational setup. Except for the last observation, we don't detect very strong asymmetries of the wavelength-dependent brightness distribution, but IRS 9A is clearly deviating from point symmetry. Without taking the last measurement into account, the values of the differential phase vary on scales of roughly ± 10 – 20 degrees. This is much larger than the variations observed in the calibrator measurements and hence is caused by intrinsic shifts of the photo-centre of IRS 9A with wavelength. We detect the smallest phase shifts at around $B_p = 32$ m and $PA = 80^\circ$, that is, for the first and the fourth observation. Both for slightly shorter and longer projected baselines as well as for smaller and larger position angles, the amplitudes of the differential phase signal increase while showing a similar, nearly sinusoidal pattern. The position of the peaks, however, changes between the observations and seems to move to smaller wavelengths with decreasing angular resolution.

The differential phases of the sixth observation vary in a slightly different way, but on a comparable scale, while the last observation shows a large phase shift around $8 \mu\text{m}$. Since the calibrator measurements do not show any unusual behaviour at this wavelength, the phase shift indicates a considerable discrepancy between the location of the photo-centre of IRS 9A at $8 \mu\text{m}$ and at $10 \mu\text{m}$, the differential phase changing from roughly -50 to $+20$ degrees. The corresponding spatial scale is about 30 mas (210 AU at 7 kpc).

4.5 Interim summary

In the previous chapters we presented the main results of our observations with MIDI. They are summarised hereafter and we also discuss their shortcomings and possible implications for the modelling.

Acquisition images:

- ▷ IRS 9A is partly resolved by a single 8 m telescope in the mid-infrared.
- ▷ Its structure is slightly asymmetric on these large scales. The asymmetries are mainly oriented towards the southwest and southeast.
- ▷ The mean sizes (FWHM) of the images are 358 mas for the north-south direction and 459 mas for the east-west direction (approximately 2500 AU and 3200 AU, respectively, for a distance of 7 kpc).

Spectra:

- ▷ The emission of IRS 9A rises steeply towards longer wavelengths, starting at 2 – 4 Jy at the lower end of the N band and ending at about 14 – 16 Jy at the upper end.
- ▷ We do not detect a silicate feature in the spectrum of IRS 9A.
- ▷ We do detect the [Ne II] emission line at $12.81 \mu\text{m}$.

Visibilities and correlated fluxes:

- ▷ The visibilities above a wavelength of about $9\ \mu\text{m}$ are always smaller than 0.1 and show that the radiation of IRS 9A is fully resolved by MIDI on spatial scales from 30 mas to 95 mas and for wavelengths from $9\ \mu\text{m}$ to $13\ \mu\text{m}$.
- ▷ A more compact structure emerges at wavelengths smaller than $9\ \mu\text{m}$, where the visibility reaches values of about 0.4 or 0.5 for some of our observations.

Differential phases:

- ▷ The differential phases clearly deviate from zero and show that the position of the photo centre of IRS 9A changes with respect to wavelength, spatial resolution and position angle.
- ▷ The last measurement shows a much stronger phase shift around $8\ \mu\text{m}$.

The analysis of the acquisition images revealed a slightly inferior quality of the “B” images compared to the “A” images. However, the effect is very weak and does not play an important role for the general conclusions. Concerning the modelling of IRS 9A, two key facts have to be considered. First, the structure around IRS 9A is quite extended, and observations with a single telescope already partly resolve the source. Second, the emitting region appears to be slightly asymmetric, but only on very large scales. The models will have to account for the former issue, but whether the latter issue can be reproduced by the models remains to be seen (see discussion in Chapter 7).

The absolute differences between the flux of the individual calibrated spectra range up to 20 %, which is typical for observations in the N band, while the shapes of the spectra are in very good agreement with each other. Therefore, the point-to-point accuracy is actually much better than indicated by the error bars in Figure 4.4. When trying to model the SED of IRS 9A, we will not include the [Ne II] emission line, but the absence of the silicate feature is a crucial aspect and the models should be able to reproduce it. In Section 5.2 we will present the spectrum of IRS 9A as measured by Spitzer. It covers a broader range of wavelengths with higher spectral resolution and hence helps to improve the SED of the models.

All our measured visibilities demonstrate that the MIR emission from IRS 9A is completely resolved for wavelengths in the range of $9 - 13\ \mu\text{m}$ and projected baseline lengths of more than 28 m. The steep increase of the visibilities towards the lower end of the N band is quite unusual and will possibly restrict the range of suitable models to a great extent. While almost all the flux beyond $9\ \mu\text{m}$ originates solely from the surroundings, the unresolved fraction of the flux increases rapidly below this wavelength. Here, a very compact structure emerges either due to a change in the opacity of the intermediate material, or due to the emission characteristics of the compact structure itself, or a combination of both effects.

5 Observations and data reduction II – Gemini South and Spitzer

Apart from the MIDI data presented in the previous chapter, we also used data which was obtained from other telescopes and instruments for our analysis of IRS 9A. We received visibilities as well as an image from an aperture masking experiment at the Gemini South telescope. Since IRS 9A is nearly fully resolved by MIDI, these visibilities represent a very valuable extension of our interferometric data to shorter baselines and the image can be compared to our acquisition images. We could also use spectroscopic data from the Spitzer Space Telescope. This spectrum has both higher resolution and, due to the absence of the atmosphere, covers a larger range of wavelengths. The latter is especially useful when we evaluate the SEDs of our models in Chapter 6.

5.1 Aperture masking observations at Gemini South

On the third of January, 2005, John D. Monnier and collaborators observed IRS 9A with the Thermal-Region Camera Spectrograph (T-ReCS) at the Gemini South Observatory. The T-ReCS instrument, described in de Buizer & Fisher (2005), is a mid-infrared imager and long-slit spectrograph, optimised for the wavelength range between 8 μm and 26 μm . For further information about the instrument and the telescope we refer to the web page of the Gemini Observatory¹.

The group used the aperture masking technique in order to obtain a diffraction limited image of IRS 9A. This technique was first described by Rhodes & Goodman (1973), and Baldwin et al. (1986) demonstrated its applicability to the observation of astronomical objects. More recent descriptions of aperture masking interferometry can be found in Monnier (1999) and Tuthill et al. (2000), which both describe the experiment at the Keck I telescope. The basic principle can be described as follows. A mask containing a series of small holes (subapertures) is placed either in the (re-imaged) aperture plane or in front of the secondary mirror, which effectively converts a single telescope into a separate-element interferometric array. One can then use the well established methods from radio interferometry (e.g. CLEAN or MEM) to recover a diffraction limited image from the visibility and closure phase information.

¹<http://www.gemini.edu/>

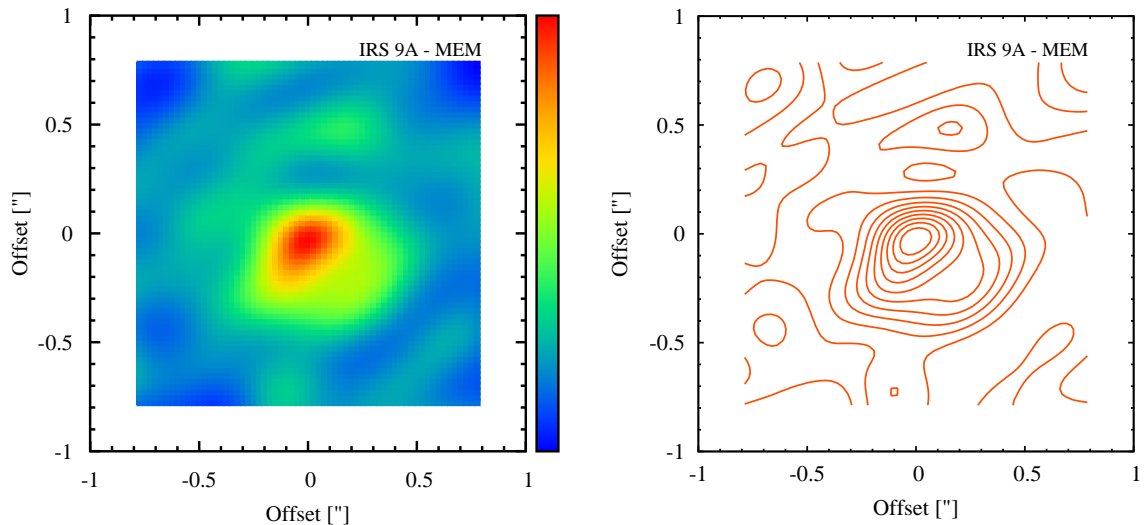


Figure 5.1: The image of IRS 9A which was recovered from the aperture masking data shown as a colour map to the left and with contour lines to the right. The twelve contour lines are calculated in the same way as for the acquisition images, i.e., they lie at about 0.4, 1, 2, 3.7, 6.3, 10, 15, 22, 32, 44, 59 and 77 % of the maximum value. North is up and east to the left.

We used both the image and the visibilities obtained by John D. Monnier (priv. communication) in order to compare them with the results from MIDI and to constrain our models. The data were taken at $11.7 \mu\text{m}$ with the Si-5 filter ($\lambda_c \pm \Delta\lambda = 11.66 \pm 0.57 \mu\text{m}$). Figure 5.1 shows the image which was recovered from the aperture masking data with the maximum entropy method (MEM; see, e.g., Cornwell & Evans 1985). The image is 64×64 pixels in size and spans roughly 1.6×1.6 square arcseconds on the sky, which is quite similar to the acquisition images from MIDI. Since the primary mirror of the Gemini South Telescope has a diameter of 8.1 m, the spatial resolution should also approximately be the same. When comparing Figure 5.1 with our acquisition images (see page 49 and 51), we find the following similarities. The aperture masking image confirms our finding that the emission of IRS 9A is already partly resolved by an 8 m class telescope in the MIR. It also shows that the shape of the emitting material deviates from point symmetry, with some material extending towards the south-west and south-east directions. The faint source which we already mentioned in Section 4.2.1 can be seen more clearly now. It is located about 0.1 arcseconds to the west and 0.5 arcseconds to the north of IRS 9A.

In comparison to a “real” optical interferometer, that is, an interferometer consisting of multiple telescopes, aperture masking observations have a much better coverage of the u - v -plane, which allows the reconstruction of images in the first place. The coverage for the observations of IRS 9A is shown together with the visibilities in Figure 5.2. Obviously, the sampling of both the projected baselines and of the position angles is far better than for our observations, and the u - v -plane is filled quite homogeneously in this case. The mask has seven sub-apertures, which leads to a total number of 21 baselines \vec{B} . However, there are only seven different projected baselines B_p , ranging in length from 1.8 m to 6.3 m.

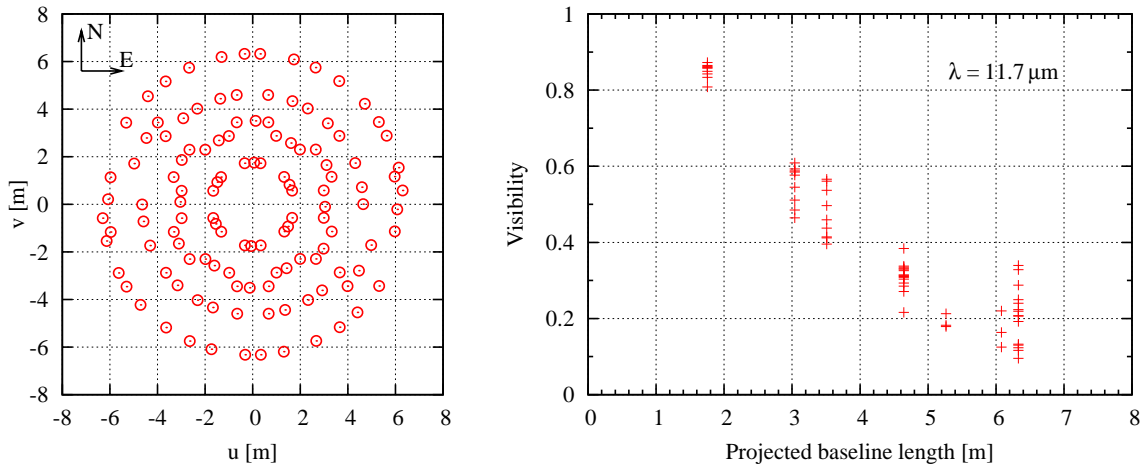


Figure 5.2: The u - v -coverage and the visibilities of the aperture masking observations.

Together with the observing wavelength of $11.7 \mu\text{m}$ this leads to an angular resolution of about 1.4 to 0.4 arcseconds.

Due to this substantially lower resolution, the measured visibilities are much higher than the ones from MIDI. They start at around 0.8–0.9 for the shortest baseline and drop to about 0.1–0.3 at the longest baselines, while showing a considerable scatter at each of these measurements. This is mostly due to the fact that measurements with the same value of B_p comprise different values of the position angle. The scatter is quite small for the shortest baseline, about ± 0.05 of the absolute value, but reaches roughly ± 0.1 or even more at the longer baselines where the resolution is high enough to resolve the outer parts of IRS 9A. A suitable model will have to reproduce the visibilities from MIDI as well as the ones from T-ReCS.

5.2 Spitzer/IRS data

The NGC 3603 star cluster and the MIR sources in its surroundings were observed with the Spitzer Space Telescope by Vianney Leboutteiller and collaborators. Their results are published in Leboutteiller et al. (2007) and Leboutteiller et al. (2008). As part of their observing campaign, they selected several infrared bright sources for follow-up spectroscopy with the Infrared Spectrograph (IRS). Among these sources they also selected IRS 9A and V. Leboutteiller kindly provided us with the calibrated dataset. The Spitzer Space Telescope is described in Werner et al. (2004), the IRS in Houck et al. (2004) and additional information can be found on the web page of the Spitzer Science Center².

The Spitzer Space Telescope is, of course, not influenced by any of the troublesome effects of the atmosphere and always produces diffraction limited images. However, the

²<http://ssc.spitzer.caltech.edu/>

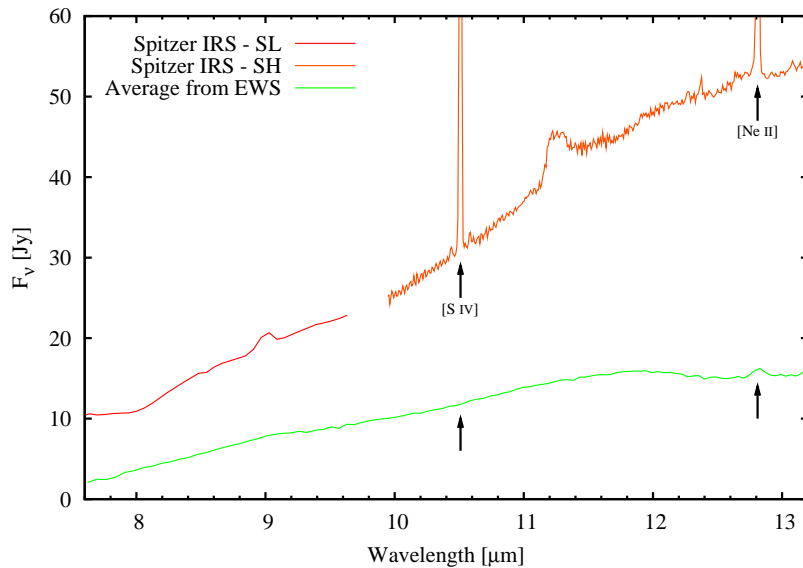


Figure 5.3: The spectrum from Spitzer compared to the average spectrum from EWS with the two most prominent emission lines labelled. The data from the SL module have been scaled to match the SH spectrum (see text for more information).

diameter of the telescope’s primary mirror is 0.85 m, which is almost ten times smaller than the primary mirrors of the UTs or of the Gemini South telescope. This leads to an equivalent decrease in angular resolution, which is about 3 arcseconds for $\lambda = 10 \mu\text{m}$. As a consequence, Spitzer collects flux from a much larger area around IRS 9A than MIDI, and the overall flux is considerably higher due to both the extended emission from IRS 9A itself as well as background emission (see the small inset in Figure 1.2). As with the correlated and total fluxes from MIDI, this offers the opportunity to locate the origin of spectral features (see below).

Spitzer’s IRS consists of four modules, with each module covering a different wavelength range. For IRS 9A we use the data from the short-low (SL) and short-high (SH) modules, which cover the ranges from 5.2 – 14.5 μm and 9.9 – 19.6 μm with spectral resolutions of around 60 – 127 and 600, respectively. The MIR sources around NGC 3603 were also observed with the low-high (LH) module, covering the range of 18.7 – 37.2 μm , but for the case of IRS 9A both the continuum and the emission lines were saturated. This is also true for the SL module for wavelengths above 9.7 μm , which results in a small gap in the spectrum from 9.6 μm to 9.9 μm . Since the aperture sizes of the slits are not the same, the spectra from different modules have to be scaled if the source is (partly) resolved by Spitzer. This is the case for IRS 9A, but for the slit sizes and details of the stitching process we refer to Lebouteiller et al. (2007, 2008) and the web page. In Figure 5.3 we present the part of the Spitzer spectrum which corresponds to the region of the N band in comparison to the average spectrum from EWS.

The flux in the spectrum from Spitzer is roughly 2.5 – 3 times larger than in the average spectrum from EWS, which we attribute mostly to the low spatial resolution of Spitzer. As mentioned earlier, MIDI’s resolution is about ten times better when observing with a single telescope. The smallest differences between the spectra are found in the middle of the N band, while they even exceed the denoted range close to the edges of the atmospheric

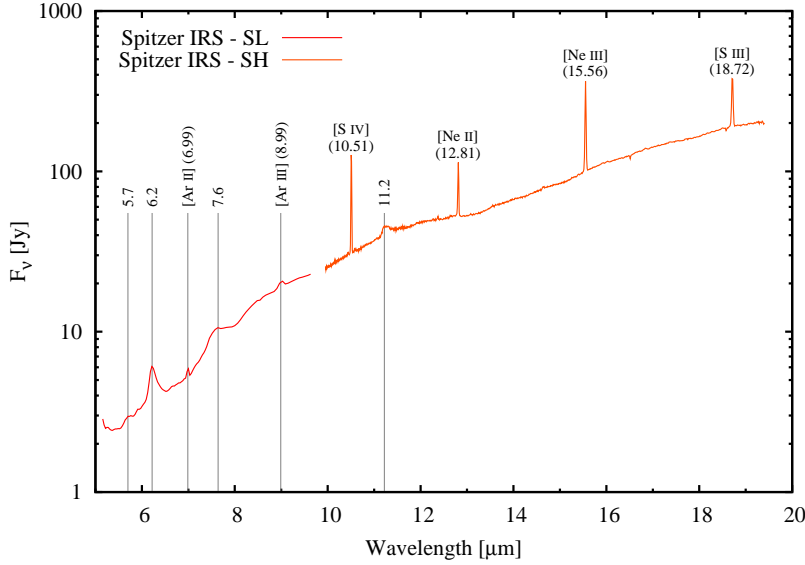


Figure 5.4: The entire spectrum from Spitzer. The forbidden emission lines are labelled with name and wavelength in round brackets, the PAH features with wavelength only.

window where the absorption becomes stronger. The silicate feature is not detected in the Spitzer spectrum as well, yet there are numerous other emission features or lines present. We will briefly discuss them when presenting the full spectrum from Spitzer in the next section. Interestingly, the [Ne II] forbidden emission line is the only spectral feature that is also present in the MIDI data. While the spectral resolution and sensitivity of MIDI might be insufficient to detect the two rather weak features at 9 μm and 11.2 μm , the [S IV] emission line at 10.51 μm should have been detected. According to Leboutteiller et al. (2008), its line flux is more than two times larger than that of the [Ne II] line. Consequently, the [S IV] line has to be emitted by material which is considerably further away from IRS 9A than the material producing the [Ne II] line. A discussion about the physical mechanisms that cause [Ne II] emission in young stars can be found in van Boekel et al. (2009) and the references therein. Depending on the parameters of the system, it may be caused by outflows that are related to strong accretion activity or by irradiation of the disk surface by stellar X-rays. As we already mentioned in Section 1.3.3, IRS 9A is not detected in the Chandra observations by Moffat et al. (2002), suggesting ongoing accretion and outflow activities.

5.2.1 Spectral index, emission lines and PAH features

In Figure 5.4 we present the full spectrum of IRS 9A from Spitzer, extending from 5.2 μm to 19.4 μm . The spectrum is composed of a thermal continuum from the dust around IRS 9A and superimposed are numerous PAH features and forbidden emission lines. The value of the spectral index α_{IR} , where $\alpha_{\text{IR}} := d \log \lambda F_{\lambda} / d \log \lambda$ is the slope of the SED, was first calculated by Nürnbergger (2003). He obtained $\alpha_{\text{IR}} = 1.37$ in the wavelength range from 2.2 μm to 11.6 μm , using the 2.5 m telescope from the Las Campanas Observatory and the 3.6 m telescope from the La Silla Observatory, respectively. This value designates

IRS 9A as a Class I protostar according to the standard classification scheme for low- to intermediate mass stars (see Myers et al. 1987; Lada 1987; Adams et al. 1987; André et al. 1993; McKee & Ostriker 2007). With our data from MIDI and Spitzer we are now able to recalculate this value and also to extend the range of wavelengths. However, it is important to note that the different aperture and slit sizes of the telescopes will strongly influence the value of α_{IR} . This can already be seen in Figure 5.3 from the previous section, where the slope of the SED as measured by Spitzer is clearly much steeper than that measured by MIDI.

We calculated the spectral index for the following wavelength ranges: $\alpha_{2.2-10\mu\text{m}}$ (NIRCAM–MIDI), $\alpha_{2.2-10\mu\text{m}}$ (NIRCAM–Spitzer), $\alpha_{2.2-19.4\mu\text{m}}$ (NIRCAM–Spitzer) and $\alpha_{5.25-19.4\mu\text{m}}$ (Spitzer–Spitzer), where the corresponding telescopes or instruments are given in parenthesis (see also table 1.3). Given the sequence above we obtain values of 1.10, 1.70, 1.83 and 2.34. Since MIDI offers the highest (spatial) resolution and, consequently, picks up much less radiation from the surroundings, using its measured flux at 10 μm in combination with the flux from NIRCAM leads to the smallest value of the spectral index. The equivalent flux from Spitzer, on the other hand, leads to a much larger value, as is also the case with the third combination, shifting the upper wavelength to 19.4 μm . The fourth value cannot be easily compared to the other three because the smaller wavelength changed from 2.2 μm to 5.25 μm . We do not plan to discuss the individual values here. The bottom line is that the spectral index of IRS 9A is always clearly larger than zero, confirming the prior result by Nürnberger (2003).

The spectrum contains several forbidden emission lines. Among these are the [S IV] and [Ne II] lines which we mentioned before, but also [Ne III] at 15.56 μm and [S III] at 18.71 μm . The [Ar II] and [Ar III] lines at 6.99 μm and 8.99 μm , respectively, are also detected, but are much weaker compared to the other four lines. The line fluxes and additional information can be found in Lebouteiller et al. (2007, 2008).

The PAH features imply the presence of complex carbonaceous material excited by UV radiation. They have been known since the 70s (originally called the “UIR” or unidentified infrared bands) and were identified as the vibrational modes of free-flying PAHs in the 80s (Duley & Williams 1981; Leger & Puget 1984; Allamandola et al. 1985). They are now known to be quite ubiquitous and found close to stars as well as in the diffuse ISM. For a general overview of PAHs and other spectral features in the IR we refer to van Dishoeck (2004) and the references therein.

6 Modelling

As discussed earlier in Chapter 2, optical interferometry is a powerful yet indirect method to get high spatial resolution information of astronomical objects. The quite sparse coverage of the u - v -plane does not usually allow the reconstruction of an image of the source, but calls for models in order to get more detailed information about the structure and/or dynamics. These models should be able to reproduce the visibility as well as the spectral energy distribution of the object, which, in combination, can prove to be quite challenging. This is especially true in our case, since the visibilities from MIDI are complemented by the ones from the aperture masking observations at the Gemini South telescope, which together span a very large range of spatial frequencies.

In this chapter we describe the aims, methods and limitations of our different modelling efforts, starting with the most simple models and subsequently going over to the more sophisticated ones, giving a brief discussion of the results and implications in each case. In Section 6.1 we try to model the visibilities of IRS 9A with simple brightness distributions in order to get a first idea about its inner structure on scales below ≈ 100 mas. Since this is only a “first step”, we do not try to fit these models to both sets of visibilities, but use the ones from MIDI only. The SED is also not considered at this point. We then move on to more physically motivated models in Section 6.2, starting with the one-dimensional radiative transfer code DUSTY and subsequently using MC3D, a three-dimensional continuum radiative transfer code based on the Monte Carlo method. Finally, we discuss the results of fitting the Spitzer spectrum to a large grid of young stellar object SEDs in Section 6.3.

6.1 Simple brightness distributions, binary and accretion disk models

Although simple brightness distributions like a Gaussian or a uniform disk will most likely not provide an accurate representation of the real geometry of the source, they are very useful as a first step on the way to more complex models. These usually incorporate a lot of free parameters and also more complex physics, which is why their results have to be treated very carefully and can be easily misunderstood. The simple models, on the other hand, can be described by a few basic equations which are easily implemented in a small fitting routine and yield first estimates of quantities like the angular size, inclination and orientation of the emitting region. These values can then serve as input values for

the more complex models or, depending on the fitting results, some models may even be excluded from the further modelling process at a very early stage (for example a binary).

Our approach is based on the method presented by Eisner et al. (2003, 2004), who investigated several Herbig Ae/Be stars that were observed with the Palomar Testbed Interferometer at $2.2\ \mu\text{m}$. Since we measured the spectrally dispersed visibility of IRS 9A in the N band, we are in principle able to model the visibility separately for each spectral channel. However, this approach does not lead to useful results due to the rather special shape of IRS 9A's visibilities, that is, the fact that they are approximately zero for wavelengths larger than about $9\ \mu\text{m}$. In this range we cannot constrain the size of the emitting region, but only give a lower limit. Every brightness distribution that is large enough leads to a "good fit" here. Hence, instead of fitting our full set of visibilities, we only use the values at $\lambda = 7.98\ \mu\text{m}$. This wavelength has the advantage that all seven visibilities are clearly nonzero, while at the same time the results from MIA and EWS agree very well with each other (compare with Figure 4.9 in Section 4.4.3).

6.1.1 Gaussian, uniform disk, ring

The equations describing these brightness distributions and the corresponding visibilities were already listed in Section 2.9. They are described by their angular size θ , conveniently measured in mas. In the case of the Gaussian brightness distribution, θ is taken as the FWHM value, whereas for the uniform disk model, θ is simply the angular size of the disk. The ring model has two different angular sizes, the inner and the outer rim, and we take θ to be equal to the size of the inner rim. The outer rim can then be written as $\theta_{\text{out}} = (1 + f)\theta_{\text{in}} = (1 + f)\theta$, with $f = w/r > 0$, where r is the radius of the inner rim and w the width of the ring. Instead of introducing one more free parameter, the value for f is taken from radiative transfer models of puffed-up inner disks by Dullemond et al. (2001). We adopt their value of $f = 0.27$ for stars earlier than spectral type B6.

In order to allow for inclination effects, we introduce two more free parameters: the inclination angle ϕ and the orientation angle ψ (measured east of north). An inclination of $\phi = 0$ corresponds to a face-on brightness distribution, in which case the orientation ψ does not have any effect on the appearance of the model. Using these two angles we can include inclination effects via a simple coordinate transformation:

$$x' = x \sin \psi + y \cos \psi, \quad y' = (y \sin \psi - x \cos \psi) / \cos \phi, \quad (6.1)$$

$$u' = u \sin \psi + v \cos \psi, \quad v' = \cos \phi (v \sin \psi - u \cos \psi), \quad (6.2)$$

where (x, y) and (u, v) are the original coordinates and (x', y') and (u', v') the transformed coordinates (equations (4) and (5) of Eisner et al. 2004). With these definitions an inclined (i.e. flattened) brightness distribution is elongated in the north-south direction and turns clockwise with increasing values of ψ .

The parameter range for θ should probe a range of spatial scales which encloses the one from our measurements. The projected baselines range from 28.1 m to 62.5 m (see

Tables 4.2 or A.3) which translates to an angular resolution of roughly 25 mas to 60 mas for $\lambda = 8 \mu\text{m}$. Since the code for these simple models is very fast, we vary θ from 1 mas to 200 mas in increments of 1 mas. As for the inclination and orientation, we vary ϕ from

Model	θ [mas]	ϕ	ψ	χ_r^2
Gaussian	68.5	64°	151°	14.54
UD	74.5	59°	135°	10.68
Ring	47.0	60°	115°	2.46

Table 6.1: Best-fit parameters of the Gaussian, uniform disk and ring models.

0° (face-on) to 90° (edge-on) and ψ from 0° to 180° , both in increments of 1° . We do not vary ψ up to 360° because all of the models are point symmetric and orientations of, for example, 70° and 250° cannot be distinguished. The results of this modelling approach are summarised in Table 6.1, where we show the parameters of the best fits and the corresponding values of χ_r^2 .

6.1.2 Binary and accretion disk models

The binary model also uses θ and ψ as free parameters, but θ is now interpreted as the angular separation of the two components. Because the binary model resulted in very high values for χ_r^2 , we extended the range of possible angular separations up to 1 as. Instead of the inclination ϕ , the brightness ratio of the two components R is the third free parameter (see equation (2.48)), varying from 0.1 to 1 in increments of 0.01. The inclination of the system cannot be determined since it is not possible to distinguish any nonzero inclination from a smaller (projected) angular separation of the two components. In the case of the accretion disk model, θ is taken as the size of the inner rim of the disk, that is, $\theta = 2r_{\text{in}}$, while ϕ and ψ determine its orientation. The values for the radius of the inner rim

Model	θ [mas]	R	ψ	χ_r^2
Binary	473.1	1.0	35°	87.18
		ϕ		
Accretion disk	20.6	61°	137°	8.58

Table 6.2: Best-fit parameters of the binary and accretion disk models.

vary from 10 AU to 100 AU. The disk is a geometrically thin, irradiated accretion disk as described in Eisner et al. (2003) and references therein. The temperature at the inner boundary is 1500 K and the disk is truncated at an outer boundary which is the lesser of 2000 AU or the radius at which the temperature falls below 10 K. The results are shown in Table 6.2.

6.1.3 Results

Except for the binary model, all models favour rather inclined orientations of $\phi \approx 60^\circ$ and $\psi \approx 130^\circ$, although they show a considerable scatter concerning the angular size. However, the latter is probably simply due to the different geometric shapes of the models, the value for θ having a slightly different meaning in each case. The ring model yields the lowest value of χ_r^2 by far. Its brightness distribution and visibility are shown in Figure

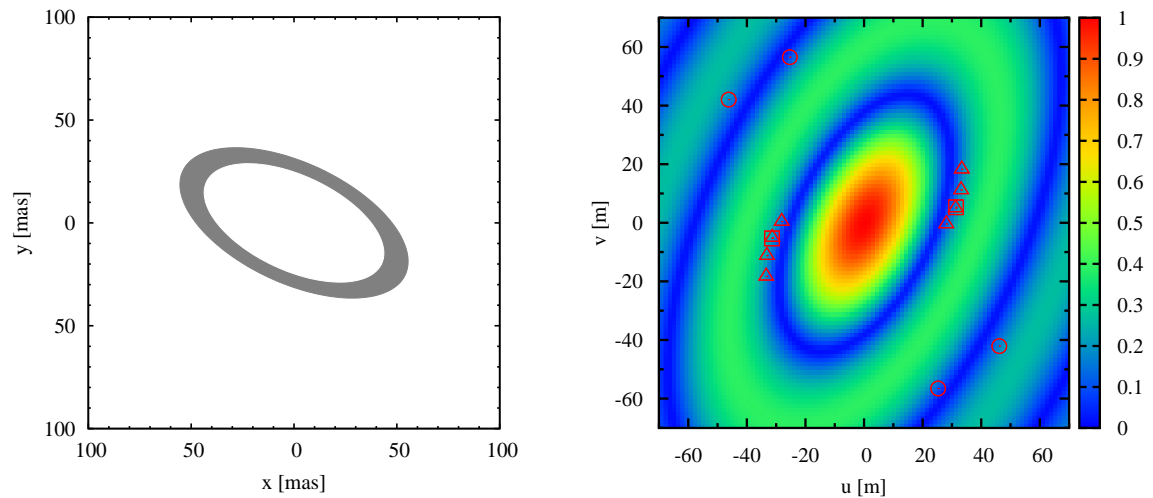


Figure 6.1: The brightness distribution and the corresponding visibility of the ring model with $\theta = 47$ mas, $\phi = 60^\circ$ and $\psi = 115^\circ$. The sampled points of the u - v -plane are also shown (see Figure 4.5).

6.1. Since the visibility is the Fourier transform of the brightness distribution, the two are oriented perpendicular to each other.

As noted above, we probed all angular separations between 1 mas and 1000 mas for the binary, but none of these values resulted in a good fit to the data. The χ_r^2 value of 87 is clearly offset from the other models, and the rather large separation of almost 0.5 as together with the brightness ratio of 1 would also have been detected in the acquisition images or the image from the aperture masking observations. Therefore, we can rule out a binary model for the brightness distribution of IRS 9A down to a brightness ratio of 0.1 and the angular scales probed by MIDI.

Irrespective of the precise structure of the unresolved region, we can use the values of the remaining four models to give an estimate of its size. For the given wavelength of $\lambda = 7.98 \mu\text{m}$ and a distance of 7 kpc this leads to the following values: 144 AU for the diameter of the inner rim of the accretion disk, 329 AU for the inner diameter of the the ring, 478 AU for the FWHM of the Gaussian and 521 AU for the diameter of the uniform disk. Since all models have a significant inclination of about 60° , these values correspond to the size of the major axis. Hence, due to the different geometric shapes, it is not possible to give a single characteristic size of the emitting region. If we use the values from our best-fit ring model, the values of the major axis are $\theta_{\text{in}} = 47$ mas (329 AU) and $\theta_{\text{out}} = \theta_{\text{in}} \times (1 + f) \approx 60$ mas (420 AU). The values for the minor axis are a factor of $\cos(\phi) = \cos(60^\circ) = 0.5$ smaller.

6.2 Radiative transfer models

We now start our analysis of both the visibilities and the SED by using two different radiative transfer models. The main difference between them lies in the fact that DUSTY can

only handle one-dimensional geometries (spherical or plane-parallel) for the gas and dust, while MC3D is able to work with arbitrary, three-dimensional distributions. DUSTY calculates the radiation field and temperature distribution of the dust by integrating an equation for the spectral energy density and the simple geometries allow fast, approximate analytical solutions. As the name already suggests, MC3D uses Monte Carlo methods to calculate the same quantities for three-dimensional geometries, which allows for asymmetrical density distributions or combinations of different components. However, if a moderately high accuracy is required, the calculations are very time-consuming.

We searched for suitable models with both DUSTY and MC3D by comparing the visibilities of the models with the ones we observed and calculating the corresponding χ_r^2 . Only after that did we examine the SED of the models and attempt to tune the input parameters so as to achieve a reasonable fit to both the visibilities and the SED, with the main focus still being on the visibilities. This is contrary to the approach of trying to achieve a good fit to the SED and then comparing these models with the visibilities (e.g. Leinert et al. 2004). We used the visibilities obtained with MIA (see Figure 4.6) for the comparison with the models and the calculation of χ_r^2 was conducted with the OYSTER software. Although we show the visibility V rather than V^2 throughout this work, most of the software dealing with interferometric data uses V^2 for their internal calculations since this is the quantity that is actually measured by the interferometer. This is also the case for OYSTER and should be kept in mind when comparing the visibility curves and the corresponding values for χ_r^2 in the subsequent chapters.

We note at this point that we make use of the steady-state approximation in all our radiative transfer models. The consequences of this approach are discussed in Chapter 7.

6.2.1 DUSTY

The radiative transfer code DUSTY is described in the user manual (Ivezić et al. 1999) and the theory behind the code is detailed in Ivezić & Elitzur (1997, 1999). DUSTY solves the problem of radiation transport for one-dimensional geometries, for example envelopes of gas and dust around stars. It produces radial profiles of the simulation parameters such as the bolometric flux, aspect ratios of the shell sizes, temperatures, etc. and also calculates the emerging SED, maps of the surface brightness and wavelength-dependent visibilities. However, we used the maps of the surface brightness in order to calculate the visibilities in the same way as we did for MC3D.

DUSTY utilises the scaling properties of radiatively heated dust (Rowan-Robinson 1980) which reduce the number of independent input parameters of the model. If the inner boundary of the spherical envelope is determined by dust sublimation, the spectral shape is the only important property of the heating radiation and the absolute luminosity is irrelevant for the problem. Likewise, the absolute values of the densities and distances of the dusty envelope are not important: it is fully characterised by the aspect ratios of its individual shells and the overall optical depth. Therefore, DUSTY cannot determine absolute values of the luminosity, the sizes and the visibilities on its own. Since these val-

ues are, of course, of great importance in the modelling process, they have to be inferred by external constraints. The radius where the temperature is equal to the dust sublimation temperature, for example, is specified in DUSTY's output for a luminosity of $L = 10^4 L_\odot$. It scales in proportion to $L^{1/2}$ and thus, if the luminosity of the central source has been measured, the absolute value of the inner radius of the envelope can be determined. Together with the aspect ratio of the shell this also fixes the overall size of the dust envelope.

Needless to say, it is highly unlikely that the circumstellar material of IRS 9A or other massive young stellar objects (MYSOs) is distributed in a spherically symmetric way. Rather, it will likely be arranged in circumstellar disks, bipolar cavities, jets, etc. Nevertheless, we consider it useful to test if such simple geometric shapes can already account for the general shape of the SED and the visibilities before introducing models which contain more free parameters, such as MC3D.

6.2.1.1 Parameters

Despite the simple geometry and the use of scaling relations, there are a number of input parameters that have to be specified. These are the spectral shape of the central object, dust properties such as the chemical composition and the size of the grains, the dust temperature at the inner boundary of the dust shell (T_1), the relative thickness (Y) and density distribution of the shell (η), the optical depth specified at some reference wavelength (τ_0) and the desired numerical accuracy of the calculations. We used small routines written in C++ and IDL in order to conduct a grid search for suitable parameters.

In the course of this grid search, we always kept three of the aforementioned parameters fixed. These are the spectral shape of the central object, the dust temperature at the inner boundary and the accuracy of the calculations. Assuming the central source to be a point source, DUSTY offers the possibility to conveniently define its spectral shape by specifying the temperature of a black body. Following Nürnbergger (2003), we use $T = 22000$ K for IRS 9A (see also Table 1.3). The temperature at the inner boundary of the envelope determines the dust sublimation temperature and for most of our models we adopt the common value of 1500 K. We never changed the accuracy of DUSTY's calculations from the recommended value of 5%. We now briefly describe the parameters that we varied in order to find a suitable model for IRS 9A.

Concerning the chemical composition of the dust, DUSTY offers six common grain types and the user simply has to specify their fractional abundances. We always used silicates and graphite grains from Draine & Lee (1984) and tested both the typical ISM ratio between graphites and silicates of 0.88 as well as mixtures from almost pure silicate to almost pure graphite. The size distribution of the grains is usually controlled by the MRN power law (Mathis et al. 1977), where the number of grains with radius a , $n(a)$, is given by:

$$n(a) \propto a^{-q}, \quad \text{for } a_{\min} \leq a \leq a_{\max}. \quad (6.3)$$

The standard parameters for the diffuse ISM are $q = 3.5$, $a_{\min} = 0.005 \mu\text{m}$ and $a_{\max} =$

		Dust		
Central object	Chemistry (DL)		Size distribution (MRN, $q = 3.5$)	
Black body $T_{\text{bb}} = 22000 \text{ K}$	Mix of silicates and graphite grains	sil.: 5–95 % gra.: 95–5 %	$0.005 \mu\text{m} \leq a_{\text{min}} \leq 0.5 \mu\text{m}$ $0.25 \mu\text{m} \leq a_{\text{max}} \leq 25 \mu\text{m}$	
		T_1	Y	p
		$\tau_0 (\lambda = 10 \mu\text{m})$	Num. acc.	
		1500 K	1000	$-2 \leq p \leq 2$
		$10^{-6} \leq \tau_0 \leq 10^0$	5%	

Table 6.3: Overview of the parameters of our grid search with DUSTY. Note that negative values for p imply that the density rises with radius since $\eta(y) = y^{-p} \propto r^{-p}$. Not all of the possible combinations of these parameters have been tested (see text).

$0.25 \mu\text{m}$. We slightly varied the lower and upper cutoffs in order to examine their effect on the visibilities and the SED, but the exponent q was always kept fixed.

The inner radius of the dusty envelope, r_{in} , is determined by the dust sublimation temperature. We always set the relative thickness Y of the shell to 1000 and defined the density distribution η via a simple power law. DUSTY normalises the density distribution and describes it in terms of the scaled radius $y = r/r_{\text{in}}$. Hence the power law can be written as:

$$\eta(y) = y^{-p}, \quad \text{with } 1 \leq y \leq Y, \quad \text{and} \quad \int \eta(y) dy = 1. \quad (6.4)$$

This power law can have more than one exponent, that is, the density distribution can be described via a piecewise power law. We tested models with both multiple exponents, simulating two concentric dust shells, as well as models with single exponents. In the case of the concentric dust shells, the density first dropped steeply before rising again to about half a percent of the density at the inner rim between $y = 200$ and $y = 500$. The optical depth τ_0 was always specified for a reference wavelength of $10 \mu\text{m}$. All parameters are summarised in Table 6.3.

We stress that we did not cover the full range of all the aforementioned parameters in one single grid search. Assuming a reasonably fine grid this would have exceeded our computational resources and simply have taken too much time. We rather examined the effect of individual parameters first, then started with coarse grids and subsequently narrowed the parameter ranges towards better and better models. For example, in the case of the models that were specifically adjusted to match the data from MIDI (see next chapter), we did not vary the chemical composition but rather assumed the standard ISM ratio between graphites and silicates of 0.88. Therefore, it is quite possible that a better fit to our data is possible within the given range of parameters.

6.2.1.2 Results

During the analysis of our models we noticed another problem which is connected to the rather strange shape of our measured visibilities. When searching for suitable models by

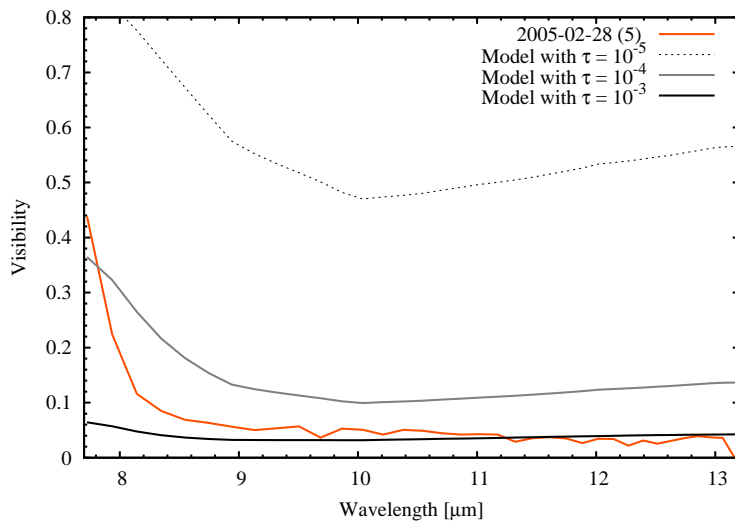


Figure 6.2: Comparison of one of our measured visibilities with three models that only differ in their optical depth. Starting with the lowest optical depth, the χ_r^2 values of the models are 37154, 112 and 6.7, respectively. All models have a mixture of 45 % silicates, 55 % graphite grains, $a_{\min} = 0.005 \mu\text{m}$, $a_{\max} = 0.25 \mu\text{m}$ and $p = 1.5$.

comparing their values of χ_r^2 , it turns out that models with completely resolved emission throughout the N band yield quite “competitive” values. If, in a specific grid search, the model with the lowest value of χ_r^2 is such a “zero-model”, this does not necessarily mean that a suitable model cannot be found within the given set of parameters. This is illustrated in Figure 6.2, where we show the effect of the optical depth on the visibilities. As indicated in the caption, the model which is almost completely resolved at all wavelengths, the “zero-model”, yields the best χ_r^2 by far. However, it does not reproduce the rising visibility for wavelengths below $9 \mu\text{m}$ and a better fit would probably have been obtained for an optical depth somewhere in-between 10^{-4} and 10^{-3} (although the slope is a bit too shallow in any case). Hence, if the “best model” of a specific grid search turned out to be a rather poor fit to the data, we always checked the models with similar parameters and a (slightly) worse χ_r^2 . These are also a good starting point for a subsequent grid search with a narrower range of parameters.

The results of our modelling efforts with DUSTY can be summarised as follows. Within the given range of parameters from Table 6.3 and the limitations outlined above, we find it impossible to construct a model that can account for all our data, even allowing for large deviations in individual cases. Such a “perfect” model would be able to simultaneously explain both sets of visibilities (MIDI and Gemini) and the SED of IRS 9A. Yet fitting an arbitrary combination of two of these three data sets is already a serious problem. Thus, we do find models that, for example, can reproduce the MIDI visibilities reasonably well, but the SED of these models is a very poor fit to the observed one. Furthermore, the visibilities of these models are not compatible with the ones from the Gemini South Observatory. These visibilities, on the other hand, can be reproduced quite easily with a different set of models, but they also have problems to account for the SED of IRS 9A. The parameters of these two classes of models do not have much in common, and, consequently, when using the models that can reproduce the data from Gemini to calculate the visibilities from MIDI, they also give a very poor result.

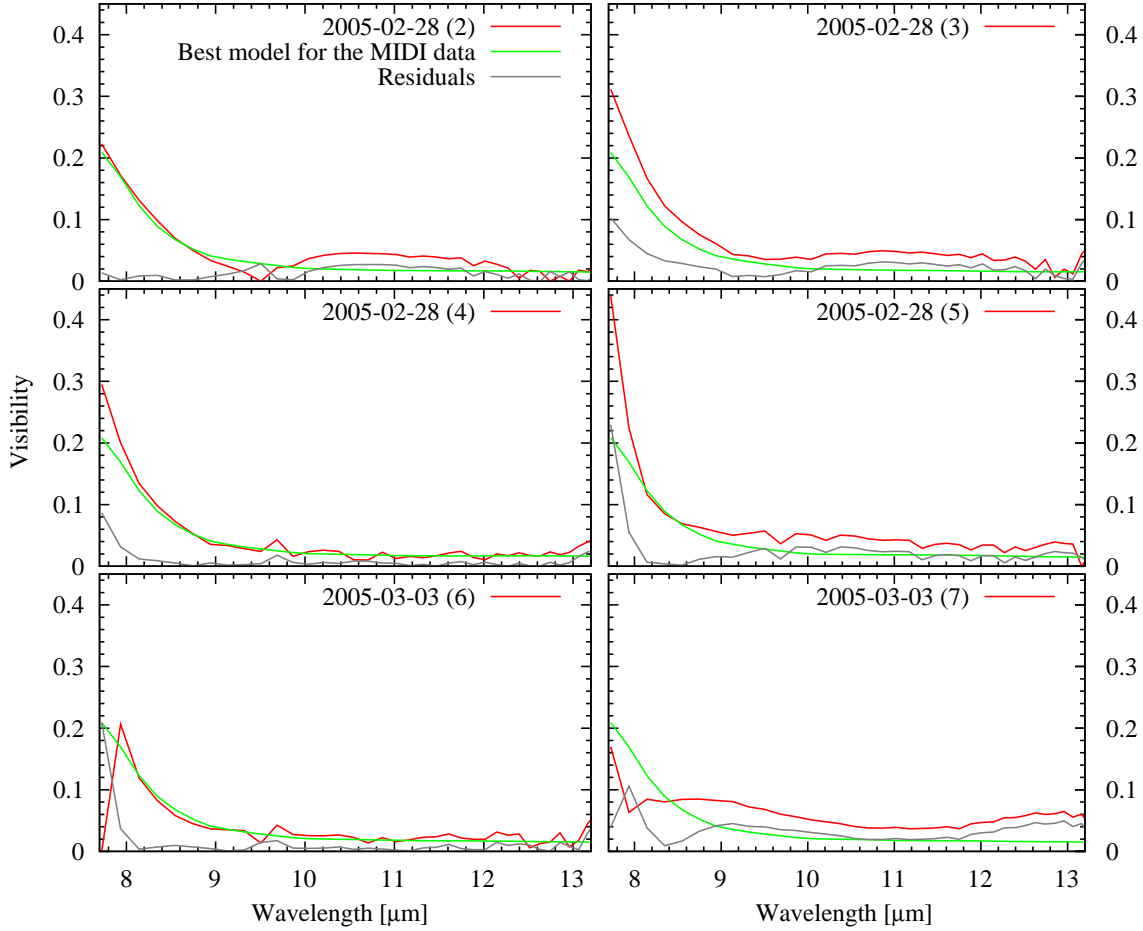


Figure 6.3: Comparison of six of our seven visibilities from MIDI with our best model from DUSTY. This model has $T_{\text{bb}} = 22000$ K, 53.2 % silicates, 46.8 % graphite grains, standard MRN, $T_1 = 1500$ K, $Y = 1000$, $p = -0.8$ and $\tau_0 = 0.1$. The inner radius is calculated to be about 100 AU, and so the apparent size of the inner diameter is ≈ 28.6 mas.

The SED itself poses another problem, which is connected to the fact that we do not detect a silicate feature in our spectra of IRS 9A either in absorption or emission. DUSTY always produces SEDs which contain this feature. Even if, by chance, the optical depth has a value that leads to an almost perfect cancellation of the emission and the absorption, there are still remnants in the form of quite strong, wing-like oscillations.

We now show the best models for the individual data sets to illustrate the problems outlined above. The plots that show the visibilities always have the same design, namely the observed data are shown in red, the models in green and the absolute value of their difference is shown in grey. The numbers of the individual measurements refer to the nomenclature that was used in the figures throughout Section 4.4. Starting with the best model for the visibilities from MIDI, henceforth called the “MIDI model”, Figure 6.3 shows six of our seven measurements with MIDI and the visibilities of the model for

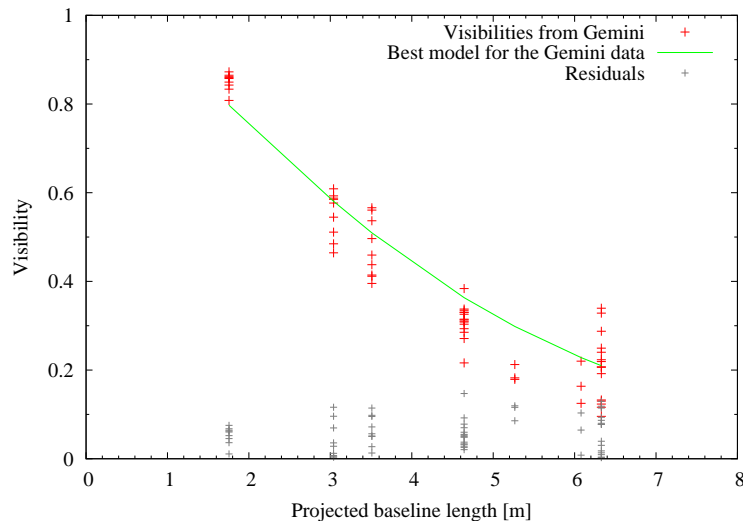


Figure 6.4: Comparison of the visibilities from the aperture masking data with our best model from DUSTY. This model has $T_{\text{bb}} = 22000$ K, 100 % silicates, standard MRN, $T_1 = 900$ K, $Y = 1000$, $p = 2$ and $\tau_0 = 10$, leading to an inner radius of about 490 AU and an apparent inner diameter of ≈ 140 mas.

the corresponding u - v -coordinates. We do not show the first measurement (27 February) because its u - v -coordinates are nearly identical to the ones from the fourth measurement. The model is able to reproduce the general trend of the observed visibilities, although the slope is almost identical in all cases which does not lead to a particularly good fit in the case of the third, fifth and seventh measurement. Averaged over all six measurements, this model has $\chi_r^2 = 6.45$, whereas the best fit has $\chi_r^2 = 0.4$ (no. 1) and the worst fit has $\chi_r^2 = 16.34$ (no. 6).

The parameters of this model are listed in the caption and we want to point out the unusual value of the parameter p . This model and also the models with similarly low values of χ_r^2 all have $p \approx -1$ which leads to $\rho(r) \propto r$. Such a steep, positive gradient for the density structure is rather unexpected for the dust distribution around a YSO and lacks a physical explanation. In the recent paper by de Wit et al. (2007), the authors analyse MIDI observations of the forming massive star W33A. They also come to the conclusion that models with steep, negative gradients for the density do not lead to reasonable fits to their visibilities, but they do find suitable models with $\rho(r) \propto r^{-0.5}$ after significantly reducing the assumed values of W33A’s luminosity and effective temperature. However, these models also do not lead to a good fit to the SED and the authors did not (yet) attempt a two-dimensional approach.

The best model for the visibilities from the Gemini South Observatory, the “Gemini model”, is shown in Figure 6.4. Note that although the visibility of this model is shown with a line in order to improve the visualisation, it is actually only calculated at the seven u - v -radii of the Gemini visibilities. The model cannot produce different visibilities for different position angles due to its spherical symmetry. For this reason it cannot account for the scatter of the Gemini data at each of the seven u - v -radii. The main differences between this model and the MIDI model lie in the chemical composition, the temperature at the inner boundary, the density distribution and the optical depth. We did not conduct a grid search for the Gemini model since our initial parameters already led to results that

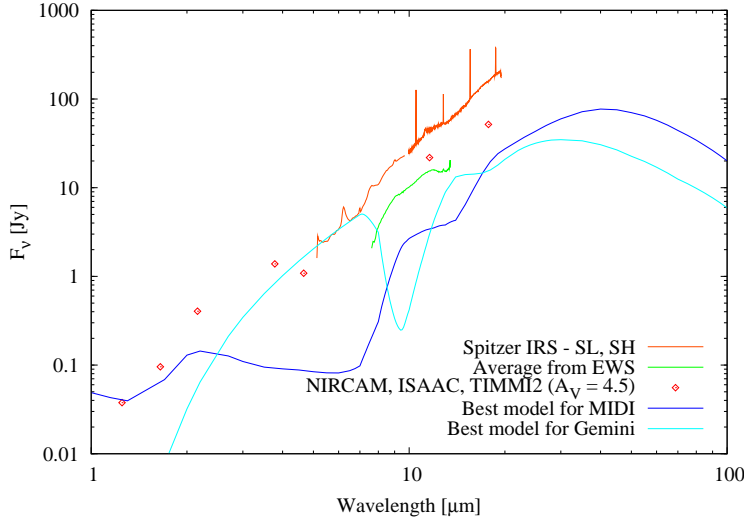


Figure 6.5: The SEDs from the MIDI and Gemini models compared to the observations.

are quite similar to the ones shown in Figure 6.4. Hence models with parameters that are closer to the ones from the MIDI model might exist, but as we will see below, the MIDI model itself is utterly inappropriate for the aperture masking data.

Figure 6.5 shows the SEDs of the MIDI and Gemini models in comparison to the spectrum from Spitzer and the spectrum from MIDI. We also show the single measurements from Table 1.3 in Section 1.3.2, but note that one would have to convolve the SEDs of the models with the transmission curves of the filters in order to make a meaningful comparison between the two. However, it is immediately obvious that both models cannot reproduce the observed SED and so we did not carry out these calculations. The overall near- and mid-infrared flux of the MIDI model is far too small, although the difference between the observed spectrum and the MIDI model is only a factor of four or five. The latter is due to the broad silicate emission feature of this model. The Gemini model can actually account for the observed Spitzer flux from about $5 \mu\text{m}$ to $7 \mu\text{m}$, but apart from that it also suffers from insufficient flux and a huge silicate absorption feature that is caused by the large optical depth of $\tau_0 = 10$.

As noted earlier, our primary goal is to construct a model that can account for the measured visibilities. We did not try to find a set of parameters that leads to a proper reproduction of the SED. Therefore, it is quite likely that such a set of parameters exists, but based on our results and experience with the models from DUSTY, we estimate the probability that the corresponding model can also reproduce the visibilities to be very low. In any case, the task of constructing a suitable SED will be hindered by the problem with the silicate feature outlined above.

Before concluding this chapter, we quickly show the results of the MIDI model applied to the data from Gemini as well as the Gemini model applied to the data from MIDI. Figure 6.6 illustrates that both models are not able to reproduce the visibilities of the particular dataset. We only show one visibility from MIDI since the results of the individual observations all look very similar, that is, the model visibilities are all very close to zero

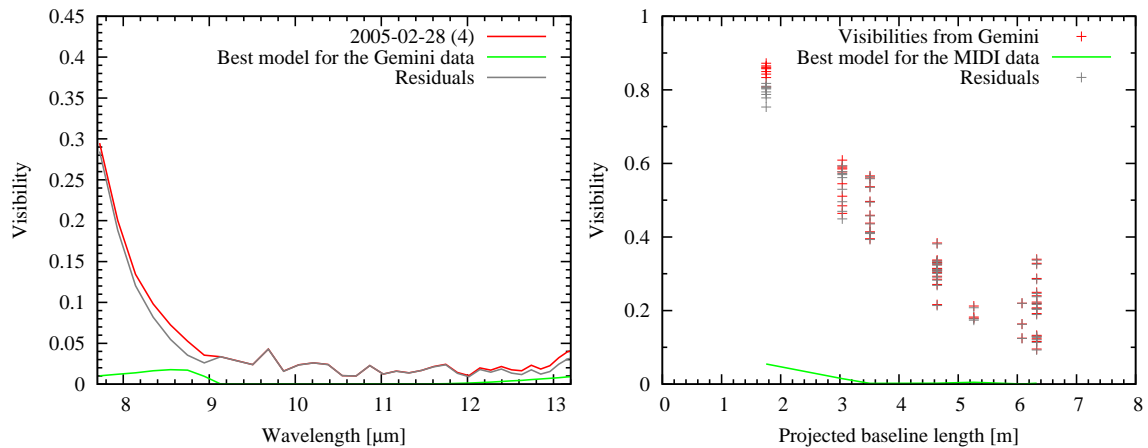


Figure 6.6: The left plot shows the fourth observation of MIDI and the corresponding visibility from the Gemini model. The right plot shows the data from Gemini and the corresponding visibilities from the MIDI model. Both models yield very poor results in these cases.

throughout the N band. The apparent size of the MIDI model is large enough to be almost completely resolved on projected baselines of only about 2 m.

In conclusion, we are not able to construct a single model that can account for all our observational data, indicating a more asymmetric structure of the material in IRS 9A's surroundings or invalid assumptions concerning the (fixed) parameters of our grid search. In order to decide between these two alternatives, we make use of the capabilities of MC3D in the next chapter.

6.2.2 MC3D

The radiative transfer code MC3D is described in Wolf et al. (1999) and Wolf (2003). It solves the radiative transfer problem for arbitrary dust configurations surrounding one or more stars by using the Monte Carlo method. A detailed account of the solution of the radiative transfer problem in this code can be found in Fischer et al. (1994). MC3D computes the dust temperature of the circumstellar material, the SED, maps of the intensity and of the polarisation of light and hence is an ideal tool to model the dusty environments of young stars. The big advantage compared to DUSTY is, of course, that the calculations are fully three-dimensional, which allows for much more complex gas and dust geometries such as, for example, an accretion disk combined with an outer shell. Moreover, the calculations do not make use of any simplifying assumptions. The disadvantages are a larger set of free parameters and a significantly higher computational demand. The last point is due to the fact that the random error of the results is roughly proportional to the inverse of the square root of the number of simulated photons. Thus, in order to achieve a reasonably low level of statistical noise, a large number of photons has to be used. This is especially true in the case of large optical depths.

The algorithm can be divided into a small number of steps that solve the radiative transfer problem iteratively. First, the model space is divided into so-called *energy storage cells*, small volumes that can absorb and emit radiation, in order to obtain a spatially resolved dust temperature distribution. Here, several aspects have to be taken into account concerning an optimal splitting of the model space (see Wolf et al. 1999). In the second step, the initial temperature of each of these cells is calculated by taking the total absorbed flux from the central star(s) into account. This step does not yet consider the dust re-emission of the cells. The dust re-emission is evaluated in the third step and, since it is carried out for each cell separately, this step is repeated until the following two conditions are met. On the one hand, after the dust re-emission of one of the cells has been calculated, the maximum change of the temperature of all of the other cells always has to be smaller than a given limit (usually a few Kelvin). On the other hand, the code checks for energy conservation by calculating the sum of the luminosities of the central star(s) and the dust shell as they appear from outside of the model space. This luminosity has to match the original luminosity of the central star(s) to better than 0.1 %.

As described in Wolf (2003), MC3D is also capable of calculating images and SEDs via ray tracing. This approach is much faster than the “real” radiative transfer, but will only lead to correct results if scattering processes are negligible. Since this is the case for mid-infrared wavelengths, we always used ray tracing to calculate our images and SEDs.

6.2.2.1 Model geometry

Due to the unsatisfactory results from our previous modelling efforts and the general picture of (high-mass) star formation outlined in Sections 1.1 and 1.2, we use MC3D to test whether gas and dust distributions involving a circumstellar disk are able to explain our observations of IRS 9A. Just as in our approach with DUSTY, the main difficulty is to find a structure that can account for both the visibilities measured by MIDI and those measured by T-ReCS at Gemini South, i.e., the visibilities from low to high spatial frequencies. As we will see below, models involving a circumstellar disk can reproduce the MIDI data reasonably well, but a disk alone appears too compact at the resolution of Gemini South and hence produces visibilities that are too high. For this reason we embed the disk in a large shell that does not completely obscure the inner parts, but leads to partly resolved visibilities for baselines of only a few meters. This model can also account for the appearance of IRS 9A in single-dish observations, where it clearly does not appear as a point source.

The density structure of the disk which we use in our models is based on the approach described in Wood et al. (2002). Here, the authors use a two-dimensional, axisymmetric, flared disk that is additionally heated by stellar radiation. Flared disks were first described by Kenyon & Hartmann (1987) in order to explain the observed (high) disk temperatures of T Tauri stars that could not be reproduced by the flat, steady accretion disks from Lynden-Bell & Pringle (1974). Due to the fact that the scale height of a flared disk increases with radius, it can intercept more radiation from the central star than a flat

disk and, consequently, has a shallower radial temperature gradient and larger infrared excess (see also the short review by Wood 2008). However, in contrast to Wood et al. (2002), we make use of the general assumption that the reprocessed radiation from the star dominates the flux of the disk in the infrared. This might not be true for the inner parts of the disk, but due to the large distance to IRS 9A even the VLTI cannot resolve these regions. Therefore, we do not include any contributions from viscous heating.

The different effects of accreting and non-accreting disks, puffed-up inner rims and dusty envelopes on the observational appearance of RY Tau have been extensively discussed by Schegerer et al. (2008). One of their conclusions is that an actively accreting disk and a passive disk in combination with an envelope have the same effect on the SED and visibilities in the near- and mid-infrared. Hence, although an analysis considering accretion effects would certainly be interesting in its own right, we see two reasons to favour the approach with a passive disk and a spherical envelope. First, owing to the appearance of IRS 9A in low-resolution observations, we need to incorporate a large structure that surrounds the central regions and radiates in the mid-infrared. Second, the number of free parameters should be as small as possible in order not to overdetermine the models. The dusty envelope is the simplest solution for both issues, adding only one more free parameter.

6.2.2.2 Parameters

The number of parameters required for a full simulation with MC3D is quite large and we will only list and explain the ones that are immediately connected to the relevant physical parameters of the models. We start with the accretion disk whose density distribution is controlled by the three parameters a , b and h_{100} . The radial dependence of the density is governed by a , b is the so-called *flaring parameter* and h_{100} is the scale height at a radius of 100 AU. Using cylindrical coordinates $r = \sqrt{x^2 + y^2}$ and z (ϕ is irrelevant due to azimuthal symmetry), the equation for the density can be written as:

$$\rho(r, z) = \rho_0 \left(\frac{R_\star}{r} \right)^a \exp \left[-\frac{1}{2} \left(\frac{z}{h(r)} \right)^2 \right], \quad (6.5)$$

where ρ_0 is used to scale the density distribution so that the total mass of the dust adds up to a previously specified value. The scale height is given by $h = h_{100}(r/R_\star)^b$, that is, it increases with radius and b . Due to hydrodynamical considerations, a and b are connected via the relation $a = 3(b - 1/2)$ (see, e.g., Schegerer et al. 2009).

The dust shell around this disk is calculated using one more free parameter which we call d_s . It is used to define the radius \vec{r} (now in three dimensions) beyond which the density distribution is spherical and falls off in proportion to $|\vec{r}|^{-a}$. We thus write for the density of the shell:

$$\rho(|\vec{r}|) = \rho_0 e^{-1/2} \left(\frac{R_\star}{|\vec{r}|} \right)^a, \quad \text{if } |\vec{r}| > \frac{R_{\text{out}}}{d_s}, \quad (6.6)$$

General model parameters	Parameters of the disk / shell	
	Disk	Disk + shell
$R_{\text{in}} = 10 - 120$ [AU]	$a = 2.1$	$a = 0.9, 1.5, 2.1$
$R_{\text{out}} = 1000, 2000, 4000$ [AU]	$b = 1.2$	$b = 0.8, 1.0, 1.2$
$T_{\text{eff}} = 22000, 32000$ [K]		$d_s = 1.01 - 3.4$
$L_{\text{tot}} = 180000, 270000$ [L_{\odot}]	$h_{100} = 3, 9, 15$ [AU]	$h_{100} = 3, 9$ [AU]
$T_{\text{sub}} = 1500$ [K]	$m_{\text{dust}} = 0.01 - 1.0$ [M_{\odot}]	$m_{\text{dust}} = 0.01 - 0.03$ [M_{\odot}]
	$\theta = 0 - 86$ [$^{\circ}$]	$\theta = 72 - 86$ [$^{\circ}$]
	PA = 0 - 180 [$^{\circ}$]	PA = 0 - 180 [$^{\circ}$]

Table 6.4: Overview of the parameters of our grid search with MC3D. The individual values are either given explicitly or restricted to a certain range. In the latter case we usually divided the range into about 4–6 single values first and then improved these initial values based on the results of the simulations.

where R_{out} is the outer radius of the model space and $d_s > 1$. The factor $e^{-1/2}$ ensures that the density at the inner rim of the shell equals the density of the disk at one scale height and $r = R_{\text{out}}/d_s$.

Table 6.4 gives an overview of the most important parameters, separated into the ones that are related to the general configuration of the simulation (inner and outer radii, stellar parameters, etc.) and the ones that affect the structure and appearance of the disk and/or shell. In contrast to DUSTY, the dust sublimation temperature T_{sub} is not used to calculate the radius of the inner rim. This radius is fixed by the value R_{in} . Therefore, it is possible that the temperature in the innermost cells of MC3D exceeds the dust sublimation temperature. MC3D issues a warning in this case, indicating the number of affected cells. However, in most of these cases the affected cells contain very small amounts of dust and the effects on the overall results can be neglected. The position angle is, in fact, not a parameter of MC3D, but when calculating the values of χ_r^2 within OYSTER, we always took different orientations of the model into account by rotating the intensity maps for position angles from 0° to 180° .

During our grid search with MC3D we did not test all possible combinations of the parameters given in Table 6.4 as well. A single simulation with MC3D takes much more time than with DUSTY, especially if one wishes to compute a very accurate SED that also contains the contributions from the central star in the optical and ultraviolet range. Thus, the same limitation that we already mentioned at the end of Section 6.2.1.1 also holds true for our simulations with MC3D. A specific combination of the parameters in Table 6.4 might yield a better fit to our data, as well as, of course, an entirely different set of parameters.

6.2.2.3 Results I – Disk models

We start with the results of the models that are only composed of a circumstellar disk. We find two sets of parameters that lead to an adequate reproduction of the visibilities from

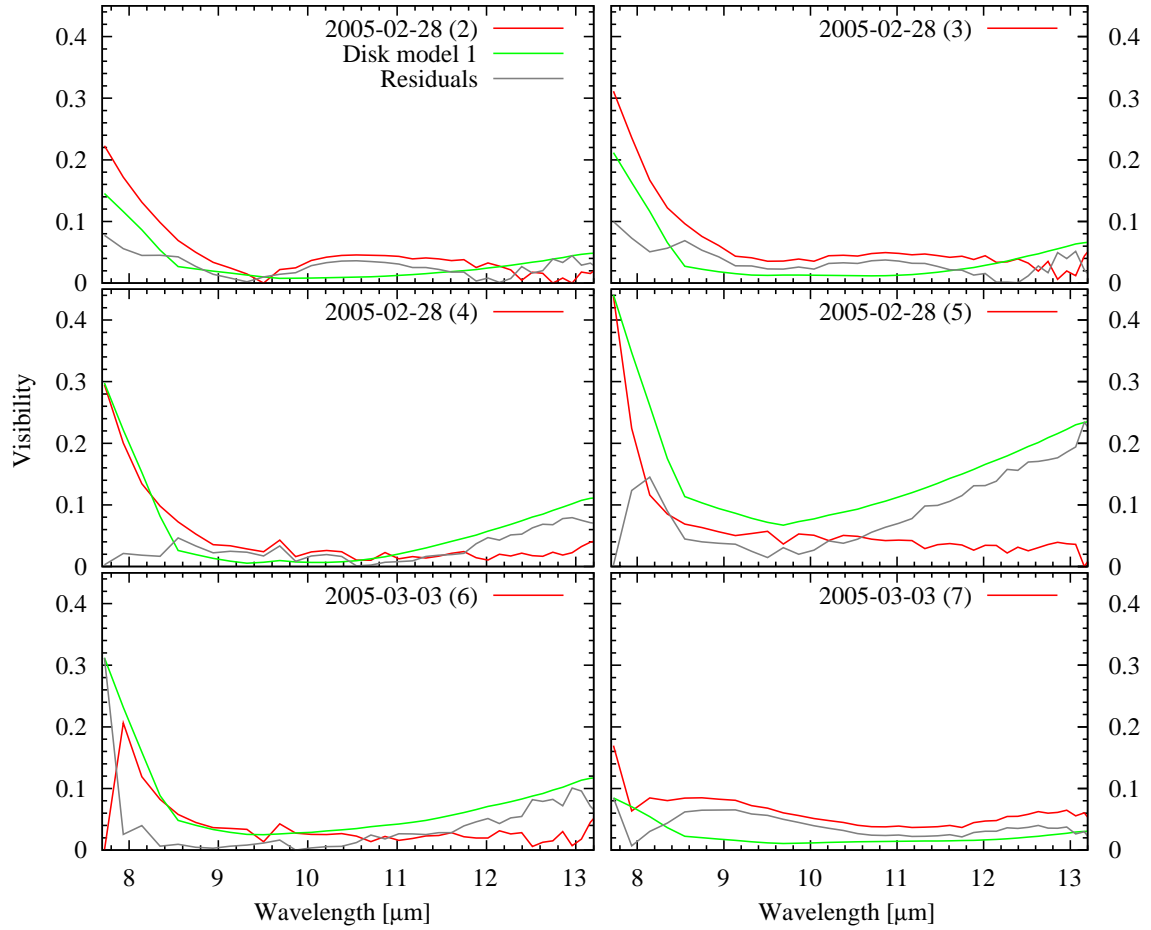


Figure 6.7: The visibilities of disk model 1 compared to the ones from MIDI. The parameters of this model are: $R_{\text{in}} = 110$ AU, $R_{\text{out}} = 2000$ AU, $T_{\text{eff}} = 22000$ K, $L_{\text{tot}} = 2.7 \times 10^5 L_{\odot}$, $a = 2.1$, $b = 1.2$, $h_{100} = 9$ AU, $m_{\text{dust}} = 0.03 M_{\odot}$, $\theta = 72^{\circ}$, PA = 118° .

MIDI. We will refer to these models as “disk model 1” and “disk model 2” or simply the first and the second model. Figure 6.7 shows the visibilities of disk model 1 compared to the observations of MIDI. The model is able to reproduce most of the measurements fairly well and, compared to the models from DUSTY, produces a much better fit to the steep slope of the visibility below $9 \mu\text{m}$. However, the visibilities of the model rise for wavelengths larger than about $10 \mu\text{m}$ or $11 \mu\text{m}$, which is especially evident for observation number five. This trend is visible in all other curves as well, yet on a smaller scale. The model also does not yield a particularly good fit to observation number seven, although the small change of the position angle between the sixth and the seventh observation from 132° to 156° leads to a significant change of the visibility (see discussion at the end of Section 4.4.3).

Figure 6.8 shows the same plot for disk model 2. The visibilities of this model are also quite close to the ones from MIDI, especially for observations number 2, 3 and 4.

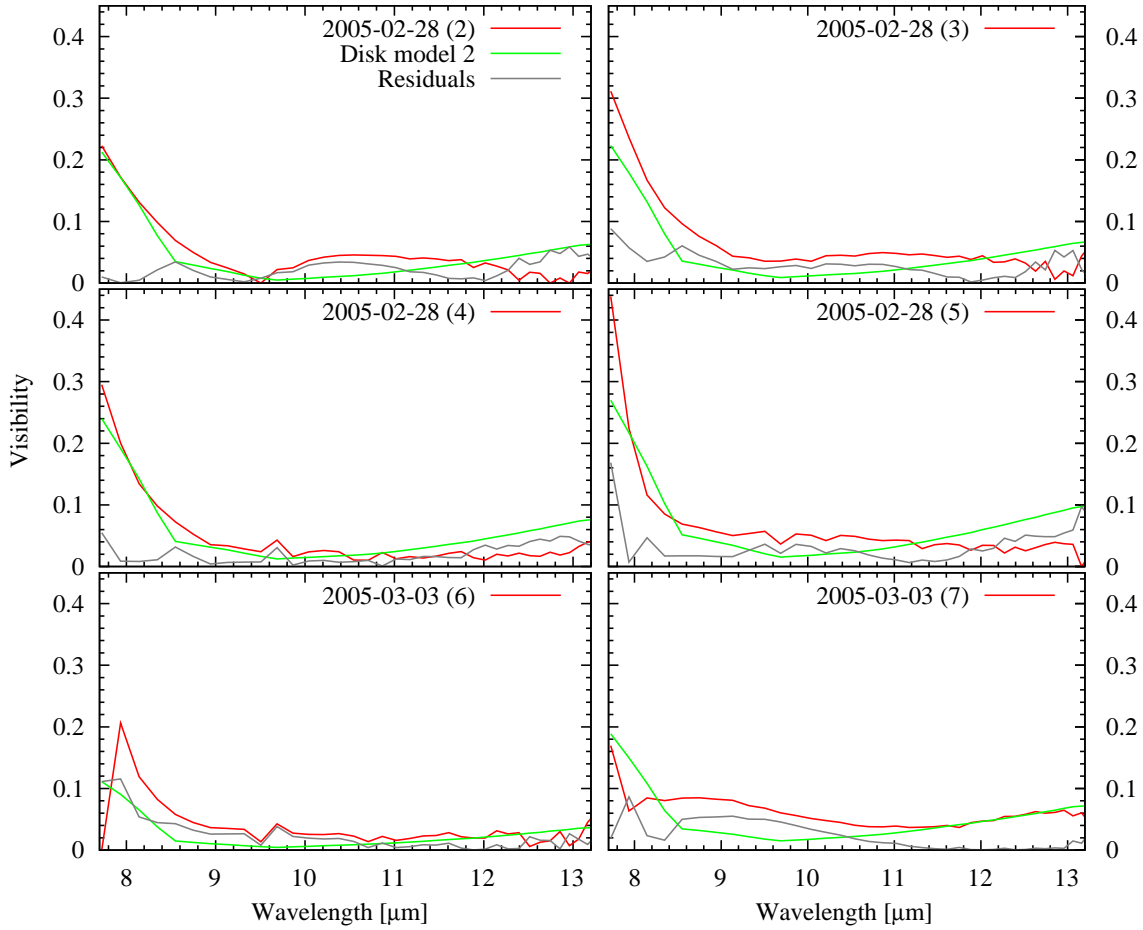


Figure 6.8: The visibilities of disk model 2 compared to the ones from MIDI. The parameters of this model are: $R_{\text{in}} = 20 \text{ AU}$, $R_{\text{out}} = 4000 \text{ AU}$, $T_{\text{eff}} = 22000 \text{ K}$, $L_{\text{tot}} = 2.7 \times 10^5 L_{\odot}$, $a = 2.1$, $b = 1.2$, $h_{100} = 15 \text{ AU}$, $m_{\text{dust}} = 0.16 M_{\odot}$, $\theta = 55^{\circ}$, $\text{PA} = 0^{\circ}$.

However, the fit to the sixth observation is slightly worse. The increase of the visibility for wavelengths larger than $10 \mu\text{m}$ is not as strong as for disk model 1, which leads to a better fit to observation number 5, but the agreement with the last observation is fairly similar again. Both models are not able to account for the slightly different shape of observation number seven.

The parameters of these two models differ in several important aspects. First, the inner and outer radii are not the same. The radial extent of the disk of the first model is much smaller, ranging from an inner radius of 110 AU to an outer radius of 2000 AU , whereas the second model already starts at 20 AU and reaches out to 4000 AU . Second, the disk of the first model is less massive and thick, featuring a total mass of the dust of $0.03 M_{\odot}$ and a scale height of 9 AU ($0.16 M_{\odot}$ and 15 AU for the second model). Finally, the inclinations and position angles differ. They are rather large for the first model, which is seen almost edge-on, while the second model is seen under a moderate inclination and

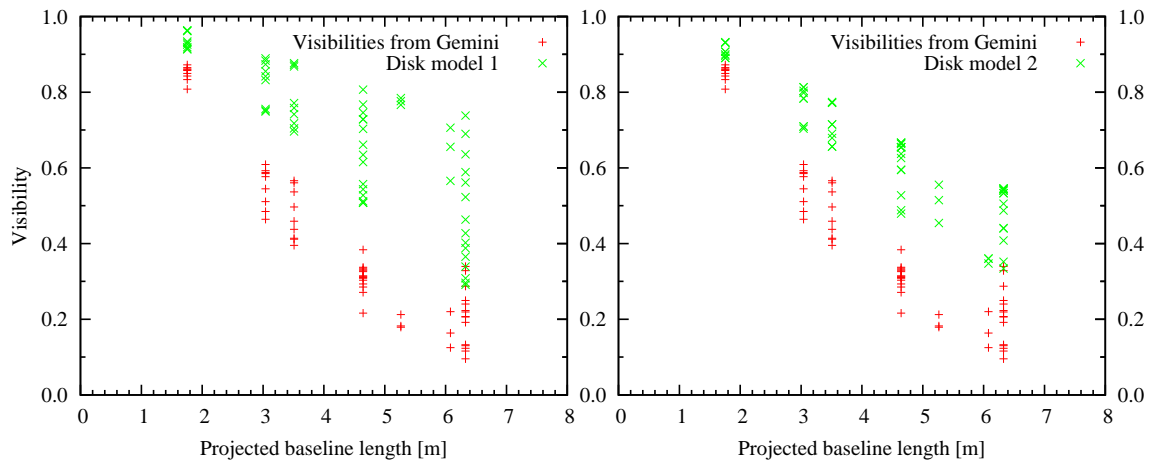


Figure 6.9: The two disk models compared to the visibilities from Gemini South. In order to avoid confusion due to too many points in the plot, we do not show the residuals as in the other figures.

with a position angle of zero. Since the disk of the first model is thinner, the central regions of the disks are visible in both cases, including parts of the inner rim. This is not surprising as they represent the smallest and hottest parts of the disk and are responsible for the rising visibilities at wavelengths below $9\ \mu\text{m}$.

We already mentioned that the emission from the disk alone cannot account for the visibilities at low spatial frequencies. This is demonstrated in Figure 6.9, showing disk model 1 and 2 applied to the u - v -coverage of the observations from Gemini South. Given that the models are not spherically symmetric, we do not obtain a line as in Figure 6.4, but the different position angles lead to different values of the visibilities. It is immediately obvious that the disk appears too compact in both cases, although the second model yields much better visibilities than the first model. This is due to the different sizes of the disks. The second disk model is not only larger in terms of the radial extent, but also has a larger scale height and is seen under an intermediate inclination. This leads to a much larger apparent size whereas disk model 1 is simply too small in order to be well resolved by Gemini South. Certainly, it would be rather easy to increase the physical size of the emitting region of the disk by changing its density structure, size or the inclination, but this would also change its appearance to MIDI. This led us to the idea of adding a spherical envelope to the model that leaves the appearance of the inner parts of the disk basically unchanged, but before we present the results of this approach in the next chapter, we compare the SEDs of the two disk models with the observations.

Figure 6.10 shows the spectra of disk model 1 and 2. They are very similar to each other, but the second model produces a larger mid- and far-infrared excess. The agreement between the models and the data is better than for the DUSTY models (see Figure 6.5), but the overall match is still quite poor. The slope of both SEDs is smaller than the observed one and they intersect with the data from Spitzer at wavelengths of about $11\ \mu\text{m}$ and $15\ \mu\text{m}$, respectively. At first, the flux of the models is larger than that measured by Spitzer,

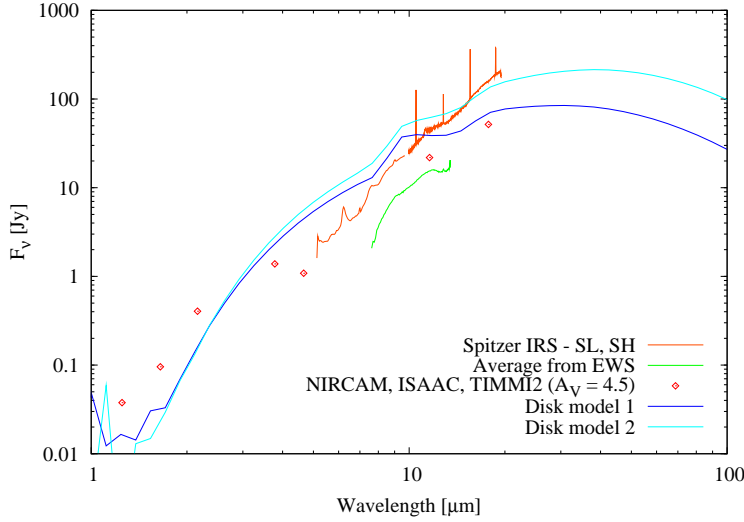


Figure 6.10: The SEDs of disk model 1 and 2 compared to the observations.

but for wavelengths that are larger than these values it is (slightly) lower. Both models show a rather faint silicate emission feature. The spiky shape of the curves that is visible at wavelengths below $2 \mu\text{m}$ is due to the Monte Carlo method. The (comparatively) strong extinction in this range requires a very high number of test photons in order to reduce the statistical noise. However, the calculation of these SEDs already takes more than one day in each case and we did not increase the number of test photons any further.

6.2.2.4 Results II – Disk + shell model

We now investigate whether we can improve our disk models by adding a spherical envelope to the density distribution. Ideally, this envelope will increase the apparent size of the emitting region on the spatial scales that are probed by the observations of Gemini South while at the same time not obscuring the inner regions that contain the disk. In order to achieve this goal, the optical depth of the spherical envelope has to be rather small and its diameter has to be larger than about 100 mas , i.e., the region investigated by MIDI (compare with Table 4.2). As it turns out, the envelope has to be very thin in order to be transparent enough. This is due to the definition of its density distribution in equation (6.6). We could, of course, use different values for a and ρ_0 , but this would introduce even more free parameters and the models should be as simple as possible.

We used the first disk model from the previous chapter as a starting point and calculated the visibilities and SEDs for different values of the shell parameter d_s (see Table 6.4). All values larger than about 1.1 lead to models that are completely resolved by MIDI because the envelope outshines and obscures the disk. We only obtain reasonable values for the visibilities if the inner radius of the envelope is larger than approximately $0.9 R_{\text{out}}$. When decreasing d_s to values smaller than 1.1, the disk becomes gradually visible again and the visibilities below $9 \mu\text{m}$ approach their “old” values without the envelope. We obtain the best agreement with the observational data for $d_s = 1.03$, that is, an inner radius

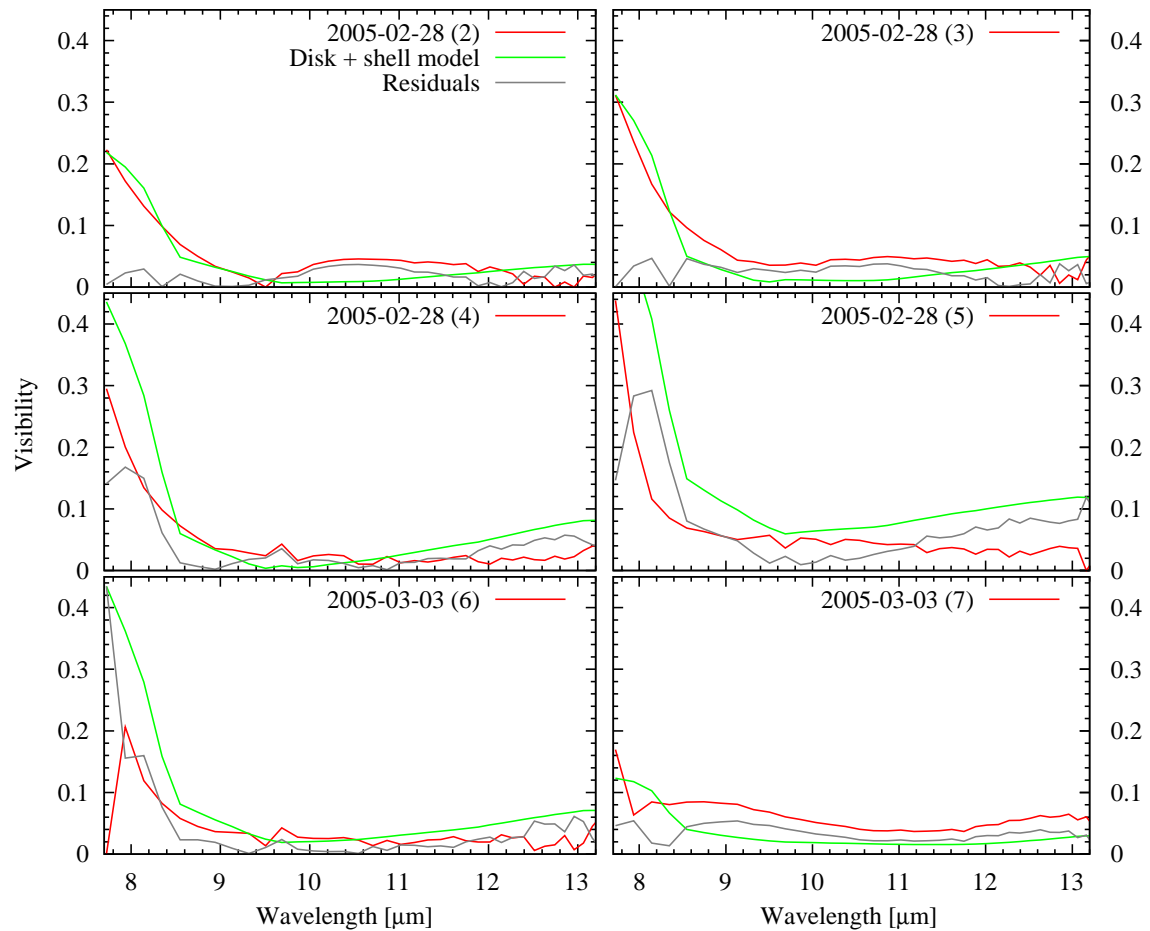


Figure 6.11: The visibilities of the disk+shell model with $d_s = 1.03$ and for $L_{\text{tot}} = 1.2 \times 10^5 L_{\odot}$. The remaining parameters are the same as for disk model 1, that is: $R_{\text{in}} = 110 \text{ AU}$, $R_{\text{out}} = 2000 \text{ AU}$, $T_{\text{eff}} = 22000 \text{ K}$, $a = 2.1$, $b = 1.2$, $h_{100} = 9 \text{ AU}$, $m_{\text{dust}} = 0.03 M_{\odot}$, $\theta = 72^\circ$, $\text{PA} = 118^\circ$.

of the envelope of about $0.97 R_{\text{out}}$. However, the flux of this model is too high and exceeds the value measured by Spitzer at all wavelengths. If we reduce the luminosity of the central source in order to correct for this, we run the risk of changing the visibilities as well, but we discovered that there are only minor changes to the visibilities while at the same time it is possible to achieve a good fit to the measured SED. We find the best agreement between the model and all datasets for $L_{\text{tot}} = 1.2 \times 10^5 L_{\odot}$. Thus, the model has the same parameters as disk model 1, except for the luminosity, and has the additional shell parameter $d_s = 1.03$. We refer to this model as the “disk+shell model”.

Figure 6.11 shows the visibilities of this model compared to those from MIDI. Obviously, the spherical envelope and the reduced luminosity of the central source lead to slight changes in the individual visibilities of the model, but the overall agreement with the data from MIDI stays more or less the same (compare with Figure 6.7). If we, for example, take a closer look at the fifth measurement, we see that the visibility from disk

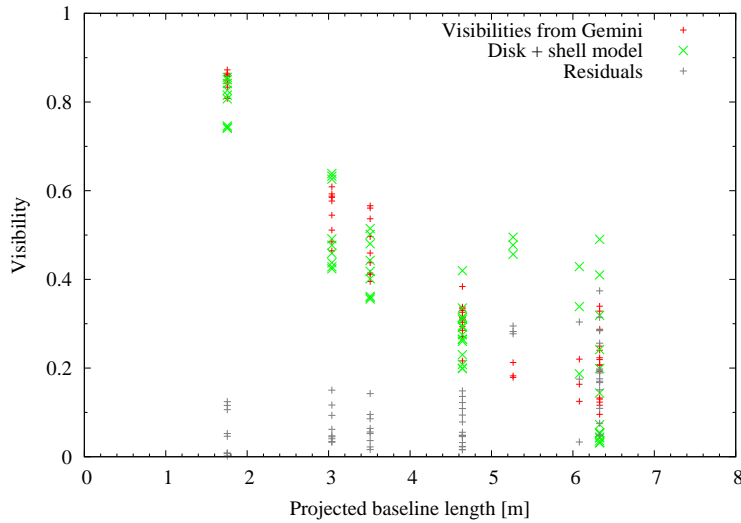


Figure 6.12: The disk + shell model compared to the visibilities from Gemini South.

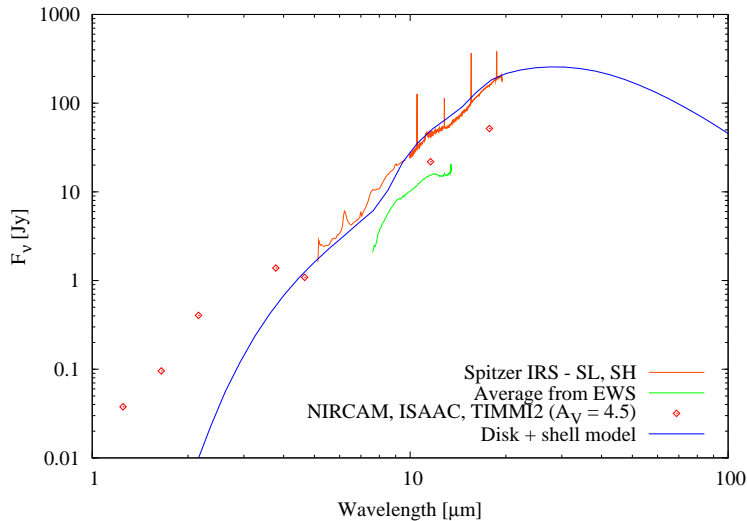


Figure 6.13: The SED of the disk + shell model in comparison to the observations.

model 1 yields a better fit to the data below $9 \mu\text{m}$, but the disk + shell model is better suited for wavelengths above $10 \mu\text{m}$. Thus, the shell neither leads to an improved fit to the MIDI data nor does it corrupt the results we have obtained so far. However, it significantly improves the visibilities corresponding to the u - v -coverage of Gemini South and improves the fit of the SED.

Figure 6.12 shows the visibilities of the disk + shell model compared to the ones from Gemini South. The agreement between the two is certainly not perfect, but much better than in all other models we have shown so far (see Figures 6.4, 6.6 and 6.9). The model can account for most of the measured features and leads to a particularly good reproduction of the four measurements at the smallest projected baselines. The only shortcomings are a slightly larger scatter at each of the projected baselines and the rather large deviations at 5.27 m and 6.08 m . However, these shortcomings have to be seen alongside the fact that this is also the first model that is able to account for both sets of visibilities.

Finally, we examine the SED of the disk + shell model which is shown in Figure 6.13. As it turns out, the spherical envelope significantly increases the slope of the SED which is now close to the one from Spitzer (compare with Figure 6.10). Together with the reduced luminosity of the central object, this produces an excellent fit to the SED from Spitzer throughout the mid-infrared. Furthermore, the model shows only a very weak silicate emission feature that is barely discernable in the plot. Hence the disk + shell model leads to an acceptable reproduction of all our observational data, ranging from visibilities that cover a large range of spatial frequencies to the mid-infrared spectrum. The comparison of this model SED with the (small aperture) spectrum from MIDI and the near- and mid-infrared data from Table 1.3 will be discussed in a forthcoming paper.

6.3 Fitting the spectra to a large grid of young stellar object SEDs

Due to the increasing number of near- and mid-infrared SEDs of YSOs that have been observed, a grid of 20000 YSO models has been computed by Robitaille et al. (2006). The idea behind the project is to facilitate the interpretation of observed spectra by providing an online fitting tool that compares a given dataset with the SEDs of the models, taking a wide range of parameters into account (see Robitaille et al. 2007). The website¹ of the project gives access to all models and their parameters as well as the SED fitting tool.

Within the framework of this project it is assumed that all stars form via accretion and the circumstellar geometry consists of a rotationally flattened, infalling envelope, bipolar cavities and a flared accretion disk. The models are axisymmetric and encompass a large range of (proto-) stellar masses and ages, ranging from $0.1 M_{\odot}$ to $50 M_{\odot}$ and from 10^3 yr to 10^7 yr, respectively, leading to evolutionary states from highly embedded sources to very low mass disks. The stellar atmospheres are taken from Brott & Hauschildt (2005) for temperatures below 10000 K and from Kurucz (1992) for temperatures above 10000 K. The properties of the central star are related to its age and mass via the evolutionary tracks of Bernasconi & Maeder (1996). In contrast to our approach with MC3D, the accretion luminosity of the disk is taken into account. The SEDs are calculated with a Monte Carlo radiation transfer code which, together with the geometry of the models, is described in detail in Whitney et al. (2003a,b).

For each model, the SED is calculated for 10 different viewing angles and 50 circular apertures, resulting in 10 million SEDs. The grid consists of 14 different parameters. Among them are the stellar mass, radius and temperature, the envelope and disk accretion rate, the disk mass and further parameters that mostly characterise the geometry of the system. The details are given in Robitaille et al. (2006). The SED fitting tool can deal with data that is given in common broad- or narrowband filters (e.g. 2MASS, IRAC, MIPS) or monochromatic flux measurements from spectral data. The user also has to specify the

¹<http://caravan.astro.wisc.edu/protostars/>

error of each measurement, the size of the aperture that was used to measure the flux, and a range of distances and interstellar extinctions towards the object. The online fitter then compares all model SEDs with the data, taking the values for the distance and interstellar extinction into account, and searches for the most appropriate SEDs by calculating the average value of χ^2 per data point (denoted by χ_{dp}^2 in the following). Of course, a broader range of wavelengths covered by the measurements will lead to fewer models that can reproduce the data.

We use this fitting tool to compare the model SEDs with our spectral data from MIDI and Spitzer. Both cover a rather narrow range of wavelengths and probe IRS 9A on different spatial scales. MIDI is inferior with respect to the wavelength range and spectral resolution, but superior in terms of spatial resolution. Since the fitting tool limits the number of data points to a maximum of 50, we have to restrict the MIDI and Spitzer data to specific wavelengths. In the case of MIDI we entered 50 flux values from about $7.8 \mu\text{m}$ to $13.1 \mu\text{m}$, resulting in $\Delta\lambda \approx 0.08 - 0.15 \mu\text{m}$. In the case of Spitzer we entered 28 values from $5.5 \mu\text{m}$ to $19 \mu\text{m}$, using $\Delta\lambda \approx 0.5 \mu\text{m}$. We excluded the strong emission lines; the value of the flux at $10.5 \mu\text{m}$ was obtained via a linear fit to the continuum on both sides of the [S IV] line.

The size of the apertures of MIDI and Spitzer are significantly different from each other. The width of the slit that is inserted in the intermediate focus of MIDI measures $0.52''$ on the sky, whereas the two slits of Spitzer's SL module and one slit of the SH module measure $3.6''$, $3.7''$ and $4.7''$, respectively (see the user manuals/guides of the instruments). Comparing these values with the apparent size of IRS 9A, for example Figures 4.2 and 5.1, we see that the width of MIDI's slit is similar to the size of the extended emission around IRS 9A, yet the bulk of the emission lies well inside the slit. The three different slits of Spitzer, on the other hand, are much larger than IRS 9A. According to the author T.P. Robitaille (priv. comm.), the values for the aperture radius do not have to be exact, but values in-between the half width of the slit and the half width of the region the spectrum was extracted from along the width should work fine. Therefore, we use a value of $0.3''$ for the aperture radius of MIDI and $3''$ for the aperture radius of Spitzer. We also tested slightly different values and as we will see below, the results do not change much. In either case we restrict the range of distances to $D = 6 - 8 \text{ kpc}$ and the interstellar extinction to $A_V = 4 - 5 \text{ mag}$ (see discussion in Section 1.3.1).

6.3.1 Spitzer

The page that shows the results of the fitting process displays a summary of the most important information. First of all, a plot shows the input data together with all the model SEDs that satisfy the relation $\chi_{\text{dp}}^2 - \chi_{\text{dp,best}}^2 < 3$. This plot gives an immediate impression of how well the data constrain the parameter space of the models. The plot should not show too many models, otherwise the significance of the results will be limited. Given the fact that the data from Spitzer only cover the range from $5.5 \mu\text{m}$ to $19 \mu\text{m}$, this plot does show a rather small number of models which, in addition, have quite similar SEDs.

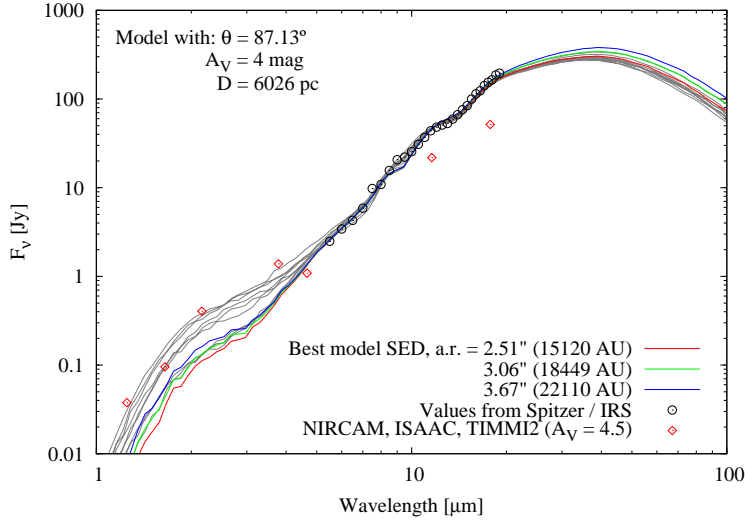


Figure 6.14: The top ten models of the YSO grid compared to the data from Spitzer. The three coloured curves all show the best model, but for different sizes of the aperture. The grey lines show the remaining nine models and the red diamonds the measurements from Table 1.3.

Second of all, the page lists the top ten models that fit the data, indicating the inclination, the total value of χ^2 (χ_{tot}^2 in the following), the interstellar extinction and the distance. These ten models all have the same inclination of 87.13° , but the values of the interstellar extinction and the distance vary within the ranges given above.

Figure 6.14 shows the SEDs of the top ten models in comparison to the data from Spitzer. We show the best model SED for three different sizes of the aperture radius in order to demonstrate its effect on the results. As mentioned before, the aperture radius does not have a big impact and all three curves are a very good fit to the data. The other models are shown in grey and match the data quite well, too. The SED of the best model has $\chi_{\text{tot}}^2 = 28.62$, that is, $\chi_{\text{dp}}^2 = 1.02$ and the SED of the “worst” (no. 10) model has $\chi_{\text{tot}}^2 = 42.53$ or $\chi_{\text{dp}}^2 = 1.52$. We also show the data points from Table 1.3 for comparison. We did not use these data as input for the online fitter because the available filters are different from those given in Table 1.3 and it is not possible to incorporate transmission curves of unknown filters.

The online fitter also provides a file that contains the parameters of the best 10000 models, sorted by their values of χ_{tot}^2 . This file can be used to calculate average values and variances of the parameters in order to identify the parameters that are well constrained and the ones that are not. Instead of using a fixed number of models for this, we use all models that satisfy the relation $\chi_{\text{tot}}^2 \leq 2\chi_{\text{tot,best}}^2$. This results in 17 different models for the Spitzer data and we present the average values, the standard deviation, the minimum and the maximum values of their parameters in Table 6.5. This table also contains the results from the fit to the MIDI data and is discussed at the end of the next chapter.

6.3.2 MIDI

Due to the fact that the data from MIDI span an even narrower range of wavelengths than the data from Spitzer, the plot with all models that satisfy $\chi_{\text{dp}}^2 - \chi_{\text{dp,best}}^2 < 3$ shows

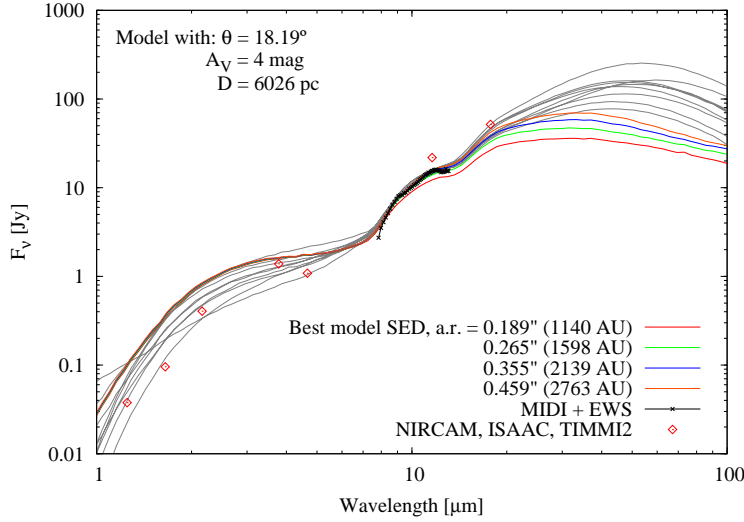


Figure 6.15: The top ten models of the grid compared to the data from MIDI. The four coloured curves all show the best model, but for different sizes of the aperture. The remaining models are shown in grey and the individual measurements from Table 1.3 are shown as red diamonds.

a very large number of models. This already indicates that the results will most likely not yield firm constraints for the individual parameters. However, the top ten models all agree concerning the inclination, 18.19° in this case, but again are distributed across the full ranges of A_V and D .

Figure 6.15 shows the spectrum from MIDI compared to the top ten models and the data from Table 1.3. The best model is shown again for different values of the aperture radius, but it only affects the SED for wavelengths larger than about $10 \mu\text{m}$, and each curve gives a reasonable fit to the MIDI data. However, the differences between the individual SEDs are larger than in Figure 6.14. The best SED of this model has $\chi_{\text{tot}}^2 = 21.56$, that is, $\chi_{\text{dp}}^2 = 0.43$ and the “worst” model has $\chi_{\text{tot}}^2 = 42.94$ or $\chi_{\text{dp}}^2 = 0.86$. In the case of the MIDI data, the relation $\chi_{\text{tot}}^2 \leq 2\chi_{\text{tot,best}}^2$ only leads to 10 different models.

6.3.3 Results

We now examine whether the good fits to the Spitzer and MIDI data shown above allow us to give firm estimates for the values of the parameters and how much these values agree with each other. The left hand side of Table 6.5 shows the results of the fit to the Spitzer data and the right hand side shows the corresponding values of the fit to the MIDI data. We leave the absolute values of the parameters aside for the time being, but rather concentrate on the two columns that show the ratio between the standard deviation and the mean value (entitled “%”). These columns give an immediate impression of how much the models which satisfy $\chi_{\text{tot}}^2 \leq 2\chi_{\text{tot,best}}^2$ agree with each other concerning a specific parameter. Based on these values we divide the list of parameters into four groups: parameters that are well constrained by the models ($\sigma/\bar{x} < 10\%$), parameters that are reasonably constrained ($10\% \leq \sigma/\bar{x} < 20\%$), parameters that are rather uncertain ($20\% \leq \sigma/\bar{x} < 100\%$) and parameters that are completely uncertain ($\sigma/\bar{x} \geq 100\%$).

In the case of the 17 models for the Spitzer data, there are six parameters which are

well constrained by the models. These are the inclination, the stellar radius and temperature, the outer radius of the envelope, the density profile exponent and the flaring parameter of the disk. In principle there are seven parameters which are reasonably constrained, but since we restrict the distance and interstellar extinction to rather narrow ranges from the outset (see above), they cannot vary by much more than 10 %. Therefore, only five parameters remain. These are the stellar mass, the inner radii of the envelope and the disk, the scale height of the disk and the density inside the cavity. All other parameters are quite uncertain, especially the YSO-internal extinction and the outer radius, mass and accretion rate of the disk which all have $\sigma > \bar{x}$. However, depending on the minimum and maximum values, we can also gain some instructive information in these cases (see discussion below).

The overall agreement between the 10 models for the MIDI data is slightly worse than the agreement between the models for the Spitzer data. Hence there are only three parameters which are well constrained, namely the inclination, the density profile exponent and the flaring parameter of the disk. Once again neglecting the distance and interstellar extinction, there are six parameters which are reasonably constrained. These are the stellar mass, the inner and outer radii of the envelope, the inner radius and scale height of the disk and the opening angle of the cavity. The remaining parameters show, on average, larger values for the ratio between the standard deviation and the mean value than the corresponding parameters for the Spitzer data.

What are the conclusions that we can draw from this? Unfortunately, the results of the two fits not only differ with respect to their accuracy, but also regarding (most of) the absolute values of their parameters. Therefore, we first have to decide whether we want to trust the results from the fit to the Spitzer data or the corresponding results from the MIDI data, although some more general statements about the nature of IRS 9A emerge in both cases. It is difficult to evaluate the advantages and disadvantages of the two instruments and telescopes in this respect. Of course, Spitzer offers higher spectral resolution, observes from space and covers a larger range of wavelengths. Yet its spatial resolution is a factor of 10 worse, which might lead to contamination effects from nearby sources. However, we think that the advantages of Spitzer outweigh its poor spatial resolution, especially when considering the fact that IRS 9A is by far the brightest (MIR) source of the IRS 9 cluster. Thus, in the following summary we will concentrate on the results of the fit to the Spitzer data and only briefly mention the differences of the two results.

The models that are able to reproduce the SED as measured by Spitzer all involve very young and massive protostars. None of them is older than a few times 10^5 years and most of them are more massive than $20 M_{\odot}$; some are even close to $40 M_{\odot}$. They have temperatures of about 40000 K and, in combination with the accretion luminosity of the envelope and the disk, account for the total luminosity of the system which is approximately $10^5 L_{\odot}$. The Spitzer data favour almost edge-on inclinations of the accretion disk and envelope, which lead to very high values of the intrinsic extinction of the YSO along

Parameter	Spitzer (17 models)					MIDI (10 models)				
	Best	$\bar{x} \pm \sigma$	%	Min	Max	Best	$\bar{x} \pm \sigma$	%	Min	Max
D [pc]	6026	6752 ± 730	11	6026	7943	6026	6702 ± 726	11	6026	7943
$A_{V_{IS}}$	4.00	4.58 ± 0.47	10	4.00	5.00	4.00	4.35 ± 0.46	11	4.00	5.00
$A_{V_{YSO}}$	2405	14040 ± 14690	105	107.6	47330	5.85	5.22 ± 1.85	36	2.78	8.89
ϕ [°]	87.1	85.8 ± 2.5	3	81.4	87.1	18.2	18.2 ± 0.0	0	18.2	18.2
t_c [yr]	1.2×10^5	$1.4 \times 10^5 \pm 9.4 \times 10^4$	65	2.9×10^4	3.7×10^5	1.4×10^4	$9.2 \times 10^4 \pm 1.0 \times 10^5$	109	1.3×10^4	3.2×10^5
M_c [M_\odot]	27.3	27.6 ± 3.3	12	18.4	34.3	16.3	15.3 ± 1.5	10	12.7	16.9
R_c [R_\odot]	6.85	6.92 ± 0.55	8	5.49	7.92	38.7	20.9 ± 17.7	85	4.4	44.6
T_c [K]	39340	39264 ± 1554	4	34300	41820	10660	21049 ± 10738	51	9140	33100
L_{tot} [L_\odot]	1.0×10^5	$1.1 \times 10^5 \pm 2.3 \times 10^4$	21	7.9×10^4	1.7×10^5	2.0×10^4	$1.9 \times 10^4 \pm 6.0 \times 10^3$	32	1.2×10^4	3.0×10^4
$R_{in,env}$ [R_{sub}]	1.00	1.03 ± 0.08	8	1.00	1.35	1.09	1.08 ± 0.19	17	1.00	1.60
$R_{out,env}$ [AU]	1.0×10^5	$1.0 \times 10^5 \pm 0.0$	0	1.0×10^5	1.0×10^5	1.0×10^5	$9.3 \times 10^4 \pm 1.7 \times 10^4$	19	4.5×10^4	1.0×10^5
$R_{in,disk}$ [R_{sub}]	1.00	1.03 ± 0.08	8	1.00	1.35	1.09	1.08 ± 0.19	17	1.00	1.60
$R_{in,disk}$ [AU]	26.5	28.5 ± 3.7	13	23.3	38.0	11.4	11.3 ± 1.8	16	9.1	14.1
$R_{out,disk}$ [AU]	631	377 ± 573	152	31	1942	12.7	80.2 ± 78.3	98	12.7	237.6
M_{env} [M_\odot]	129	93 ± 22	23	63	137	104	221 ± 148	67	95	595
M_{disk} [M_\odot]	0.022	0.156 ± 0.188	120	7.0×10^{-4}	0.655	0.244	0.079 ± 0.102	130	0.002	0.244
\dot{M}_{env} [M_\odot/yr]	3.6×10^{-4}	$2.4 \times 10^{-4} \pm 8.9 \times 10^{-5}$	37	1.5×10^{-4}	4.4×10^{-4}	1.8×10^{-4}	$4.6 \times 10^{-4} \pm 3.4 \times 10^{-4}$	73	1.6×10^{-4}	1.1×10^{-3}
\dot{M}_{disk} [M_\odot/yr]	3.9×10^{-7}	$6.0 \times 10^{-5} \pm 1.6 \times 10^{-4}$	266	1.1×10^{-9}	6.6×10^{-4}	2.9×10^{-4}	$3.1 \times 10^{-5} \pm 9.0 \times 10^{-5}$	290	1.7×10^{-8}	2.9×10^{-4}
a_{disk}	2.10	2.09 ± 0.05	2	2.01	2.16	2.13	2.09 ± 0.06	3	2.01	2.20
b_{disk}	1.10	1.09 ± 0.05	5	1.01	1.16	1.13	1.09 ± 0.06	6	1.01	1.20
h_{100} [AU]	5.46	7.25 ± 1.39	19	4.95	8.93	7.30	6.45 ± 0.79	12	5.40	7.77
α_{disk}	0.062	0.033 ± 0.031	92	0.001	0.079	0.025	0.011 ± 0.009	80	0.003	0.025
θ_{cav} [°]	37.9	32.0 ± 6.4	20	21.7	43.5	17.4	16.1 ± 2.4	15	12.5	20.1
ρ_{cav} [g/cm^3]	1.0×10^{-20}	$8.4 \times 10^{-21} \pm 1.6 \times 10^{-21}$	19	6.3×10^{-21}	1.2×10^{-20}	1.7×10^{-20}	$1.2 \times 10^{-20} \pm 5.3 \times 10^{-21}$	45	6.5×10^{-21}	2.4×10^{-20}
ρ_{amb} [g/cm^3]	5.1×10^{-21}	$6.5 \times 10^{-21} \pm 1.7 \times 10^{-21}$	26	4.5×10^{-21}	1.1×10^{-20}	6.2×10^{-21}	$5.9 \times 10^{-21} \pm 1.7 \times 10^{-21}$	29	2.4×10^{-21}	8.1×10^{-21}

Table 6.5: Average values of the best models for the data from Spitzer and MIDI. The columns show the parameter values of the model with the lowest χ^2_{tot} (Best), the mean values and the standard deviation ($\bar{x} \pm \sigma$), the value of σ/\bar{x} in % (%), the minimum value (Min) and the maximum value (Max). Parameters: D: distance, $A_{V_{IS}}$: interstellar extinction, $A_{V_{YSO}}$: extinction from the outside of the YSO to the stellar surface (measured along the line of sight), ϕ : inclination to the line of sight, t_c , M_c , R_c , T_c : age, mass, radius and temperature of the central source, L_{tot} : total system luminosity, $R_{in,env}$, $R_{out,env}$, $R_{in,disk}$, $R_{out,disk}$: inner and outer radii of the envelope and the disk, M_{env} , M_{disk} : mass of the envelope and the disk (dust + gas), \dot{M}_{env} , \dot{M}_{disk} : infall/accretion rate of the envelope and the disk, a_{disk} , b_{disk} , h_{100} , α_{disk} : density profile exponent, flaring parameter, scale height at 100 AU and α -parameter of the disk, θ_{cav} : opening angle of the cavity, ρ_{cav} : density inside the cavity, ρ_{amb} : ambient density. The dust sublimation radius is denoted with R_{sub} . Note that this radius is in general different for each model, hence the standard deviation of $R_{in,disk}$ [R_{sub}] and $R_{in,disk}$ [AU] are also different.

the line of sight (minimum of 100 mag). The geometry of the circumstellar envelope and the disk is rather similar for all models, with the exception of the outer radius of the disk. The latter varies from 30 AU to about 2000 AU which leads to a huge range of masses of the disk. However, the mass contained in the envelope is always larger than $60 M_{\odot}$, providing a large reservoir to allow for further growth of the protostar. If we assume that the envelope and the disk can survive for some 10^4 years more, the accretion and infall rates of up to $\approx 5 \times 10^{-4} M_{\odot}/\text{yr}$ would indeed transport substantial amounts of gas and dust towards the centre. Depending on how much of this material actually reaches the protostar and how much is ejected in the form of outflows (see, e.g., Matzner & McKee 2000), its mass could increase by a considerable amount.

The models that can account for the data from MIDI favour rather pole-on inclinations, leading to intrinsic extinctions of only 3–9 mag. The central object is slightly younger and less massive, hence its temperature and luminosity are also lower. Yet the mass and infall rate of the envelopes of these systems are even higher, and they might evolve into systems that are similar to the ones found for the data from Spitzer in the future.

7 Summary and discussion

In the previous chapter we presented the methods and results of our different attempts to model the observational data of IRS 9A. They are summarised and discussed hereafter and we also refer to the short summary of our findings with MIDI given in Section 4.5, where we outlined the immediate results of our observations and also some of the conditions that a suitable model has to fulfill.

Simple brightness distributions, binary and accretion disk models:

Our first step was to use very simple models for the brightness distribution that can be described by only a few analytical equations in order to get a first impression of the size scales, inclinations and orientations that are determined by the visibilities.

- ▷ Due to the different geometric shapes of the models, we obtain the best fits for a range of angular sizes. For $\lambda \approx 8 \mu\text{m}$ and $D = 7 \text{kpc}$ we obtain 144 AU for the inner diameter of an accretion disk, 329 AU for the inner diameter of a ring, 478 AU for the FWHM of a Gaussian and 521 AU for the diameter of a uniform disk.
- ▷ Except for a binary model, all models favour inclinations of about 60° and position angles of around 130° .
- ▷ A binary model can be ruled out for brightness ratios larger than 0.1 and angular scales larger than about 30 mas.

In spite of their simplicity, these models already allow us to rule out a binary nature of IRS 9A. To be more precise, we can rule out a (mid-infrared) bright companion with a distance to IRS 9A of more than 200 AU. A companion with an even smaller distance and only weak mid-infrared emission seems very unlikely. Considering the observed multiplicity of high-mass stars (see Section 1.2), this is an important result.

Interestingly, the inner radius of the best accretion disk model lies halfway between the inner radii of disk models 1 and 2 (110 AU and 20 AU, respectively). Its inclination of 61° is also not too far from the corresponding values of the disk models, whereas the position angle of 137° is only somewhat close to disk model 1. However, one can not easily compare the results of these models as their appearance to MIDI is calculated in a totally different way. Hence the relations should not be overinterpreted.

Radiative transfer models:

The next step was to use the radiative transfer codes DUSTY and MC3D. However, before we summarise the results of the individual models, we first return to our statement at the beginning of Section 6.2, where we emphasized that all our radiative transfer models

make use of the steady-state approximation. In fact, this approach is very common as it simplifies the theoretical description considerably, but it also has its drawbacks. As an example we refer to the radiative cooling rate of an optically thin gas which is described in Schmutzler & Tscharnuter (1993). The authors show that a time-dependent approach leads to a different energy loss rate and hence cooling timescale than in the commonly assumed case of collisional ionisation equilibrium. However, since it was not the goal of this work to develop a time-dependent radiative transfer code, we took the DUSTY and MC3D codes “as is” and did not attempt to incorporate any such effects. Thus, it is not clear whether the particular timescales of our models actually permit the use of the steady-state assumption or not.

DUSTY:

DUSTY is restricted to one-dimensional geometries, but this enables a very efficient and hence fast solution of the radiative transfer problem. Using models with different values of the chemical composition of the dust and the size distribution of the grains, different density distributions and optical depths, we find the following results:

- ▷ It is possible to devise models that are able to reproduce the individual interferometric datasets from MIDI and Gemini South.
- ▷ However, these models are fundamentally different from each other and within the range of parameters given in Table 6.3 we are not able to find models that can account for both datasets at the same time.
- ▷ The spectra of the models that can account for the interferometric datasets yield very poor fits to the observed SED and we did not attempt to construct a model that is able to give a reasonable reproduction of the measured SED.

Our modelling efforts with DUSTY show that spherically symmetric density distributions are inappropriate in order to explain the visibilities and the SED of IRS 9A, bearing in mind the shortcomings of our grid search and the set of adopted parameters. Fitting individual datasets is quite possible, although some of these models exhibit questionable parameters. It seems that a more complex structure of the circumstellar gas and dust around IRS 9A is a crucial ingredient in order to construct an effective model.

MC3D:

MC3D is able to calculate images and SEDs for arbitrary, three-dimensional dust configurations around one or more stars. We used the code to test whether models that are composed of a circumstellar disk or a combination of a disk and a spherical envelope lead to improved fits to our data. The parameters of our grid search are given in 6.4.

- ▷ Using models which involve only a circumstellar disk, we find two models that are able to reproduce the visibilities from MIDI (“disk model 1 and 2”). The disks differ with respect to their radial extent, mass and scale height, and they are also seen under different inclinations and at different position angles.

-
- ▷ The agreement of these models with the data from Gemini South is better than that of the DUSTY models, but overall is still quite poor. Their SEDs are similar and cannot account for the steep slope of IRS 9A’s spectrum. Furthermore, they both show pronounced silicate emission.
 - ▷ Using gas and dust distributions which are composed of a disk and a spherical envelope, we are able to devise a model that can simultaneously account for all our observational data (“disk + shell model”). We find that the envelope has to be quite thin and we also have to reduce the luminosity of the central source to $1.2 \times 10^5 L_{\odot}$. The SED of this model shows only a very weak silicate emission feature.

Once again we stress that, even within the range of parameters of our grid search, there might exist a specific combination of parameters that leads to a better model. However, searching for models that are able to reproduce both the SED and the spatial structure from low to very high angular resolution is certainly not an easy task. Therefore, even though the individual fits are not perfect, we estimate the agreement between the disk + shell model and the observations of IRS 9A to be quite remarkable.

Certainly, it would be rewarding to test alternative configurations of the model. In the last paragraph of Section 6.2.2.1 we mentioned that in the case of RY Tau (see Schegerer et al. 2008), models with actively accreting disks have the same effects on the SED and the visibilities in the near- and mid-infrared as passive disks with a dusty envelope. This does not necessarily have to be the case for IRS 9A, which is much more massive and luminous, so that the effects of accretion might be different. However, due to IRS 9A’s appearance in low-resolution observations, we would still need some kind of dusty shell. It would also be interesting to improve the description of the envelope by using a separate parameter for its density distribution and smooth transitions at the inner and outer radii. Yet both modifications would increase the number of free parameters.

If we assume the common value of the gas-to-dust ratio of 100:1 (e.g. Whittet 1992), the total mass of the disk of our best model is $3 M_{\odot}$. The mass of IRS 9A, on the other hand, is estimated to be about $40 M_{\odot}$, and hence the disk is close to being in a self-gravitating state. Considering the fact that fully self-gravitating disks evolve much faster, this is not surprising. It is simply much more likely to observe a disk in this state.

We do not try to model the asymmetric structure of IRS 9A which is observed in the acquisition images and the image from Gemini South. Instead we refer to Nürnberger (2008) for a discussion about the probable origin of these asymmetries. They seem to point away from the direction of the nearby OB cluster, hence ionising radiation or stellar winds might be seen to interact with the circumstellar envelopes.

Fitting the spectra to a large grid of young stellar object SEDs:

The grid of YSO SEDs and the online fitter by Robitaille et al. (2006, 2007) provide a convenient way of interpreting spectra and offer a wide range of physical parameters. The parameters of the models that are able to reproduce the observations can be compared to additional data or other models. Using the SEDs from Spitzer and MIDI we obtain the following results.

- ▷ For each dataset we obtain several models that lead to a proper reproduction of the SED. The number of models is higher in the case of the MIDI data which cover a narrower range of wavelengths. This leads to a larger scatter of the parameters on average and we presume that the models for the data from Spitzer are more reliable.
- ▷ By calculating mean values of the parameters of the models that fulfill the relation $\chi_{\text{tot}}^2 \leq 2\chi_{\text{tot,best}}^2$, we are able to give firm estimates for some of the parameters, whereas in other cases we can only restrict the values to a certain range.
- ▷ The models obtained for the data from Spitzer indicate that IRS 9A is very young ($\approx 10^5$ yr), massive ($\approx 30 M_{\odot}$), hot (≈ 40000 K) and luminous ($\approx 10^5 L_{\odot}$, including contributions from infall/accretion). There is a considerable discrepancy concerning the size and mass of the circumstellar disk which is seen edge-on, but the mass of the envelope is always larger than $60 M_{\odot}$. If these configurations can survive for some 10^4 years more, the infall/accretion rates might lead to further, substantial growth of IRS 9A.
- ▷ In comparison to the models obtained from the fit to the Spitzer data, the central objects of the models for the MIDI data are generally younger, less massive and also have a lower temperature and luminosity. The inclination of these models is close to pole-on.

Despite the fact that these models provide a much more accurate description of a YSO, including accretion, infall from an envelope and bipolar cavities, one has to keep in mind that this involves a large number of free parameters. Hence, in order to obtain meaningful results, the SED of the object under investigation should be known across a very large range of wavelengths. Our data from Spitzer and MIDI are certainly not optimal in this respect. However, as outlined above, they already allow us to give quite accurate estimates for some crucial parameters, while others can be confined to a certain range. The online fitter also does not offer a straightforward way to incorporate spatial information on an object, for example in the form of visibilities. This would most likely decrease the number of suitable models by a considerable amount.

How do the aforementioned parameters of IRS 9A and its disk/envelope compare to the ones from Table 1.3 and our best MC3D model? Concerning IRS 9A by itself we see that there is reasonable agreement on its age and mass, whereas the temperatures and luminosities differ by a factor of about 2. There is a huge discrepancy between the estimated amount of circumstellar material, even considering the fact that the (estimated) value from Table 1.3 is a lower limit. This estimate could be improved by measuring the far-infrared or sub-millimeter flux of IRS 9A, which would also be rewarding with regard to the results of the online fitter. Concerning the disk, the parameters a , b and h_{100} are very similar, but most of the disks from the YSO grid are much smaller and less massive than the one from our best MC3D model.

8 Conclusions

In this work we try to devise a model of the circumstellar structure of IRS 9A, a member of the rare class of massive young stellar objects, in order to improve our understanding of the processes that lead to the formation of high-mass stars. We make use of several observing techniques. First and foremost, we obtained mid-infrared interferometric observations with MIDI at the VLTI which represent the data with the highest spatial resolution available in this wavelength range. These data also contain a low resolution spectrum of IRS 9A in the N band. Second, we make use of aperture masking observations taken at the Gemini South telescope which extend our interferometric observations to small spatial frequencies. Third, we received a moderate resolution spectrum taken with the Spitzer Space Telescope, covering a larger range of wavelengths than the spectrum from MIDI.

With regard to the many observational problems connected to high-mass star formation, IRS 9A is located in an advantageous position close to a cluster of OB stars. This region and the properties of IRS 9A that were known previous to this study are summarised in Section 1.3. Based on our observations and the results of our different modelling efforts, we are able to confirm some of these parameters, give estimates of previously unknown quantities and in particular present a model of the circumstellar structure. In the following we describe the characteristics of IRS 9A as they emerge from our study, before evaluating these results in view of the theory of high-mass star formation.

Our low resolution observations show that IRS 9A is surrounded by a slightly asymmetric envelope of gas and dust, distributed on scales of about 2500 AU to 3200 AU. This circumstellar material leads to strong infrared excess emission and spectral indices in the range of 1.1 to 2.3, depending on the wavelength range and telescopes used. The N band spectrum that originates from the centre of IRS 9A shows the [Ne II] line in emission, but apart from that there are no signs for other spectral features, especially no emission or absorption due to silicates. The latter is also true for the large aperture SED from Spitzer, but, apart from the [Ne II] line, it shows several other forbidden emission lines and PAH features. We conclude that the origin of the [S IV] emission lies outside of MIDI's FOV of about 0.3 arcseconds. The visibilities confirm that the circumstellar gas and dust is quite extended, as MIDI fully resolves the emission of IRS 9A on scales of 30–95 mas and wavelengths from 9 μm to 13 μm . Yet we detect a compact, unresolved structure that emerges at wavelengths below 9 μm . The differential phases show that the position of the photo centre of IRS 9A depends on wavelength, spatial resolution and position angle.

We use a large number of fundamentally different models in order to further constrain the properties of IRS 9A and the material in its immediate surroundings. These models allow us to exclude a possible binary nature of IRS 9A on angular scales down to 30 mas

and for brightness ratios larger than 0.1. We are not able to reconcile the observations with spherically symmetric models, but we show that the combination of a circumstellar disk and a dusty envelope leads to a proper reproduction of all our observational data. Together with the models that were selected based on the SED from Spitzer, we can confirm previous estimates that IRS 9A is indeed a very young and massive object. However, the best agreement between the models and the data is found if we reduce its luminosity by about a factor of two. There is some ambiguity concerning its temperature and we also cannot give precise values of the size, mass and accretion rate of the circumstellar disks and envelopes. We stress that, within the scope of our modelling efforts, we find that IRS 9A's properties can also be explained without including any accretion effects. If, however, accretion is included, the corresponding mass flow rates are quite high, potentially allowing for further growth of the central object.

Altogether our analysis of IRS 9A supports the idea that high-mass stars can form via accretion of material from circumstellar disks and envelopes, akin to the way in which low- and intermediate-mass stars form. Similar results have already been found for Herbig Ae/Be stars (Leinert et al. 2004) and in recent theoretical investigations of massive star formation (Krumholz et al. 2009). However, even though our work provides convincing evidence that IRS 9A will develop into a high-mass main sequence star, we cannot give any predictions about its final mass. The main accretion phase might already be over, but it is also possible that IRS 9A is still accumulating mass. Hence observational evidence for the formation of the most massive stars with $M_{\star} \approx 100 M_{\odot}$ is still pending.

We already mentioned some of the aspects which should be addressed in the future, for example the inclusion of accretion effects in our MC3D models. Depending on whether or not the corresponding models are better suited to explain the observational data, we could decide if IRS 9A is still actively accreting circumstellar material or not. It would also be very rewarding to calculate images for the best models from Section 6.3 and use them to calculate the visibilities which correspond to the u - v -coverage of the observations of MIDI and Gemini South. It is not unlikely that some of these models are incompatible with one or even both sets of visibilities. Our study would also benefit from additional observational data. Visibility measurements using projected baselines that cover the range between the ones from MIDI and Gemini South would be able to further constrain the number of suitable models. Likewise, measurements of IRS 9A's flux in the visual, far-infrared or sub-millimetre ranges would yield valuable constraints for the SED fits, even if these values are fairly uncertain. A measurement of the sub-millimetre flux would also allow an independent estimate to be made for the circumstellar dust mass. Quite possibly the problem of the formation of the most massive stars will not be settled until new telescopes and instruments have been built. With regard to (high-mass) star formation, the most important ones are the Atacama Large Millimeter Array, the James Webb Space Telescope, Herschel and also new instruments for the VLTI which will combine more telescopes than MIDI or AMBER and allow imaging. These observations will set new benchmarks in terms of sensitivity and angular resolution and will challenge the numerical simulations which are constantly improving as well.

A Observing log

The following pages summarise our observations with MIDI in three tables. Each table contains the date and time of the individual observations, the values for the seeing and the airmass and optional comments. Apart from that, the table for the acquisition images also contains the coherence time and the filter which was used, the table for the interferometric observations lists the coherence time and the baseline together with the projected length and position angle, and the table for the photometric observations also indicates which telescopes were used. Table A.1 below lists the coordinates of IRS 9A and HD 107446.

	Equatorial		Galactic	
	Right ascension	Declination	l	b
IRS 9A	11 ^h 15 ^m 11.34 ^s	−61°16′45.20″	291°37′56.28″	−0°32′13.20″
	11.25315 h	−61.27922°	291.6323°	−0.5370°
HD 107446	12 ^h 21 ^m 21.61 ^s	−60°24′04.13″	299°13′23.16″	2°15′13.68″
	12.35600 h	−60.40115°	299.2231°	2.2538°

Table A.1: The equatorial and galactic coordinates (ICRS, J2000) of IRS 9A (from Nürnberger 2003) and HD 107446 (from Perryman et al. 1997).

Airmass

The term *airmass* specifies the relative “amount” of atmosphere between the telescope and a celestial source. The airmass has to be measured/calculated for every observation since the light is attenuated in the atmosphere by scattering and absorption. By definition, the airmass of a source at the zenith is 1. For small distances to the zenith one can use the approximation $\text{airmass} \approx 1/\cos(\theta)$, where θ is the angular distance to the zenith (*zenith angle*). When the zenith angle increases the accuracy of the formula decreases since the atmosphere is neither homogeneous nor plane-parallel. According to the simple approximation, a source at the horizon would have an airmass of infinity, while the proper value is usually a bit less than 40.

Target	Date & Time	Seeing ["']	Airmass	τ_0 [ms]	Filter	Classification of observations (night reports)
HD 107446	2005-02-27 - 04:10:15	0.57	1.38	5.21	SiC	X (coordinates of target incorrect)
HD 107446	" 06:19:53	0.68	1.23	4.32	N8.7	A
HD 107446	" 07:55:37	0.52	1.28	5.84	N8.7	A
IRS 9A	" 08:29:30	0.56	1.49	6.44	N8.7	A
HD 107446	" 09:10:50	1.20	1.41	3.06	N8.7	A (MACAO loop opened twice during fringe track)
HD 107446	2005-02-28 - 03:40:22	0.56	1.44	5.13	N8.7	A
HD 107446	" 05:30:20	0.69	1.26	4.13	N8.7	A
HD 107446	" 06:18:23	0.60	1.23	6.34	N11.3	A
IRS 9A	" 06:41:29	0.63	1.29	5.74	N8.7	A
HD 107446	" 07:03:46	0.62	1.24	4.90	N8.7	A
IRS 9A	" 07:38:25	0.49	1.37	6.63	N8.7	C (only because calibrator afterwards is C)
HD 107446	" 07:59:06	0.61	1.29	5.53	N8.7	C (periodical OPD oscillation, abnormal visibility)
IRS 9A	" 08:27:06	0.52	1.49	6.37	N8.7	B (LST out of range)
HD 107446	" 08:48:37	0.51	1.37	6.35	N8.7	A
IRS 9A	" 09:12:21	0.53	1.66	6.01	N8.7	B (LST out of range)
HD 107446	" 09:43:32	0.57	1.51	5.45	N8.7	A
HD 107446	2005-03-03 - 04:15:59	0.81	1.34	7.79	N8.7	A
HD 107446	" 05:21:13	-1.00	1.25	9.99	N11.3	A
IRS 9A	" 07:05:03	0.68	1.33	8.42	N8.7	B
HD 107446	" 07:43:50	0.61	1.28	7.43	N8.7	A
IRS 9A	" 08:48:39	0.52	1.61	8.40	N8.7	B
HD 107446	" 09:10:18	0.57	1.45	7.65	N8.7	A
HD 107446	" 09:28:54	0.62	1.50	6.91	N8.7	C (twilight, MACAO loop opened)
HD 107446	" 09:46:25	1.00	1.56	4.27	N8.7	A

Table A.2: Journal of observations: acquisition images. The classification of the observations is as follows: A = fully within specifications, B = mostly within specifications, C = out of specifications, X = uncertain / not applicable.

Target	Date & Time	Seeing ["]	Airmass	τ_0 [ms]	Baseline	B_{proj} [m]	P.A. [deg]	Comments
HD 107446	2005-02-27 - 04:15:14	0.64	1.37	4.69	UT2–UT3	44.58	21.22	outlier
HD 107446	" 06:25:30	0.54	1.23	5.48	"	41.99	44.50	
HD 107446	" 08:01:27	0.52	1.28	5.91	"	38.09	61.27	
IRS 9A	" 08:35:10	0.55	1.51	6.65	"	31.83	80.41	
HD 107446	" 09:16:19	1.32	1.42	2.79	"	33.66	74.77	
HD 107446	2005-02-28 - 03:45:55	0.55	1.43	5.03	UT2–UT3	44.81	16.57	bad visibility (> 1) outlier
HD 107446	" 05:38:16	0.60	1.25	4.82	"	43.15	36.86	
HD 107446	" 06:24:13	0.50	1.23	7.19	"	41.91	44.96	
IRS 9A	" 06:48:35	0.67	1.29	4.40	"	38.04	61.29	
HD 107446	" 07:09:28	0.53	1.24	5.76	"	40.29	52.86	
IRS 9A	" 07:43:50	0.62	1.38	4.94	"	34.97	71.33	
HD 107446	" 08:04:48	0.58	1.29	5.81	"	37.72	62.55	
IRS 9A	" 08:33:25	0.52	1.51	6.28	"	31.68	80.85	
HD 107446	" 08:54:31	0.53	1.38	6.11	"	34.83	71.47	
IRS 9A	" 09:21:12	0.52	1.70	6.04	"	28.10	90.86	
HD 107446	" 09:48:34	0.51	1.53	6.26	"	31.09	81.71	
HD 107446	2005-03-02 - 04:21:49	0.81	1.33	7.86	UT3–UT4	56.01	81.93	
HD 107446	" 05:27:17	–1.00	1.25	8.88	"	59.34	96.28	
IRS 9A	" 07:10:49	0.65	1.34	8.82	"	62.46	132.32	
HD 107446	" 07:49:38	0.65	1.29	7.01	"	62.43	126.42	
IRS 9A	" 08:54:33	0.58	1.63	7.67	"	61.95	155.87	
HD 107446	" 09:16:19	0.54	1.47	8.01	"	62.18	145.60	
HD 107446	" 09:33:24	0.77	1.52	5.62	"	62.05	149.51	
HD 107446	" 09:51:29	1.03	1.59	4.16	"	61.90	153.70	

Table A.3: Journal of observations: interferometric observations

Target	Date	Time		Telescopes		Seeing ["]		Airmass		Comments
		A open	B open	A	B	A	B	A	B	
HD 107446	2005-02-27	04:20:05	04:21:17	UT2	UT3	0.70	0.65	1.36	1.36	
HD 107446	"	06:30:47	06:31:54	"	"	0.51	0.50	1.23	1.23	
HD 107446	"	08:06:19	08:07:29	"	"	-1.00	0.48	1.29	1.29	
IRS 9A	"	08:40:02	08:41:10	"	"	0.58	0.54	1.52	1.52	
HD 107446	"	09:21:10	09:22:24	"	"	1.29	1.32	1.43	1.44	
HD 107446	2005-02-28	03:50:50	03:52:07	UT2	UT3	0.61	0.63	1.41	1.41	
HD 107446	"	05:43:28	05:44:38	"	"	0.59	0.55	1.25	1.25	
HD 107446	"	06:29:12	06:30:20	"	"	0.49	0.52	1.23	1.23	
IRS 9A	"	06:53:27	06:54:38	"	"	0.65	0.70	1.30	1.30	flux abnormally high in B
HD 107446	"	07:14:22	07:15:34	"	"	0.59	0.60	1.25	1.25	
IRS 9A	"	07:48:51	07:50:06	"	"	0.59	0.60	1.39	1.40	
HD 107446	"	08:10:00	08:11:12	"	"	0.63	0.63	1.30	1.30	
IRS 9A	"	08:38:43	08:39:51	"	"	0.44	0.47	1.53	1.53	
HD 107446	"	08:59:47	09:01:02	"	"	-1.00	-1.00	1.39	1.39	flux abnormally high in A and B
IRS 9A	"	09:26:18	09:27:33	"	"	0.52	0.56	1.72	1.73	flux abnormally high in B
IRS 9A	"	09:33:03	09:34:12	"	"	0.52	0.53	1.76	1.76	
HD 107446	"	09:53:34	09:54:49	"	"	0.62	0.53	1.55	1.55	
HD 107446	2005-03-03	04:26:47	04:27:57	UT3	UT4	0.79	0.78	1.32	1.32	
HD 107446	"	05:32:28	05:33:40	"	"	0.90	0.95	1.25	1.25	
IRS 9A	"	07:15:56	07:17:10	"	"	0.62	0.59	1.35	1.35	
HD 107446	"	07:54:50	07:56:03	"	"	0.66	0.67	1.29	1.30	
IRS 9A	"	08:59:34	09:00:46	"	"	0.51	0.51	1.65	1.66	
HD 107446	"	09:21:21	09:22:41	"	"	0.52	0.57	1.48	1.48	
HD 107446	"	09:38:30	09:39:41	"	"	0.95	0.98	1.54	1.54	
HD 107446	"	09:56:28	09:57:46	"	"	0.81	0.78	1.60	1.61	

Table A.4: Journal of observations: photometric observations. The observations are taken separately with each of the telescopes and A and B refer to the shutters of MIDI.

B Transmission curves of MIDI filters

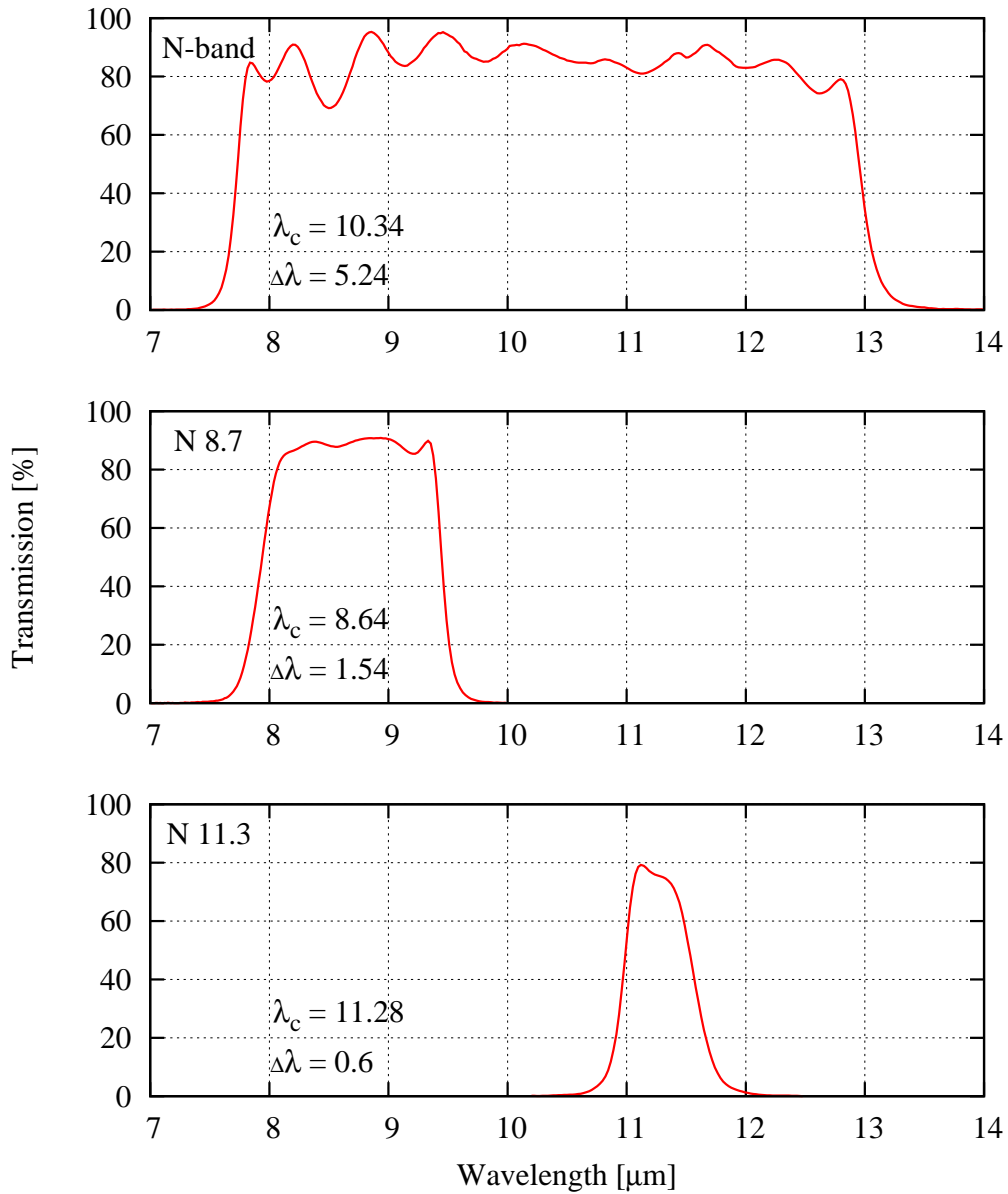


Figure B.1: Transmission curves for three of MIDI's filters. Top: the filter for the whole N band, middle: the N 8.7 filter which was used for most of the acquisition images, bottom: the N 11.3 filter.

C List of acronyms, units and constants

Acronyms

AMBER	Astronomical Multi-BEam combineR
AO	Adaptive Optics
AT	Auxiliary Telescope
DIT	Detector Integration Time
ESO	European Southern Observatory
EWS	Expert Work Station
FINITO	Fringe-tracking Instrument of NIce and TOrino
FOV	Field Of View
FWHM	Full Width at Half Maximum
IDL	Interactive Data Language
IMF	Initial Mass Function
IRAS	InfraRed Astronomical Satellite
IRIS	InfraRed Image Sensor
IRS	InfraRed Spectrograph / InfraRed Source
ISM	InterStellar Medium
ITR	Integrate-Then-Read
JPL	Jet Propulsion Laboratory
LST	Local Siderial Time
LTE	Local Thermodynamic Equilibrium
MACAO	Multi-Application Curvature sensing Adaptive Optics
MEM	Maximum Entropy Method
MIA	MIDI Interactive Analysis
MIDI	MID-infrared Interferometric instrument
MIR	Mid-InfraRed
MPIA	Max Planck Institute for Astronomy
MYSO	Massive Young Stellar Object
NASA	National Aeronautics and Space Administration
NIR	Near-InfraRed
OLBIN	Optical Long Baseline Interferometry News
OPD	Optical Path Difference

PA	Position Angle
PAH	Polycyclic Aromatic Hydrocarbon
PSF	Point Spread Function
RMS	Root Mean Square
SED	Spectral Energy Distribution
T-ReCS	Thermal-Region Camera Spectrograph
UD	Uniform Disk
UT	Unit Telescope
VISIR	VLT Imager and Spectrometer for the mid-InfraRed
VLT	Very Large Telescope
VLTI	Very Large Telescope Interferometer
VST	VLT Survey Telescope
YSO	Young Stellar Object

Units & constants

as	arcsecond	$1'' = \left(\frac{1}{3600}\right)^\circ = \frac{\pi}{180} \frac{1}{3600} \text{ rad} = 4.848 \times 10^{-6} \text{ rad}$
AU	Astronomical Unit	$1.4960 \times 10^{11} \text{ m} = 1.581 \times 10^{-5} \text{ ly} = 4.848 \times 10^{-6} \text{ pc}$
c	speed of light	$2.99792458 \times 10^8 \text{ m/s}$
L_\odot	solar luminosity	$3.846 \times 10^{26} \text{ W}$
ly	light-year	$9.4607 \times 10^{15} \text{ m} = 6.324 \times 10^4 \text{ AU} = 3.066 \times 10^{-1} \text{ pc}$
M_\odot	solar mass	$1.989 \times 10^{30} \text{ kg}$
mas	milliarcsecond	$10^{-3} \text{ arcseconds}$
pc	parsec	$3.0857 \times 10^{16} \text{ m} = 2.063 \times 10^5 \text{ AU} = 3.262 \text{ ly}$

Bibliography

- Adams, F. C., Lada, C. J., & Shu, F. H. (1987, Jan.). Spectral evolution of young stellar objects. *The Astrophysical Journal* 312, 788–806
- Allamandola, L. J., Tielens, A. G. G. M., & Barker, J. R. (1985, Mar.). Polycyclic aromatic hydrocarbons and the unidentified infrared emission bands - Auto exhaust along the Milky Way. *The Astrophysical Journal Letters* 290, L25–L28
- André, P., Ward-Thompson, D., & Barsony, M. (1993, Mar.). Submillimeter continuum observations of Rho Ophiuchi A - The candidate protostar VLA 1623 and prestellar clumps. *The Astrophysical Journal* 406, 122–141
- Arsenault, R., Alonso, J., Bonnet, H., et al. (2003, Feb.). MACAO-VLTI: An Adaptive Optics system for the ESO VLT interferometer. In *Adaptive Optical System Technologies II*, eds. P. L. Wizinowich & D. Bonaccini, Volume 4839 of *Society of Photo-Optical Instrumentation Engineers (SPIE) Conference Series*, 174–185
- Baldwin, J. E., Beckett, M. G., Boysen, R. C., et al. (1996, Feb.). The first images from an optical aperture synthesis array: mapping of Capella with COAST at two epochs. *Astronomy & Astrophysics* 306, L13–L16
- Baldwin, J. E., Haniff, C. A., Mackay, C. D., & Warner, P. J. (1986, Apr.). Closure phase in high-resolution optical imaging. *Nature* 320, 595–597
- Balick, B., Boeshaar, G. O., & Gull, T. R. (1980, Dec.). The giant galactic H II region NGC 3603 - Optical studies of its structure and kinematics. *The Astrophysical Journal* 242, 584–591
- Bernasconi, P. A. & Maeder, A. (1996, Mar.). About the absence of a proper zero age main sequence for massive stars. *Astronomy & Astrophysics* 307, 829–839
- Beuther, H., Churchwell, E. B., McKee, C. F., & Tan, J. C. (2007, Apr.). The Formation of Massive Stars. In *Protostars and Planets V*, eds. B. Reipurth, D. Jewitt & K. Keil. University of Arizona Press, Tucson, 2007, 165–180
- Boden, A. F. (2000, Jul.). Elementary Theory of Interferometry. In *Principles of Long Baseline Stellar Interferometry. Course notes from the 1999 Michelson Summer School*, ed. P. R. Lawson. NASA-JPL publication 00-009, 9–30
- Bonnell, I. A., Bate, M. R., Clarke, C. J., & Pringle, J. E. (1997, Feb.). Accretion and the stellar mass spectrum in small clusters. *Monthly Notices of the Royal Astronomical Society* 285, 201–208
- Bonnell, I. A., Bate, M. R., Clarke, C. J., & Pringle, J. E. (2001, May). Competitive accretion in embedded stellar clusters. *Monthly Notices of the Royal Astronomical Society* 323, 785–794
- Bonnell, I. A., Bate, M. R., & Zinnecker, H. (1998, Jul.). On the formation of massive stars. *Monthly Notices of the Royal Astronomical Society* 298, 93–102
- Bonnell, I. A., Larson, R. B., & Zinnecker, H. (2007, Apr.). The Origin of the Initial Mass Function. In *Protostars and Planets V*, eds. B. Reipurth, D. Jewitt & K. Keil. University of Arizona Press, Tucson, 2007, 149–164
- Born, M. & Wolf, E. (1999, Oct.). *Principles of Optics: Electromagnetic Theory of Propagation, Interference and Diffraction of Light* (seventh ed.). Cambridge, UK: Cambridge University Press, 1999
- Brandl, B., Brandner, W., Eisenhauer, F., et al. (1999, Dec.). Low-mass stars in the massive H II region NGC 3603. Deep NIR imaging with ANTU/ISAAC. *Astronomy & Astrophysics* 352, L69–L72
- Brandner, W., Grebel, E. K., Chu, Y.-H., et al. (2000, Jan.). HST/WFPC2 and VLT/ISAAC Observations of Proplyds in the Giant H II Region NGC 3603. *Astronomical Journal* 119, 292–301
- Brott, I. & Hauschildt, P. H. (2005, Jan.). A PHOENIX Model Atmosphere Grid for Gaia. In *The Three-Dimensional Universe with Gaia*, eds. C. Turon, K. S. O’Flaherty & M. A. C. Perryman, Volume 576 of *ESA Special Publication*, 565–568

Bibliography

- Caswell, J. L. & Haynes, R. F. (1987, Jan.). Southern H II regions - an extensive study of radio recombination line emission. *Astronomy & Astrophysics* 171, 261–276
- Chesneau, O. (2007, Oct.). MIDI: Obtaining and analysing interferometric data in the mid-infrared. In *Observation and Data Reduction with the VLT Interferometer - Proceedings of the VLTI Euro Summer School held in Goutelas, France, 4-16 June 2006*, eds. F. Malbet & G. Perrin, Volume 51. New Astronomy Review, 666–681
- Chesneau, O., Verhoelst, T., Lopez, B., et al. (2005, may). The mid-IR spatially resolved environment of OH 26.5+0.6 at maximum luminosity. *Astronomy & Astrophysics* 435, 563–574
- Chiang, E. I. & Goldreich, P. (1999, Jul.). Spectral Energy Distributions of Passive T Tauri Disks: Inclination. *The Astrophysical Journal* 519, 279–284
- Chini, R., Hoffmeister, V., Kimeswenger, S., et al. (2004, May). The formation of a massive protostar through the disk accretion of gas. *Nature* 429, 155–157
- Chini, R., Hoffmeister, V. H., Nielbock, M., et al. (2006, Jul.). A Remnant Disk around a Young Massive Star. *The Astrophysical Journal Letters* 645, L61–L64
- Cohen, M., Walker, R. G., Carter, B., et al. (1999, Apr.). Spectral Irradiance Calibration in the Infrared. X. A Self-Consistent Radiometric All-Sky Network of Absolutely Calibrated Stellar Spectra. *Astronomical Journal* 117, 1864–1889
- Cornwell, T. J. & Evans, K. F. (1985, Feb.). A simple maximum entropy deconvolution algorithm. *Astronomy & Astrophysics* 143, 77–83
- Coudé du-Foresto, V. & Ridgway, S. T. (1992). Fluor - a Stellar Interferometer Using Single-Mode Fibers. In *High-Resolution Imaging by Interferometry*, eds. J. M. Beckers & F. Merkle. European Southern Observatory, Garching bei München, Germany, 731–+
- Cox, A. N. (2000). *Allen's Astrophysical Quantities* (fourth ed.). New York: AIP Press; Springer, 2000
- Crowther, P. A. (2005). Near and mid infrared observations of ultracompact H II regions. In *Massive Star Birth: A Crossroads of Astrophysics*, eds. R. Cesaroni, M. Felli, E. Churchwell & M. Walmsley, Volume 227 of *IAU Symposium*, 389–396
- Crowther, P. A. & Dessart, L. (1998, May). Quantitative spectroscopy of Wolf-Rayet stars in HD 97950 and R136a - the cores of giant H II regions. *Monthly Notices of the Royal Astronomical Society* 296, 622–642
- de Buizer, J. & Fisher, R. (2005). T-ReCS and Michelle: The Mid-Infrared Spectroscopic Capabilities of the Gemini Observatory. In *High Resolution Infrared Spectroscopy in Astronomy*, eds. H. U. Käuffl, R. Siebenmorgen & A. Moorwood, 84–87
- de Pree, C. G., Nysewander, M. C., & Goss, W. M. (1999, Jun.). NGC 3576 and NGC 3603: Two Luminous Southern H II Regions Observed at High Resolution with the Australia Telescope Compact Array. *Astronomical Journal* 117, 2902–2918
- de Wit, W. J., Hoare, M. G., Oudmaijer, R. D., & Mottram, J. C. (2007, Dec.). VLTI/MIDI 10 μ m Interferometry of the Forming Massive Star W33A. *The Astrophysical Journal Letters* 671, L169–L172
- Deroo, P., van Winckel, H., Verhoelst, T., et al. (2007, jun). The circumbinary disc around the J-type C-star IRAS 18006-3213. *Astronomy & Astrophysics* 467, 1093–1101
- di Benedetto, G. P. & Conti, G. (1983, May). Stellar diameter measurements by two-aperture interferometry in the infrared. *The Astrophysical Journal* 268, 309–318
- Draine, B. T. & Lee, H. M. (1984, Oct.). Optical properties of interstellar graphite and silicate grains. *The Astrophysical Journal* 285, 89–108
- Duchêne, G., Simon, T., Eislöffel, J., & Bouvier, J. (2001, Nov.). Visual binaries among high-mass stars. An adaptive optics survey of OB stars in the NGC 6611 cluster. *Astronomy & Astrophysics* 379, 147–161
- Duley, W. W. & Williams, D. A. (1981, Jul.). The infrared spectrum of interstellar dust - Surface functional groups on carbon. *Monthly Notices of the Royal Astronomical Society* 196, 269–274
- Dullemond, C. P., Dominik, C., & Natta, A. (2001, Oct.). Passive Irradiated Circumstellar Disks with an Inner Hole. *The Astrophysical Journal* 560, 957–969

- Dyck, H. M. (2000, Jul.). Interferometry with Two Telescopes. In *Principles of Long Baseline Stellar Interferometry. Course notes from the 1999 Michelson Summer School*, ed. P. R. Lawson. NASA-JPL publication 00-009, 185–201
- Eisenhauer, F., Quirrenbach, A., Zinnecker, H., & Genzel, R. (1998, May). Stellar Content of the Galactic Starburst Template NGC 3603 from Adaptive Optics Observations. *The Astrophysical Journal* 498, 278–292
- Eisner, J. A., Lane, B. F., Akeson, R. L., Hillenbrand, L. A., & Sargent, A. I. (2003, May). Near-Infrared Interferometric Measurements of Herbig Ae/Be Stars. *The Astrophysical Journal* 588, 360–372
- Eisner, J. A., Lane, B. F., Hillenbrand, L. A., Akeson, R. L., & Sargent, A. I. (2004, Oct.). Resolved Inner Disks around Herbig Ae/Be Stars. *The Astrophysical Journal* 613, 1049–1071
- Fedele, D., van den Ancker, M. E., Acke, B., et al. (2008, Dec.). The structure of the protoplanetary disk surrounding three young intermediate mass stars. II. Spatially resolved dust and gas distribution. *Astronomy & Astrophysics* 491, 809–820
- Fischer, O., Henning, T., & Yorke, H. W. (1994, Apr.). Simulation of polarization maps. 1: Protostellar envelopes. *Astronomy & Astrophysics* 284, 187–209
- Fizeau, H. (1868). Prix Borodin: rapport sur le concours de l'année 1867. *Comptes Rendus de l'Académie des Sciences* 66, 932–934
- Fried, D. L. (1965). Statistics of a Geometric Representation of Wavefront Distortion. *Journal of the Optical Society of America (1917-1983)* 55, 1427–1435
- Frogel, J. A., Persson, S. E., & Aaronson, M. (1977, May). Compact infrared sources associated with southern H II regions. II. *The Astrophysical Journal* 213, 723–736
- Gai, M., Menardi, S., Cesare, S., et al. (2004, Oct.). The VLTI fringe sensors: FINITO and PRIMA FSU. In *New Frontiers in Stellar Interferometry*, ed. W. A. Traub, Volume 5491 of *Society of Photo-Optical Instrumentation Engineers (SPIE) Conference Series*, 528–539
- Gay, J. & Journet, A. (1973, Jan.). Infrared astronomy-Interferometric measurement of solar diameter. *Nature* 241, 32–33
- Glazenberg-Kluttig, A. W., Przygodda, F., Hanenburg, H., Morel, S., & Pel, J.-W. (2003, Feb.). Realization of the MIDI cold optics. In *Interferometry for Optical Astronomy II*, ed. W. A. Traub, Volume 4838 of *Society of Photo-Optical Instrumentation Engineers (SPIE) Conference Series*, 1171–1181
- Glindemann, A., Algomedo, J., Amestica, R., et al. (2003, Feb.). The VLTI – A Status Report. In *Interferometry for Optical Astronomy II*, ed. W. A. Traub, Volume 4838 of *Society of Photo-Optical Instrumentation Engineers (SPIE) Conference Series*, 89–100
- Glindemann, A., Bauvir, B., van Boekel, R., et al. (2001). ESO's VLT interferometer - first results. In *From optical to millimetric interferometry: scientific and technological challenges. Proceedings of the 36th Liège International Astrophysics Colloquium*, eds. J. Surdej, J. P. Swings, D. Caro & A. Detal, Volume 36 of *Liège International Astrophysical Colloquia*, 27–36
- Goss, W. M. & Radhakrishnan, V. (1969). The Distances of the Galactic H II Regions NGC 3576 and 3603. *Astrophysical Letters* 4, 199–203
- Goss, W. M., Radhakrishnan, V., Brooks, J. W., & Murray, J. D. (1972, Jan.). The Parkes Survey of 21-Centimeter Absorption in Discrete-Source Spectra. IV. 21-Centimeter Absorption Measurements on Low-Latitude Sources South of Declination -46° . *The Astrophysical Journal Supplement Series* 24, 123–159
- Hanbury Brown, R., Davis, J., & Allen, L. R. (1974, Apr.). The angular diameters of 32 stars. *Monthly Notices of the Royal Astronomical Society* 167, 121–136
- Hanbury Brown, R. & Twiss, R. Q. (1956a, Jan.). Correlation between Photons in two Coherent Beams of Light. *Nature* 177, 27–29
- Hanbury Brown, R. & Twiss, R. Q. (1956b, Nov.). A test of a new type of stellar interferometer on Sirius. *Nature* 178, 1046–1048
- Houck, J. R., Roellig, T. L., van Cleve, J., et al. (2004, Sep.). The Infrared Spectrograph (IRS) on the Spitzer Space Telescope. *The Astrophysical Journal Supplement Series* 154, 18–24
- Ivezić, Ž. & Elitzur, M. (1997, Jun.). Self-similarity and scaling behaviour of infrared emission from radiatively heated dust - I. Theory. *Monthly Notices of the Royal Astronomical Society* 287, 799–811

Bibliography

- Ivezić, Ž. & Elitzur, M. (1999, Mar.). Erratum: Self-similarity and scaling behaviour of infrared emission from radiatively heated dust - I. Theory. *Monthly Notices of the Royal Astronomical Society* 303, 864–864
- Ivezić, Ž., Nenkova, M., & Elitzur, M. (1999, Oct.). User Manual for DUSTY, Internal report, University of Kentucky, accessible at <http://www.pa.uky.edu/~moshe/dusty>
- Jackson, J. D. (1998, Aug.). *Classical Electrodynamics* (third ed.). New York: John Wiley and Sons, 1998
- Jaffe, W. J. (2004, Oct.). Coherent fringe tracking and visibility estimation for MIDI. In *New Frontiers in Stellar Interferometry*, ed. W. A. Traub, Volume 5491 of *Society of Photo-Optical Instrumentation Engineers (SPIE) Conference Series*, 715–724
- Johnson, M. A., Betz, A. L., & Townes, C. H. (1974). 10- μ m heterodyne stellar interferometer. *Physical Review Letters* 33, 1617–1620
- Kennicutt, Jr., R. C. (1984, Dec.). Structural properties of giant H II regions in nearby galaxies. *The Astrophysical Journal* 287, 116–130
- Kenyon, S. J. & Hartmann, L. (1987, Dec.). Spectral energy distributions of T Tauri stars - Disk flaring and limits on accretion. *The Astrophysical Journal* 323, 714–733
- Köhler, R., Petr-Gotzens, M. G., McCaughrean, M. J., et al. (2006, Nov.). Binary stars in the Orion Nebula Cluster. *Astronomy & Astrophysics* 458, 461–476
- Krumholz, M. R. & Bonnell, I. A. (2007, Dec.). Models for the Formation of Massive Stars. To be published in *Structure Formation in the Universe*, ed. G. Chabrier, *ArXiv e-print* 0712.0828
- Krumholz, M. R., Klein, R. I., McKee, C. F., Offner, S. S. R., & Cunningham, A. J. (2009, Jan.). The Formation of Massive Star Systems by Accretion. *Science* 323(5915), 754–757
- Krumholz, M. R., McKee, C. F., & Klein, R. I. (2005, Jan.). How Protostellar Outflows Help Massive Stars Form. *The Astrophysical Journal Letters* 618, L33–L36
- Kurucz, R. L. (1992). Model Atmospheres for Population Synthesis. In *The Stellar Populations of Galaxies*, eds. B. Barbuy & A. Renzini, Volume 149 of *IAU Symposium*, 225–232
- Köhler, R. (2005, aug). Do's and Don'ts of MIDI Data-reduction. *Astronomische Nachrichten* 326, 563–+
- Labeyrie, A. (1970, May). Attainment of Diffraction Limited Resolution in Large Telescopes by Fourier Analysing Speckle Patterns in Star Images. *Astronomy & Astrophysics* 6, 85–87
- Labeyrie, A. (1975, Mar.). Interference fringes obtained on VEGA with two optical telescopes. *The Astrophysical Journal Letters* 196, L71–L75
- Lada, C. J. (1987). Star formation - From OB associations to protostars. In *Star Forming Regions; Proceedings of the Symposium, Tokyo, Japan, Nov. 11-15, 1985*, eds. M. Peimbert & J. Jugaku, Volume 115 of *IAU Symposium*, 1–17
- Lawson, P. R. (1995, Feb.). Group-delay tracking in optical stellar interferometry with the fast Fourier transform. *Journal of the Optical Society of America A* 12, 366–374
- Lawson, P. R. (2000, Jul.). Notes on the History of Stellar Interferometry. In *Principles of Long Baseline Stellar Interferometry. Course notes from the 1999 Michelson Summer School*, ed. P. R. Lawson. NASA-JPL publication 00-009, 325–332
- Lawson, P. R., Scott, T. R., & Haniff, C. A. (1999, Mar.). Group-delay tracking and visibility fluctuations in long-baseline stellar interferometry. *Monthly Notices of the Royal Astronomical Society* 304, 218–224
- Lebouteiller, V., Bernard-Salas, J., Brandl, B., et al. (2008, Jun.). Chemical Composition and Mixing in Giant H II Regions: NGC 3603, 30 Doradus, and N66. *The Astrophysical Journal* 680, 398–419
- Lebouteiller, V., Brandl, B., Bernard-Salas, J., Devost, D., & Houck, J. R. (2007, Aug.). PAH Strength and the Interstellar Radiation Field around the Massive Young Cluster NGC 3603. *The Astrophysical Journal* 665, 390–401
- LeDrew, G. (2001, Feb.). The Real Starry Sky. *Journal of the Royal Astronomical Society of Canada* 95, 32–33

- Leger, A. & Puget, J. L. (1984, Aug.). Identification of the 'unidentified' IR emission features of interstellar dust? *Astronomy & Astrophysics* 137, L5–L8
- Leinert, C., Graser, U., Przygodda, F., et al. (2003a, Jul.). MIDI - the 10 μm instrument on the VLTI. *Astrophysics and Space Science* 286, 73–83
- Leinert, C., Graser, U., Richichi, A., et al. (2003b, Jun.). MIDI combines light from the VLTI: the start of 10 μm interferometry at ESO. *The Messenger* 112, 13–18
- Leinert, C., Graser, U., Waters, L. B. F. M., et al. (2003c, Feb.). Ten-micron instrument MIDI: getting ready for observations on the VLTI. In *Interferometry for Optical Astronomy II*, ed. W. A. Traub, Volume 4838 of *Society of Photo-Optical Instrumentation Engineers (SPIE) Conference Series*, 893–904
- Leinert, C., van Boekel, R., Waters, L. B. F. M., et al. (2004, Aug.). Mid-infrared sizes of circumstellar disks around Herbig Ae/Be stars measured with MIDI on the VLTI. *Astronomy & Astrophysics* 423, 537–548
- Lucy, L. B. (1974, Jun.). An iterative technique for the rectification of observed distributions. *Astronomical Journal* 79, 745–754
- Lynden-Bell, D. & Pringle, J. E. (1974, Sep.). The evolution of viscous discs and the origin of the nebular variables. *Monthly Notices of the Royal Astronomical Society* 168, 603–637
- Mandel, L. & Wolf, E. (1995, Oct.). *Optical Coherence and Quantum Optics* (first ed.). Cambridge, USA: Cambridge University Press, 1995
- Martins, F., Schaerer, D., & Hillier, D. J. (2005, Jun.). A new calibration of stellar parameters of Galactic O stars. *Astronomy & Astrophysics* 436, 1049–1065
- Massey, P. (1998). The Initial Mass Function of Massive Stars in the Local Group. In *The Stellar Initial Mass Function (38th Herstmonceux Conference)*, eds. G. Gilmore & D. Howell, Volume 142 of *ASP Conference Series*, 17–44
- Mathis, J. S., Rumpl, W., & Nordsieck, K. H. (1977, Oct.). The size distribution of interstellar grains. *The Astrophysical Journal* 217, 425–433
- Matsuura, M., Chesneau, O., Zijlstra, A. A., et al. (2006, Aug.). The Compact Circumstellar Material around OH 231.8+4.2. *The Astrophysical Journal Letters* 646, L123–L126
- Matzner, C. D. & McKee, C. F. (2000, Dec.). Efficiencies of Low-Mass Star and Star Cluster Formation. *The Astrophysical Journal* 545, 364–378
- McKee, C. F. & Ostriker, E. C. (2007, Sep.). Theory of Star Formation. *Annual Review of Astronomy & Astrophysics* 45, 565–687
- Meeus, G., Bouwman, J., Dominik, C., Waters, L. B. F. M., & de Koter, A. (2002, Sep.). The absence of the 10 μm silicate feature in the isolated Herbig Ae star HD 100453. *Astronomy & Astrophysics* 392, 1039–1046
- Meeus, G., Bouwman, J., Dominik, C., Waters, L. B. F. M., & de Koter, A. (2003, May). Erratum: The absence of the 10 μm silicate feature in the isolated Herbig Ae star HD 100453. *Astronomy & Astrophysics* 402, 767–767
- Meeus, G., Waters, L. B. F. M., Bouwman, J., et al. (2001, Jan.). ISO spectroscopy of circumstellar dust in 14 Herbig Ae/Be systems: Towards an understanding of dust processing. *Astronomy & Astrophysics* 365, 476–490
- Meisner, J. (2001). Fringe tracking and group delay tracking methods for MIDI. In *From optical to millimetric interferometry: scientific and technological challenges. Proceedings of the 36th Liège International Astrophysics Colloquium*, eds. J. Surdej, J. P. Swings, D. Caro & A. Detal, Volume 36 of *Liège International Astrophysical Colloquia*, 225–231
- Melnick, J., Tapia, M., & Terlevich, R. (1989, Apr.). The galactic giant H II region NGC 3603. *Astronomy & Astrophysics* 213, 89–96
- Michelson, A. A. (1890). On the application of interference methods to astronomical measurements. *Philosophical Magazine* 30, 1–20
- Michelson, A. A. (1891, Sep.). Measurement of Jupiter's Satellites by Interference. *Publications of the Astronomical Society of the Pacific* 3, 274–278

Bibliography

- Michelson, A. A. & Pease, F. G. (1921, May). Measurement of the diameter of alpha Orionis with the interferometer. *The Astrophysical Journal* 53, 249–259
- Moffat, A. F. J. (1974, Oct.). On the distance and reddening of the massive H II region NGC 3603. *Astronomy & Astrophysics* 35, 315–317
- Moffat, A. F. J. (1983, Aug.). The bright stellar content of the giant galactic H II region NGC 3603. *Astronomy & Astrophysics* 124, 273–278
- Moffat, A. F. J., Corcoran, M. F., Stevens, I. R., et al. (2002, Jul.). Galactic Starburst NGC 3603 from X-Rays to Radio. *The Astrophysical Journal* 573, 191–198
- Monnier, J. D. (1999, Oct.). Infrared interferometry and spectroscopy of circumstellar envelopes, *PhD thesis*, University of California, Berkeley
- Monnier, J. D. (2000, Jul.). An Introduction to Closure Phases. In *Principles of Long Baseline Stellar Interferometry. Course notes from the 1999 Michelson Summer School*, ed. P. R. Lawson. NASA-JPL publication 00-009, 203–229
- Monnier, J. D. (2003, May). Optical interferometry in astronomy. *Reports of Progress in Physics* 66, 789–857
- Myers, P. C., Fuller, G. A., Mathieu, R. D., et al. (1987, Aug.). Near-infrared and optical observations of IRAS sources in and near dense cores. *The Astrophysical Journal* 319, 340–357
- Natta, A., Prusti, T., Neri, R., et al. (2001, May). A reconsideration of disk properties in Herbig Ae stars. *Astronomy & Astrophysics* 371, 186–197
- Nürnberg, D. E. A. (2008, Oct.). High mass star formation to the extremes: NGC 3603 at high angular resolution in the near-infrared. *Journal of Physics Conference Series* 131(1), 012025 (8pp)
- Nürnberg, D. E. A. (2003, Jun.). Infrared observations of NGC 3603. III. The enigmatic, highly reddened sources of IRS 9. *Astronomy & Astrophysics* 404, 255–265
- Nürnberg, D. E. A. (2004, Oct.). The Galactic Starburst Region NGC 3603 : Exciting New Insights on the Formation of High Mass Stars, *PhD thesis*, Institut für Theoretische Physik und Astrophysik, Universität Würzburg, Germany
- Nürnberg, D. E. A., Bronfman, L., Yorke, H. W., & Zinnecker, H. (2002, Oct.). The molecular environment of NGC 3603. I. Spatial distribution and kinematic structure. *Astronomy & Astrophysics* 394, 253–269
- Nürnberg, D. E. A., Chini, R., Eisenhauer, F., et al. (2007, Apr.). Formation of a massive protostar through disk accretion. II. SINFONI integral field spectroscopy of the M 17 silhouette disk and discovery of the associated H₂ jet. *Astronomy & Astrophysics* 465, 931–936
- Nürnberg, D. E. A., Chini, R., & Hoffmeister, V. H. (2005, Nov.). Exciting New Vistas on High Mass Protostars and their Circumstellar Envelopes + Disks. In *The Nature and Evolution of Disks Around Hot Stars*, eds. R. Ignace & K. G. Gayley, Volume 337 of *ASP Conference Series*, 279–283
- Nürnberg, D. E. A. & Petr-Gotzens, M. G. (2002, Feb.). Infrared observations of NGC 3603. I. New constraints on cluster radius and K_S-band luminosity function. *Astronomy & Astrophysics* 382, 537–553
- Nürnberg, D. E. A. & Stanke, T. (2003, Mar.). Infrared observations of NGC 3603. II. A 11.9 μm and 18 μm survey. *Astronomy & Astrophysics* 400, 223–239
- Pandey, A. K., Ogura, K., & Sekiguchi, K. (2000, Oct.). Stellar Contents of the Galactic Giant H II Region NGC 3603. *Publications of the Astronomical Society of Japan* 52, 847–865
- Perryman, M. A. C., Lindgren, L., Kovalevsky, J., et al. (1997, Jul.). The HIPPARCOS Catalogue. *Astronomy & Astrophysics* 323, L49–L52
- Persi, P., Ferrari-Toniolo, M., Tapia, M., & Roth, M. (1985, Mar.). An infrared study of the giant H II region NGC 3603. *Astronomy & Astrophysics* 144, 275–281
- Preibisch, T., Balega, Y., Hofmann, K.-H., Weigelt, G., & Zinnecker, H. (1999, Dec.). Multiplicity of the massive stars in the Orion Nebula cluster. *New Astronomy* 4, 531–542

- Qiu, K., Zhang, Q., Wu, J., & Chen, H.-R. (2009, Jan.). Submillimeter Array Observations of the Molecular Outflow in High-mass Star-forming Region G240.31+0.07. Accepted for publication in *The Astrophysical Journal*, *ArXiv e-print* 0901.4179
- Quirrenbach, A. (2000, Jul.). Observing Through the Turbulent Atmosphere. In *Principles of Long Baseline Stellar Interferometry. Course notes from the 1999 Michelson Summer School*, ed. P. R. Lawson. NASA-JPL publication 00-009, 71–86
- Quirrenbach, A. (2001). Optical Interferometry. *Annual Review of Astronomy & Astrophysics* 39, 353–401
- Raban, D., Jaffe, W., Röttgering, H., Meisenheimer, K., & Tristram, K. R. W. (2009, Jan.). Resolving the obscuring torus in NGC 1068 with the power of infrared interferometry: Revealing the inner funnel of dust. Accepted for publication in *Monthly Notices of the Royal Astronomical Society*, *ArXiv e-print* 0901.1306
- Ratzka, T. (2005, Jun.). High Spatial Resolution Observations of Young Stellar Binaries, *PhD thesis*, Combined Faculties for the Natural Sciences and for Mathematics of the University of Heidelberg, Germany
- Rhodes, W. T. & Goodman, J. W. (1973). Interferometric technique for recording and restoring images degraded by unknown aberrations. *Journal of the Optical Society of America (1917-1983)* 63, 647–657
- Robitaille, T. P., Whitney, B. A., Indebetouw, R., & Wood, K. (2007, apr). Interpreting Spectral Energy Distributions from Young Stellar Objects. II. Fitting Observed SEDs Using a Large Grid of Precomputed Models. *The Astrophysical Journal Supplement Series* 169, 328–352
- Robitaille, T. P., Whitney, B. A., Indebetouw, R., Wood, K., & Denzmore, P. (2006, dec). Interpreting Spectral Energy Distributions from Young Stellar Objects. I. A Grid of 200,000 YSO Model SEDs. *The Astrophysical Journal Supplement Series* 167, 256–285
- Roth, M., Tapia, M., Ruiz, M. T., Persi, P., & Ferrari-Toniolo, M. (1987). New Infrared Observations of NGC 3603. In *Star Forming Regions*, eds. M. Peimbert & J. Jugaku, Volume 115 of *IAU Symposium*, 182–184
- Rowan-Robinson, M. (1980, Nov.). Radiative transfer in dust clouds. I - Hot-centered clouds associated with regions of massive star formation. *The Astrophysical Journal Supplement Series* 44, 403–426
- Salpeter, E. E. (1955, Jan.). The Luminosity Function and Stellar Evolution. *The Astrophysical Journal* 121, 161–167
- Scheegerer, A. A., Wolf, S., Hummel, C. A., Quanz, S. P., & Richichi, A. (2009). Tracing the potential planet-forming regions around seven pre-main sequence stars. Accepted for publication in *Astronomy & Astrophysics*
- Scheegerer, A. A., Wolf, S., Ratzka, T., & Leinert, C. (2008, Feb.). The T Tauri star RY Tauri as a case study of the inner regions of circumstellar dust disks. *Astronomy & Astrophysics* 478, 779–793
- Schmutzler, T. & Tscharnuter, W. M. (1993, Jun.). Effective radiative cooling in optically thin plasmas. *Astronomy & Astrophysics* 273, 318–330
- Shao, M., Colavita, M. M., Hines, B. E., Staelin, D. H., & Hutter, D. J. (1988, Mar.). The Mark III stellar interferometer. *Astronomy & Astrophysics* 193, 357–371
- Shao, M. & Staelin, D. H. (1980, May). First fringe measurements with a phase-tracking stellar interferometer. *Applied Optics* 19, 1519–1522
- Sher, D. (1965, Apr.). The Curious History of NGC 3603. *Journal of the Royal Astronomical Society of Canada* 59, 67–76
- Stephan, É. (1874). Sur l'extrême petitesse du diamètre apparent des étoiles fixes. *Comptes Rendus de l'Académie des Sciences* 78, 1008–1012
- Stolte, A., Brandner, W., Brandl, B., Zinnecker, H., & Grebel, E. K. (2004, Aug.). The Secrets of the Nearest Starburst Cluster. I. Very Large Telescope/ISAAC Photometry of NGC 3603. *Astronomical Journal* 128, 765–786
- Tapia, M., Bohigas, J., Pérez, B., Roth, M., & Ruiz, M. T. (2001, Apr.). Physical Conditions and Current Massive Star Formation in NGC 3603. *Revista Mexicana de Astronomía y Astrofísica* 37, 39–56
- ten Brummelaar, T. A. (1997, Feb.). Correlation measurement and group delay tracking in optical stellar interferometry with a noisy detector. *Monthly Notices of the Royal Astronomical Society* 285, 135–150

Bibliography

- Traub, W. A. (2000, Jul.). Beam Combination and Fringe Measurement. In *Principles of Long Baseline Stellar Interferometry. Course notes from the 1999 Michelson Summer School*, ed. P. R. Lawson. NASA-JPL publication 00-009, 31–58
- Tuthill, P. G., Monnier, J. D., Danchi, W. C., Wishnow, E. H., & Haniff, C. A. (2000, Apr.). Michelson Interferometry with the Keck I Telescope. *Publications of the Astronomical Society of the Pacific* 112, 555–565
- Unsöld, A. & Baschek, B. (1999). *Der neue Kosmos* (sixth ed.). Springer-Verlag Berlin Heidelberg New York
- van Boekel, R., Guedel, M., Henning, T., Lahuis, F., & Pantin, E. (2009). An outflow origin of the [Ne II] emission in the T Tau triplet. Accepted for publication in *Astronomy & Astrophysics*, *ArXiv e-print* 0902.1101
- van Cittert, P. H. (1934). Die wahrscheinliche Schwingungsverteilung in einer von einer Lichtquelle direkt oder mittels einer Linse beleuchteten Ebene. *Physica* 1, 201–210
- van den Bergh, S. (1978, Feb.). UBV photometry of the luminous young cluster NGC 3603. *Astronomy & Astrophysics* 63, 275–277
- van Dishoeck, E. F. (2004, Sep.). ISO Spectroscopy of Gas and Dust: From Molecular Clouds to Protoplanetary Disks. *Annual Review of Astronomy & Astrophysics* 42, 119–167
- Werner, M. W., Roellig, T. L., Low, F. J., et al. (2004, Sep.). The Spitzer Space Telescope Mission. *The Astrophysical Journal Supplement Series* 154, 1–9
- Whitney, B. A., Wood, K., Bjorkman, J. E., & Cohen, M. (2003a, Dec.). Two-dimensional Radiative Transfer in Protostellar Envelopes. II. An Evolutionary Sequence. *The Astrophysical Journal* 598, 1079–1099
- Whitney, B. A., Wood, K., Bjorkman, J. E., & Wolff, M. J. (2003b, Jul.). Two-dimensional Radiative Transfer in Protostellar Envelopes. I. Effects of Geometry on Class I Sources. *The Astrophysical Journal* 591, 1049–1063
- Whittet, D. C. B. (1992). *Dust in the galactic environment*. Institute of Physics Publishing, 306 p.
- Wolf, S. (2003). MC3D-3D continuum radiative transfer, Version 2. *Computer Physics Communications* 150, 99–115
- Wolf, S., Henning, T., & Stecklum, B. (1999, Sep.). Multidimensional self-consistent radiative transfer simulations based on the Monte-Carlo method. *Astronomy & Astrophysics* 349, 839–850
- Wood, K. (2008, Jun.). Infrared signatures and models of circumstellar dust disks. *New Astronomy Review* 52, 145–153
- Wood, K., Wolff, M. J., Bjorkman, J. E., & Whitney, B. (2002, Jan.). The Spectral Energy Distribution of HH 30 IRS: Constraining the Circumstellar Dust Size Distribution. *The Astrophysical Journal* 564, 887–895
- Yorke, H. W. & Sonnhalter, C. (2002, Apr.). On the Formation of Massive Stars. *The Astrophysical Journal* 569, 846–862
- Zernike, F. (1938). The concept of degree of coherence and its application to optical problems. *Physica* 5, 785–795
- Zinnecker, H. & Yorke, H. W. (2007, Sep.). Toward Understanding Massive Star Formation. *Annual Review of Astronomy & Astrophysics* 45, 481–563

Acknowledgements

Zunächst möchte ich mich bei meinem Diplom- und nun auch Doktorvater *Prof. Dr. Wolfgang J. Duschl* bedanken. Ohne ihn wäre diese Arbeit und auch der Aufenthalt bei der ESO nie ins Rollen gekommen. Vielen Dank für die langjährige fachliche, moralische, finanzielle und stets freundliche Unterstützung!

Einen ganz herzlichen Dank auch an *Prof. Dr. Rainer Wehrse*, der sich nach meiner Rückkehr nach Heidelberg freundlich dazu bereit erklärt hat, diese Arbeit zu bewerten. Sein Interesse und die wertvollen Tipps während dieser Zeit haben sehr dazu beigetragen, dass ich die Arbeit fertigstellen konnte.

Vielen Dank an *Dr. Christian Hummel*, der sich Mitte 2005 dazu entschlossen hat, mich im Rahmen dieses Projektes zu betreuen. Sein fortwährendes Interesse an der Arbeit, seine Hinweise und Ideen und nicht zuletzt seine stets freundliche und positive Art waren mir immer wieder eine große Hilfe.

Auch *Dr. Dieter Nürnberger*, der sich die ganze Zeit über, jedoch speziell ab Anfang 2007 immer wieder an diesem Projekt beteiligt und mich betreut hat, sei an dieser Stelle herzlich gedankt. Auch dafür, dass er mir im Rahmen eines kleinen Forschungsprojektes einen Besuch am Paranal Observatorium ermöglicht hat.

Ich danke *Prof. Dr. Joachim Krautter* und *Prof. Dr. Werner Aeschbach-Hertig* dafür, dass sie sich dazu bereit erklärt haben, der Prüfungskommission beizutreten.

Thanks also to all the people at ESO Chile. In the administration I am especially indebted to *Walter Demartis*, *Soledad Silva*, *Albert Triat* and *Paulina Jiron* for finding solutions to countless problems.

Concerning the students, fellows and staff members I am grateful for a very nice working atmosphere, funny coffee breaks, scientific and non-scientific discussions, trips in- and outside of Santiago and hilarious evenings with all the munchkins and super munchkins (S.B. for example). I had a great time with all of you, but in order to keep it short, I only mention my two office mates *Pasquier Noterdaeme* and *Cristian López* by name.

I want to thank *Dr. Valentin Ivanov* for offering me the possibility to work with him on a small project at the La Silla Observatory. It has been a great experience.

Thanks to *Dr. Olivier Chesneau* for helping me with my work especially in the beginning, but also during later stages, and for providing his IDL routine for the MIDI photometry.

I want to thank *Eric Jullo* for some nice bicycle trips on the Cerro San Cristobal. I think we lost a few years of our life in the smog... I am also grateful for helping me whenever my Spanish was not sufficient to solve a problem (Chilean bureaucracy, landlord and bank issues, chilenismos, etc.).

Acknowledgements

Dr. Vianney Lebouteiller kindly provided us with the data from Spitzer. Thanks a lot!

Außerdem möchte ich mich herzlich bei *Prof. Dr. Matthias Bartelmann* bedanken, der mir nach meinem Aufenthalt in Chile freundlicherweise einen Arbeitsplatz in seiner Gruppe am ITA zur Verfügung gestellt hat.

A big thank-you to all the members of Matthias' cosmology group! These are (or were): *Ana, Carlo, Christian* (office mate #1), *Claudia* (office mate #2), *Emanuel, Gero, Gregor, Francesco, Irina, Jean-Claude, Julian, Katja, Lavinia, Luigi, Madeleine, Massimo, Matteo, Mischa, Peter* and *René*. Working in your group was a lot of fun, including ITA movie nights, barbecues or (bavarian) breakfasts at Christian's place or simply going to a bar/cinema in the old town. It has been a great third year in Heidelberg!

Simon Glover was so kind as to correct the many linguistic shortcomings of this work. Thank you very much!

Meine *Freunde* und meine *Familie* sollen an dieser Stelle auch nicht unerwähnt bleiben. Ganz besonders meine Eltern haben mich seit jeher in meinen Vorhaben unterstützt und sind zu einem großen Teil dafür verantwortlich, dass mein Studium so gut verlaufen ist. Danke, dass ich mich immer auf eure Unterstützung verlassen konnte! Auch meine Freunde und meine restliche Familie waren mir immer wieder eine Hilfe, speziell während der Anfangsphase in Chile.

Zu guter Letzt noch *Vroni*: jetzt habe ich schon so viele Leute aufgezählt, da darfst du natürlich nicht fehlen. Egal ob ein ernsthaftes Problem oder eine unbedeutende Kleinigkeit und egal in welchem Zusammenhang, du warst immer für mich da. Danke!

I want to thank the European Southern Observatory for supporting me during the first two years of my PhD within the framework of their studentship programme. I also acknowledge financial support from the Deutsche Forschungsgemeinschaft via Sonderforschungsbereich 439 and from the University of Kiel.

This research has made use of NASA's Astrophysics Data System Bibliographic Services and of the SIMBAD database, operated at CDS, Strasbourg, France.